

UC Riverside

UC Riverside Electronic Theses and Dissertations

Title

Secondary Organic Aerosol and Ozone Formation From Photo-Oxidation of Anthropogenic Compounds and Mixtures Under Relevant Atmospheric Environment

Permalink

<https://escholarship.org/uc/item/5bk5d29k>

Author

LI, Weihua

Publication Date

2018

Peer reviewed|Thesis/dissertation

UNIVERSITY OF CALIFORNIA
RIVERSIDE

Secondary Organic Aerosol and Ozone Formation From Photo-Oxidation of
Anthropogenic Compounds and Mixtures Under Relevant Atmospheric Environment

A Dissertation submitted in partial satisfaction
of the requirements for the degree of

Doctor of Philosophy

in

Chemical and Environmental Engineering

by

Weihua Li

March 2018

Dissertation Committee:

Dr. David R. Cocker III, Chairperson

Dr. Kelley Barsanti

Dr. Roya Bahreini

Copyright by
Weihua Li
2018

The Dissertation of Weihua Li is approved:

Committee Chairperson

University of California, Riverside

Acknowledgements

After 5 years, today is the day: writing this note of thanks is the finishing touch on my dissertation. It has been a period of intense learning for me, not only in the scientific arena, but also on a personal level. Writing this dissertation has had a big impact on me. I would like to reflect on the people who have supported and helped me so much throughout this period. I would particularly like to single out my thesis advisor, Dr. David Cocker; I want to thank you for your valuable guidance throughout these years. You definitely provided me with the knowledge and tools that I needed to choose the right direction, conduct research, and successfully complete my dissertation. I would like to thank my thesis committee members, Dr. Roya Bahreini and Dr. Kelly Barsanti for their direction, dedication, and invaluable advice. I would like to thank Dr. Bill Carter for his guidance on ozone formation. I would like to thank my lab mates, Dr. Lijie Li, Dr. Chia-Li Chen, Weihan Peng, Wenfu Sun, Paul van Rooy, Dr. Derek Price, Dr. Ashley Vizenor, and Dr. Mary Kacarab, for their wonderful collaboration. Specifically, I would like to thank Chia-Li Chen for teaching me running environmental chamber. I would like to thank Lijie Li for paper writing. I would like to thank Weihan Peng and Paul van Rooy for helping me fix instruments and running experiments. I would like to thank Wenfu Sun for help with the gasoline project. I would like to thank Dr. Lindsay Hatch for your valuable comments for my alkane paper. I would like to thank Kathy Cocker for her help with GC analysis.

I would also like to thank my parents and my husband for their wise counsel. You are always there listening to my concern and complain, and sometimes bearing my bad

temper. Finally, there are my three best friends, Yu Jiang, Xi Zhang, and Hefei Bai.

Thank you for spending time with me when I felt frustrated and depressed.

Weihua Li

Riverside, Feb 20th, 2018.

ABSTRACT OF THE DISSERTATION

Secondary Organic Aerosol and Ozone Formation From Photo-Oxidation of Anthropogenic Compounds and Mixtures Under Relevant Atmospheric Environment by

Weihua Li

Doctor of Philosophy, Graduate Program in Chemical and Environmental Engineering
University of California, Riverside, March 2018
Dr. David R. Cocker III, Chairperson

Secondary organic aerosol (SOA) impacts global climate change, visibility, and human health. Further, tropospheric ozone deleteriously affects human health and plant ecosystems. This thesis focuses on atmospheric SOA and ozone formation processes from the photo-oxidation of individual and mixtures of intermediate-volatility organic compounds (IVOCs) as well as unburnt gasoline and diesel in the presence of NO_x and a surrogate reactive organic gas (ROG) mixture. These processes are evaluated using the state-of-the-art dual 90 m^3 indoor environmental chamber facility at UCR CE-CERT.

IVOCs are normally considered exempt to volatile organic compounds (VOC) regulations due to their low evaporation rates; however, half of the 14 select IVOCs investigated in this work lost more than 95% of their mass due to evaporation in less than one month. Benzyl alcohol (0.41), n-heptadecane (0.38), and diethylene glycol monobutyl ether (0.16) all had measured SOA yields greater than 0.1 in the presence of NO_x and a surrogate ROG mixture. These IVOCs also measurably influence ozone

formation compared to the surrogate ROG mixture only by impacting radical levels and NO_x availability. The overall SOA and ozone formation of the IVOC-containing generic consumer products could not be explained solely by the individual IVOC experiments.

Number 2 diesel fuel is also a complex mixture of IVOCs, which formed 14 times higher SOA than previously reported for diesel fuel. Further, doubling NO_x concentrations within relevant urban concentration levels ($\text{NO}_x < 50$ ppb) enhanced SOA formation by an additional 33%. However, when NO_x levels were raised to the very high NO_x concentrations (> 1.5 ppm) needed to mimic the earlier studies of diesel fuel SOA, SOA formation was fourteen times less than the SOA formation under low NO_x levels and consistent with earlier studies.

Direct evaporation from unburned gasoline is an established source of ozone and SOA forming precursors. As new vehicle emission control technologies continue to decrease primary organic aerosol and gas-phase emissions, whole fuel evaporation becomes a more significant source of ambient organic aerosol and ozone. While SOA formation from some gasoline components has been individually studied, there are only a few studies on how these complex mixtures behave in the atmosphere. Given changes in fuel formulations, it is important to revisit whole gasoline as an important SOA precursor, especially in light of increased knowledge on the impact of reactivity on aerosol formation and improved atmospheric chambers and instrumentation. SOA formation from photo-oxidation of gasoline samples in the presence of NO_x leads to an aerosol

yield of approximately 0.055 and is consistent regardless of fuel manufacturer or octane rating. Aerosol formation, consistent with the work of Odum et al., (1996) was observed to be driven by aromatic content in the gasoline. Aromatic hydrocarbons are important for SOA formation while certain compounds in the gasoline play an additional role by suppressing OH and therefore SOA and ozone formation. Increasing NO_x and hydroxyl radical concentrations enhance SOA and ozone formation during the photooxidation of gasoline.

Table of Contents

Chapter 1: Introduction	1
Chapter 2: Materials & Methods.....	7
2.1: IVOC and IVOC-containing mixture Volatilization Rates.....	7
2.2: Surrogate ROG Mixture.....	7
2.3: Materials	8
2.4: Hydrocarbon Solvent Analysis	11
2.5: Detailed Hydrocarbon Analysis (DHA) for gasoline samples.....	11
2.6: Photo-oxidation Experiments in UCR CE-CERT Environmental Chamber	13
Tables & Figures.....	16
Chapter 3: Potential of select intermediate-volatility organic compounds and consumer products for secondary organic aerosol and ozone formation under relevant urban conditions.....	21
3.1: Introduction.....	21
3.2: Selection of individual IVOCs and mixtures and their initial concentrations	24
3.3: Results and discussion	25
3.3.1: Atmospheric Availability of the Select IVOCs	25
3.3.2: SOA Formation.....	27
3.3.3: Ozone Formation	35
3.4: Conclusion	41

Tables & Figures.....	42
Chapter 4: Secondary organic aerosol forming potential from heavy n-alkanes and hydrocarbon solvents under relevant urban atmospheric conditions	60
4.1: Introduction.....	60
4.2: Results and discussion	63
4.2.1: SOA formation.....	63
4.2.2: SOA elemental analysis and physical properties	67
4.2.3: Ozone formation	69
4.3: Conclusion	71
Tables & Figures.....	73
Chapter 5: Secondary Organic Aerosol and Ozone Formation from Photo-Oxidation of Unburned Diesel Fuel in a Surrogate Atmospheric Environment	84
5.1: Introduction.....	84
5.2: Results and discussion	86
5.2.1: Atmospheric availability of #2 diesel	86
5.2.2: SOA formation.....	88
5.2.3: Constraining SOA yield from diesel oxidation.....	89
5.2.4: Effects of OH radical concentration on SOA formation from diesel	91
5.2.5: Ozone formation	92

5.2.6: NO _x effects.....	92
5.2.7: Trends in SOA elemental composition and SOA physical properties.....	94
5.3: Conclusion.....	96
Tables & Figures.....	98
Chapter 6: Secondary Organic Aerosol and Ozone Formation from Photo-oxidation of Unburned Whole Gasoline in a Surrogate Atmospheric Environment.....	108
6.1: Introduction.....	108
6.2: Results and discussion.....	111
6.2.1: SOA formation from photo-oxidation of unburnt whole gasoline.....	111
6.2.2: Yield of Unburned Gasoline SOA.....	112
6.2.3: NO _x effects on SOA formation.....	113
6.2.4: Effects of OH radical concentration on SOA formation.....	113
6.2.5: Aromatic content vs SOA formation.....	114
6.2.6: Trends in SOA elemental composition and SOA physical properties.....	115
6.2.7: Ozone formation from photo-oxidation of gasoline.....	117
6.3: Conclusion.....	119
Tables & Figures.....	120
Chapter 7: Conclusions & Future Work.....	130
Reference.....	136

List of Tables

Table 2. 1: Composition of Surrogate ROG Mixture 1.	16
Table 2. 2: Composition of Anthropogenic Surrogate ROG Mixture.	16
Table 2. 3: Composition information of all the gasoline blends.	17
Table 2. 4: Composition information of the aromatic mixture.	17
Table 2. 5: Experimental conditions for SOA formation from select individual IVOCs. .	17
Table 2. 6: List of analytical and characterization instrumentation.	18
Table 3. 1: Chemical and physical properties of the select IVOCs tested.	42
Table 3. 2: Formulation recipes of consumer products tested.	42
Table 3. 3: List of experiments.	43
Table 3. 4: Experimental conditions for runs listed in Figure 3.4.	44
Table 3. 5: Reaction rate constant for each individual IVOC tested.	44
Table 3. 6: Yields for individual IVOC runs with surrogate and NO _x in the absence and presence of H ₂ O ₂	44
Table 4. 1: List of experiments.	73
Table 4. 2: SOA yields for experiments listed in Figure 4.1.	73
Table 4. 3: The k _{OHs} of Conosol [®] C-200 and Isopar [®] M components.	74
Table 4. 4: Maximum incremental reactivity (MIR) values for alkanes studied.	74
Table 5. 1: List of experiments.	98
Table 5. 2: Mass loss of different #2 diesel brands in 9 months.	98
Table 5. 3: The percentage of diesel reacted.	99
Table 5. 4: List of NO _x effect runs.	99

Table 6. 1: List of experiments.....	125
Table 6. 2: The k_{OHS} of gasoline components (Jathar et al., 2013).....	121
Table 6. 3: List of NO_x effect runs.....	121

List of Figures

Figure 2. 1: Schematic for IVOC volatilization measurement.	19
Figure 2. 2: DHA analysis for winter and summer gasoline blends.	19
Figure 2. 3: The UCR/CE-CERT dual 90 m ³ chambers.	20
Figure 3. 1: Volatility and the extent of oxidation of the select IVOCs.	45
Figure 3. 2: Weight loss of the select IVOCs in Evaporation chambers (Abbreviations are defined in Table 3.1).	45
Figure 3. 3: Evaporation rate measured by the experiments and predicted by the evaporation model of the select IVOCs (calculated from weight loss results (Figure 3.2)).	46
Figure 3. 4: Comparison of SOA formations from three different photo-oxidation systems.	46
Figure 3. 5: Normalized SOA formation by total precursor consumed from select individual IVOCs with surrogate and NO _x	47
Figure 3. 6: Normalized SOA formation by total precursor consumed from individual IVOCs with surrogate, NO _x , and H ₂ O ₂	47
Figure 3. 7: Comparison of SOA formation with and without H ₂ O ₂ for select IVOCs in the presence of NO _x and surrogate.	48
Figure 3. 8: Comparison of yields obtained from calculated and measured IVOC decay.	48
Figure 3. 9: Comparison of SOA formation from single IVOCs with that from mixtures in the presence of surrogate and NO _x	49
Figure 3. 10: SOA formation from IVOCs containing generic consumer products with surrogate, NO _x , and H ₂ O ₂	49

Figure 3. 11: Correlation between the change of oxygen to carbon ratio ($\Delta O:C$) and SOA mass concentration for all the runs producing $> 2 \text{ ug m}^{-3}$ of aerosol with available AMS data . Data collected under different experimental conditions are identified by different markers.....50

Figure 3. 12: Saturation concentration and the extent of oxidation of photo-oxidation of select IVOCs in the presence of surrogate, NO_x , and H_2O_2 . Circle marker represents the OSc of SOA forming precursor. Triangle marker displays the averaged final one hour OSc and its size is scaled to corresponding SOA yield.50

Figure 3. 13: Saturation concentration and the extent of oxidation of photo-oxidation of select IVOCs in the presence of surrogate and NO_x . Circle marker represents the OSc of SOA forming precursor and its size is scaled to corresponding SOA yield. Triangle marker displays the averaged final one hour OSc51

Figure 3. 14: Relationship between (a) SOA volatility and O:C and (b) SOA volatility and oxidation state (OSc) from individual IVOCs and their mixtures photooxidation under low NO_x condition.....51

Figure 3. 15: Ozone formation from individual IVOCs with surrogate and NO_x52

Figure 3. 16: Ozone formation from individual IVOCs with surrogate, NO_x , and H_2O_2 . .52

Figure 3. 17: Typical ozone formation comparison between runs with or without H_2O_2 . 53

Figure 3. 18: Ozone formation trends for each consumer product injected into surrogate mixture.53

Figure 3. 19: Ozone formation from consumer products in surrogate mixture with enhanced H_2O_254

Figure 3. 20: SAPRC-2011 Ozone modeling results for n-Tridecane and n-Heptadecane.	59
Figure 4. 1: Comparison of SOA formation of n-C ₁₃ from three different photo-oxidation systems.....	75
Figure 4. 2: Percentage of n-Tridecane reacted VS SOA formation of n-C ₁₃ from three different photo-oxidation systems.....	75
Figure 4. 3: Comparison of SOA formation from photo-oxidation of four n-alkanes.....	76
Figure 4. 4: SOA formation from photo-oxidation of <i>n</i> -alkanes and hydrocarbon solvents with surrogate and NO _x	76
Figure 4. 5: Comparison of compound classes observed in Conosol C200 and Isopar M by GC×GC-TOFMS.	77
Figure 4. 6: GC×GC-TOFMS chromatograms for (a) Conosol [®] C200 and (b) Isopar [®] M. <i>n</i> -Alkanes, branched alkanes, and cycloalkanes are indicated by the classification bubbles, for which the size is proportional to the measured peak area.....	77
Figure 4. 7: SOA formation from photo-oxidation of <i>n</i> -alkanes and hydrocarbon solvents with surrogate, H ₂ O ₂ , and NO _x	78
Figure 4. 8: Van Krevelen diagram of <i>n</i> -C ₁₇ with the presence of surrogate and NO _x . H ₂ O ₂ is added to one of the experiments to enhance OH radical concentration.....	78
Figure 4. 9: <i>f</i> ₄₄ vs. <i>f</i> ₄₃ for the SOA generated from photo-oxidation of <i>n</i> -C ₁₇ with the presence of surrogate, NO _x and H ₂ O ₂ . The dotted lines define the triangular space where ambient OOA components fall, following Ng et al. (2010)	79
Figure 4. 10: Van Krevelen Diagram of select <i>n</i> -alkanes and hydrocarbon solvents with the presence of surrogate and NO _x	79

Figure 4. 11: Van Krevelen Diagram of select <i>n</i> -alkanes and hydrocarbon solvents with the presence of surrogate, NO _x and H ₂ O ₂	80
Figure 4. 12: f_{44} vs. f_{43} for the SOA generated from photo-oxidation of hydrocarbon solvents with the presence of surrogate and NO _x . The dotted lines define the triangular space where ambient OOA components fall. The slope and intercept of the line on the left hand side are -6.0204 and 0.4154; the slope and intercept of the line on the right hand side are -1.8438 and 0.3319.	80
Figure 4. 13: f_{44} vs. f_{43} for the SOA generated from photo-oxidation of <i>n</i> -C ₁₃ and hydrocarbon solvents with the presence of surrogate, NO _x and H ₂ O ₂ . The dotted lines define the triangular space where ambient OOA components fall. The slope and intercept of the line on the left hand side are -6.0204 and 0.4154; the slope and intercept of the line on the right hand side are -1.8438 and 0.3319.	81
Figure 4. 14: VFR of <i>n</i> -alkanes and hydrocarbon solvents with the presence of surrogate and NO _x (H ₂ O ₂ as needed).	81
Figure 4. 15: Ozone formation from photo-oxidation of <i>n</i> -alkanes and hydrocarbon solvents with surrogate and NO _x	82
Figure 4. 16: Ozone formation from photo-oxidation of <i>n</i> -alkanes and hydrocarbon solvents with surrogate, H ₂ O ₂ , and NO _x	82
Figure 4. 17: Comparison of ozone formation from photo-oxidation of <i>n</i> -C ₁₃ in the presence of surrogate and NO _x with or without H ₂ O ₂	83
Figure 5. 1: Mass loss of diesel fuel samples in evaporation chambers.	100

Figure 5. 2: Evaporation Rates of # 2 diesel samples (Table S1). Vapor pressure of n-Hexadecane was used as the vapor pressure for #2 diesel samples.....	100
Figure 5. 3: SOA formation from photo-oxidation of ten #2 diesel samples and FACE9A research diesel fuel with surrogate, NO _x , and H ₂ O ₂ . SOA formation from n-Pentadecane under the same experimental condition and Surrogate-NO _x -H ₂ O ₂ run were shown as comparison.....	101
Figure 5. 4: SOA formation comparison from photo-oxidation of D1 with and without the presence of surrogate ROG mixture.	101
Figure 5. 5: SOA formation as a function of OH radical concentration.....	102
Figure 5. 6: Ozone formation from photo-oxidation of ten #2 diesel sample and one reference diesel with surrogate, NO _x , and H ₂ O ₂	103
Figure 5. 7: SOA formation from photo-oxidation of D1 with H ₂ O ₂ at various NO _x concentrations. Surrogate ROG mixture was added to low NO _x runs.....	103
Figure 5. 8: Ozone formation from photo-oxidation of D1with surrogate and H ₂ O ₂ at various NO _x concentrations.	104
Figure 5. 9: (1) Organic mass spectra of 34 ppb NO _x verse 11 ppb NO _x (normalized to total mass). (2) Organic mass spectra of 1723 ppb NO verse 11 ppb NO _x (normalized to total mass) (3) Organic mass spectra of 1723 ppb NO verse 11ppb NO _x (normalized to (total mass – mass due to even m/z numbers)).	104
Figure 5. 10: Van Krevelen diagram of #2 diesel SOA. Dotted green lines show slopes of 0, -1 and -2. Solid grey lines show OSC of 0, -1 and -2. (a) Single run; (b) All runs	

colored by NO _x conditions. Each maker represents the average over the final one hour of the experiment.....	105
Figure 5. 11: The fractions of total organic signal at m/z 43 (f ₄₃) vs. m/z (f ₄₄) at the end of each experiment together with the triangle plot of Ng et al. (2011). The dotted lines define the space where ambient OOA components fall. The ranges of f ₄₄ observed for SV-OOA and LV-OOA components are 0.03–0.11 and 0.13–0.21, respectively. Each maker represents the average over the final one hour of the experiment.	106
Figure 5. 12: VFR of diesel SOA.....	106
Figure 5. 13: Hygroscopicity growth factor of diesel SOA.....	107
Figure 6. 1: SOA formation from winter blend gasoline with surrogate, NO _x and H ₂ O ₂ .	122
Figure 6. 2: Comparison of SOA formation from winter and summer blend gasoline with surrogate and H ₂ O ₂	122
Figure 6. 3: SOA formation from photo-oxidation of WR5 with surrogate and H ₂ O ₂ at various NO _x concentrations.	123
Figure 6. 4: (1) SOA formation from WR5 with surrogate, NO _x . H ₂ O ₂ was added as needed. (2) OH exposure vs SOA formation.	123
Figure 6. 5: SOA formation as a function of OH radical concentration under various NO _x conditions. (UCR gasoline: NO _x ~25ppb; CMU gasoline: NO _x ~100-400ppb; UCR aromatic mixture: NO _x ~25ppb;).....	124
Figure 6. 6: SOA formation VS aromatics content.....	124
Figure 6. 7:	125
Figure 6. 8: : Correlation plots of the organic mass spectra (normalized to total mass) .	125

Figure 6. 9: Triangle plot for both winter and summer blends gasoline SOAs. The fractions of total organic signal at m/z 43 (f_{43}) vs. m/z (f_{44}) at the end of each experiment (Ng et al., 2010). The ranges of f_{44} observed for SV-OOA and LV-OOA components are 0.03–0.11 and 0.13–0.21, respectively.	126
Figure 6. 10: Van Krevelen diagram of gasoline SOAs. Dotted green lines show slopes of 0, -1 and -2. Dotted grey lines show <i>OSC</i> of 0, -1 and -2.	126
Figure 6. 11: VFR of winter and summer blend gasoline SOA. VFRs of <i>m</i> -xylene and aromatic mixture SOAs are shown as comparison.	127
Figure 6. 12: Hygroscopicity growth factor of winter and summer gasoline SOAs.....	127
Figure 6. 13: Ozone formation from winter gasoline blends with surrogate, NO_x , and H_2O_2	128
Figure 6. 14: Comparison of ozone formation from winter and summer gasoline blends with surrogate, NO_x , and H_2O_2	128
Figure 6. 15: Ozone formation from photo-oxidation of WR5 with surrogate and H_2O_2 at various NO_x concentrations.	129
Figure 6. 16: Comparison of ozone formation from Wp5 with or without H_2O_2 . The other experimental conditions are the same.	129

Chapter 1: Introduction

Aerosols are defined as a metastable suspension of liquid and solid particles in the atmosphere (Flagan and Seinfeld, 1988) and are ubiquitous in the Earth's atmosphere. Airborne aerosols significantly impact human health, reduced visibility, and climate change (Qin et al., 2013). Certain sized aerosols are especially detrimental to human health by penetrating deeply into human lungs and causing severe health problems, such as asthma, cardio-respiratory diseases, and lung cancer (Pope and Dockery, 2006). Singh and Dey (2012) examined the role of aerosols on visibility degradation and they found that aerosols contribute to ~90% of the observed visibility degradation in non-foggy condition. Aerosols affect global climate directly by absorption and scattering of solar radiation and indirectly by acting as cloud condensation nuclei.

A large fraction (~50%) of the submicron aerosol mass in the troposphere consists of organic material (Jimenez, J. L. et al., 2009). Organic aerosols (OA) are classified into two categories: primary organic aerosol (POA) and secondary organic aerosol (SOA). POA is OA emitted directly into the atmosphere as particulate from processes including combustion and mechanical processes. SOA is formed in the atmosphere through photochemical conversion of gaseous volatile organic compounds (VOCs), which react with ozone (O_3), the hydroxyl (OH) radicals, and the nitrate (NO_3) radicals and form oxidation products (Kroll and Seinfeld, 2008). Clustering of these generated gas phase oxidation products produces ultrafine aerosols, which grow rapidly by condensation of gases and by coagulation (collisions between particles during their random motions).

Additionally, those generated gas phase oxidation products are considered to be semi-volatile and can partition themselves onto an absorbing organic aerosol phase at concentrations below their saturation concentrations (Odum et al., 1996).

Fractional aerosol yield (Y) is widely used to determine SOA forming potential (Pandis et al., 1991; Zhang et al., 1992; Odum et al., 1996, 1997a, b; Hoffmann et al., 1997). The yield is defined as the ratio of the amount of SOA formed from the oxidation of a given parent compound to the amount of that compound that reacted:

$$Y = \frac{\Delta M_o}{\Delta HC} \quad (1)$$

Where ΔM_o ($\mu\text{g}/\text{m}^3$) is the total organic aerosol mass formed, and ΔHC ($\mu\text{g}/\text{m}^3$) is the amount of reactive organic gas reacted. According to equation 1, aerosol yield depends on the amount of organic matter present. Y can also be expressed as a function of ΔM_o by Odum et al. (1996)

$$Y = \Delta M_o \sum_i \left(\frac{\alpha_i K_{om,i}}{1 + K_{om,i} \Delta M_o} \right) \quad (2)$$

$$K_{om,i} = \frac{F_{i,om}}{A_i M_o} \quad (3)$$

where α_i and $K_{om,i}$ are the mass-based stoichiometric coefficient and absorption equilibrium partitioning coefficient of product i . $F_{i,om}$ is the particle-phase concentration of compound i ($\mu\text{g}/\text{m}^3$) and A_i is the gas-phase concentration of compound i ($\mu\text{g}/\text{m}^3$). M_o is organic aerosol mass concentration ($\mu\text{g}/\text{m}^3$). Numerous experiments confirm that the Two-product Model is sufficient for most compounds to accurately describe the shape of

the yield curve expressed by equation 2 (Odum, et al. 1996; Odum, et al. 1997 a,b; Griffin, et al. 1999). The Two-product Model is shown in equation (4):

$$Y = \Delta M_o \left(\frac{\alpha_1 K_{om,1}}{1 + K_{om,1} \Delta M_o} + \frac{\alpha_2 K_{om,2}}{1 + K_{om,2} \Delta M_o} \right) \quad (4)$$

where 1 and 2 designate two lumped aerosol-forming products. α_1 , α_2 , $K_{om,1}$ and $K_{om,2}$ can be calculated from curve fitting using experimental data.

The Two-product Model has been extensively used to represent laboratory SOA yield results of over one hundred atmospherically relevant compounds including aromatics (Cocker et al. 2001a; Song et al. 2007;), alkenes (Matsunaga et al. 2009) and terpenes (Cocker et al. 2001b) as well as other compounds (Chan, et al. 2009; Lim and Ziemann, 2009a) and modeling studies (Kanakidou, et al. 2005). However, there are inconsistencies of the Two-Product Model parameters with the actual volatilities of the known SOA components.

Aerosol properties, such as volatility and hygroscopicity, are essential to study SOA formation. Aerosol volatility helps us to explore the mixing sate and degree of aging of aerosols. Moreover, volatility is an important property in the phase partition and SOA formation of the organic components. The volatility of SOA can be characterized by the volume fraction remaining (VFR_T), which is defined as $VFR_T = (D_T/D_{Ref})^3$ assuming spherical particles. D_{Ref} is the initial particle mode diameter determined at reference temperature (298 K). D_T is the final particle mode diameter after evaporation at an

elevated temperature. The increasing trend of VFR implies less volatile aerosols formation (Emanuelsson et al., 2013). Aerosol hygroscopicity is a result of chemical composition and mixing state of particles. The hygroscopic growth of aerosol is described by the relative increase in the mobility diameter of particles because of water up-take at a specific relative humidity (RH) (Flores et al., 2012). The growth factor (GF) of a particle is defined as the ratio between the particle's diameter at a given relative humidity RH_1 , and its diameter at (typically lower) reference humidity RH_0 (Meier et al., 2009).

$$GF = \frac{D_p(RH_1)}{D_p(RH_0)} \quad (5)$$

D_p is the mobility diameter of a particle.

The oxidation of large organics associated with SOA is a very complex process (reaction pathways, intermediates, and products), which prevents the precise measurement and prediction of the oxidation associated with the formation and evolution of atmospheric organic aerosol. Therefore, the mean oxidation state of carbon of the organic aerosol is an ideal metric for the degree of oxidation of organic species in the atmosphere, and regarded as a key quantity to describe organic mixtures (Kroll, et al. 2011). The mean oxidation state of carbon of the organic aerosol increases upon oxidation. The simplified equation is described in the following:

$$\overline{OS}_c = 2O/C - H/C \quad (6)$$

Both POA and the precursors of SOA originate from anthropogenic, biogenic, and biomass burning sources. SOA has recently gained much attention because current models estimate that they account for a dominant fraction of the total organic particulate mass (Hallquist et al., 2009). However, those models still can't explain a significant portion of both ambient and laboratory SOA (Koo et al., 2003; Volkamer et al., 2006; Cappa et al., 2016; Jathar et al., 2017). Many previous studies suggest that the missing SOA can be explained by the evaporation and subsequent oxidation of intermediate-volatility organic compounds (IVOCs) (Yee et al., 2012; Zhao et al., 2014), which have saturation concentrations ranging from 10^3 to 10^6 $\mu\text{g m}^{-3}$ and in ambient conditions are found almost entirely in the vapor phase (Donahue et al., 2012). Due to their lower volatility and heavier molar mass than traditional volatile organic compounds (VOCs), IVOCs are expected to be important SOA-forming contributors (Robinson et al., 2007; Chan et al., 2009). Many consumer and personal care products contain IVOCs. A detailed mass balance study by McDonald et al. (2018) demonstrates that use of volatile chemical products, including pesticides, coatings, printing inks, adhesives, cleaning agents, and personal care products now constitute half of fossil-VOC emissions in industrialized cities. Therefore, conducting research on SOA and ozone formation from these IVOC-containing products is necessary.

The majority of atmospheric ozone is in the stratosphere, while only a small fraction (~10%) is present in the troposphere, where reactions among nitrogen oxides (NO_x (NO and NO_2)), carbon monoxide (CO) and VOCs, in the presence of sunlight contribute to

O₃ formation. In the early 1970s, it was suggested that photo-oxidation of the simplest and most abundant of all hydrocarbons, methane (CH₄), and CO can cause O₃ formation in large areas of the troposphere (Lelieveld and Dentener, 2000). VOCs precursors from motor vehicle exhaust, industrial emissions, and chemical solvents are major anthropogenic sources for O₃ formation. NO_x emissions are mainly from anthropogenic sources. O₃ formation could be controlled by regulating NO_x emission. Many countries have imposed stringent NO_x control regulations to resolve near surface O₃ problems (Li, et al., 2013).

This dissertation experimentally examines SOA and ozone formation from the photo-oxidation of select IVOCs, IVOC-containing mixtures, and unburned commercial gasoline under urban low NO_x (<50 ppb) concentrations in the presence of the surrogate reactive organic gas (ROG) mixture used to control the chamber reactivity and mimic urban atmospheric activity. Controlling chamber reactivity with a surrogate ROG mixture has been previously explored to study ozone formation by measuring incremental reactivities of representative volatile organic compounds (VOCs) (Carter et al., 1995, 2005). The atmospheric availability of select IVOCs and IVOC-containing mixtures, SOA mass yields, ozone formation, and bulk SOA chemical composition and physical properties are explored. This paper provides fundamentals for constraining modeling research to better estimate SOA and ozone formation.

Chapter 2: Materials & Methods

2.1: IVOC and IVOC-containing mixture Volatilization Rates

Evaporation rates of individual IVOCs and IVOC-containing mixtures were studied gravimetrically within miniature (~30 L) evaporation chambers operating as continuous stirred tank reactors (CSTRs, Figure 2.1). The residence time of the chambers was set to 3.5 exchanges of air per hour. The air entering these chambers was purified (Aadco 737) and had no detectable particles (<0.2 particles cm^{-3}), non-methane hydrocarbons (<1 ppb), and NO_x (<10 ppt). The dew point of the air was less than -60 °C. The temperature of individual environmental chambers was maintained at 25°C .

The evaporative mass flux was measured by a mass balance approach with the pure compounds being placed on aluminum boats (capacity 20 ml, top I.D. 43 mm, Sigma-Aldrich) and weighed. Samples were weighed daily for the first ten days and then weekly thereafter for compounds with slow evaporative rates for a period of six months. A bank of 10 of these systems was utilized in parallel to simultaneously measure the evaporation rate of the ten IVOC or IVOC-containing mixture samples.

2.2: Surrogate ROG Mixture

Two surrogate ROG mixtures were used in this dissertation. One (surrogate ROG mixture 1) was developed by Carter et al. (Carter et al., 1995) to represent the major classes of hydrocarbons and aldehydes measured in ambient urban atmospheres, with one compound used to represent each model species used in condensed lumped-molecule

mechanism. Total surrogate concentrations used were 1.1 ppmC. The concentration of each species in the surrogate ROG mixture can be found in Table 2.1. Surrogate ROG mixture 1 is used for individual IVOC and industrial hydrocarbon solvents.

The other surrogate ROG mixture (surrogate ROG mixture 2) used was also 1.1 ppmC and was injected to simulate urban air gas-phase reactivity rather than allowing the gasoline and diesel fuel to dominate the overall system reactivity. The surrogate ROG mixture 2 is described in detail in Kacarab, M.E. (2016). Briefly, this surrogate is similar to the first surrogate but aerosol forming species minimized. The concentration of each component of the simplified ROG surrogate 2 used for this work is listed in Table 2.2. Surrogate ROG mixture 2 is used in the study of SOA and ozone formation from unburnt gasoline and diesel samples.

2.3: Materials

All liquid precursor chemicals from Sigma-Aldrich and all chemicals used in experiments are as follows: Individual IVOCs: Propylene Glycol, $\geq 95\%$; Diethylene Glycol, $\geq 95\%$; Diethylene Glycol Ethyl Ether (DEGEE), $\geq 95\%$; Diethylene Glycol Monobutyl Ether (DEGEBE), $\geq 95\%$; Benzyl Alcohol, $\geq 95\%$; Dipropylene Glycol Methyl Ether Acetate (DPGMEA), $\geq 95\%$; Dimethyl Glutarate (DBE-5), $\geq 95\%$; *n*-Tridecane (*n*-C₁₃), $\geq 99\%$; *n*-Tetradecane (*n*-C₁₄), ($>99\%$); *n*-Hexadecane, (*n*-C₁₆) ($>99\%$); *n*-Heptadecane (*n*-C₁₇), ($>99\%$); 2,2,4-Trimethyl-1,3-Pentanediol Monoisobutyrate (Texanol®), $\geq 95\%$; Glyceryl Triacetate, $\geq 95\%$; Methyl Palmitate, $\geq 95\%$; Triethanolamine, $\geq 95\%$; Glycerol, $\geq 95\%$.

Surrogate ROG mixture: Acetaldehyde, $\geq 99.5\%$; n-Butane, $\geq 95\%$; m-Xylene, $\geq 99.5\%$; Ethylene, $\geq 95\%$; 1,2,4-Trimethylbenzene, $\geq 98\%$; trans-2-Butene, $\geq 95\%$; 1-Pentene, $\geq 98.5\%$; Toluene, $\geq 95\%$; Methyl ethyl ketone, $\geq 99\%$; Propylene, $\geq 95\%$; Isoprene, $\geq 99\%$; 2-Methylbutane, $\geq 99.5\%$; Methylcyclopentane, $\geq 97\%$; n-Octane $\geq 95\%$.

Other chemicals: Perfluorohexane ($>99\%$), H_2O_2 (50wt% solution in water), nitrous oxide, ultra-high purity, Matheson. NO_2 was generated in-situ by chemical conversion of NO.

Hydrocarbon solvents studied include Isopar[®] M and Conosol[®] C-200, which were provided by Exxon Mobil Corporation and Calumet Specialty Products Partners, L.P., respectively. Both Isopar[®] M and Conosol[®] C-200 are complex mixtures of alkanes; Isopar[®] M is a low aromatic mixture of C_{11} - C_{16} n-alkanes, iso-alkanes, and cycloalkanes whereas Conosol[®] C-200 is a low aromatic mixture of C_{12} - C_{16} iso-alkanes and cycloalkanes. The relative proportions of straight-chain, branched, and cyclic alkanes present in each solvent were assessed using comprehensive two-dimensional gas chromatography with time-of-flight mass spectrometry (GC \times GC-TOFMS).

Commercial #2 diesel fuels were collected in 1 L amber glass bottles from service stations throughout the Riverside, California area during the winter (February) of 2016. Winter and summer blend gasoline samples are collected in 1 L amber glass bottles from service stations throughout the Riverside, California area during the winter (February)

and summer (June) of 2016, respectively. The containers were labeled and immediately stored in an ice chest for transport to the laboratory where they were stored at -5 °C and -20 °C for diesel and gasoline, respectively. The diesel samples represent ten major commercial brands (D1-D10). An additional reference research diesel fuel was obtained from Lawrence Berkeley National Laboratory labeled as FACE9A (Fuels for Advanced Combustion Engines, sample 9, Batch A). The FACE9A research diesel fuel was designed based on 3 properties, which are essential to the performance of advanced combustion engines: ignition quality (cetane number), fuel chemistry (aromatics volume fraction), and volatility (distillation temperature). There are two similarities between the FACE9A research diesel fuel and commercial diesel fuels. Both of them are predominantly composed of n-paraffins, isoparaffins, cycloparaffins, and aromatics, with little-to-no olefins. The FACE9A research diesel fuel has a normal distribution of n-paraffins peaking at about C₁₄-C₁₅. And commercial diesel fuels have a normal distribution of n-paraffins peaking at about C₁₅-C₁₇ (Chevron Corporation, 2007). However, the FACE9A research diesel fuel contains a higher aromatic volume fraction and distillation temperature as compared with commercial diesel fuels (Alnajjar et al., 2010). The gasoline samples represent five major brands and two grades (regular (87) and premium (91)). The winter and summer gasoline blends are labeled as WGS and SGS plus a number, respectively. The number refers to octane rating, with odd and even numbers associated with regular and premium grades, respectively. In addition, the odd number together with the next larger even number indicates that the two gasoline samples are from the same commercial gasoline brand (eg. WGS1=winter gasoline sample (87 grade);

WGS2=winter gasoline sample (91grade); both WGS1 and WGS2 are from the same commercial brand).

2.4: Hydrocarbon Solvent Analysis

The composition of Isopar[®] M and Conosol[®] 200 were determined by GC×GC-TOFMS (Pegasus 4D, Leco Corp., St. Johns, MI). Each solvent was diluted 100-fold in hexane, followed by 1 μ L injection at 250 $^{\circ}$ C and 20:1 split ratio. The column set included an Rxi-5SilMS primary column (40 m, 0.18 mm ID, 0.18 μ m film, Restek Corp., Bellefonte, PA) and an Rxi-17SilMS secondary column (1.5 m, 0.15 mm ID, 0.15 μ m film, Restek Corp., Bellefonte, PA). The primary oven was held at 75 $^{\circ}$ C for 1 min, followed by a ramp at 1.25 $^{\circ}$ C/min to 175 $^{\circ}$ C with a final hold of 2 min. The secondary oven temperature was offset +5 $^{\circ}$ C relative to the primary oven and the modulator temperature was +40 $^{\circ}$ C relative to the secondary oven. The column flow rate was 0.8 mL/min with helium carrier gas. Analysis of the hexane solvent confirmed no contamination was present in the C₁₁-C₁₆ elution regions. A PiONA hydrocarbon standard (Restek Corp., Bellefonte PA) was additionally analyzed to identify *n*-alkanes through pentadecane.

2.5: Detailed Hydrocarbon Analysis (DHA) for gasoline samples

DHA, which provides in-depth molecular composition testing data for crude oil feedstocks, fuels, and other petroleum products, is applied to determine the chemical composition profile of both winter and summer gasoline blends using an Agilent 7890A gas chromatography equipped with flame ionization detectors (GC-FID). Standards used

include a stock sim dis paraffin solution (AccuStandard ASTM-P-0050), a quantitative calibration mix (AccuStandard ASTM-D3710) for petroleum products, and a certified aromatic mix (AccuStandard D-5769-ADD/IS-R2). For all of the fuels, between 94.5 and 98.8% of the mass of each gasoline sample is speciated by DHA analysis.

To illustrate the key differences in fuel composition, in Figure 2.2, we plot these data by fuel sample, color-coded by molecular structure. Both commercial winter and summer gasoline samples are primarily composed of aromatics, isoalkanes, n-alkanes, oxygenates, olefins, and cycloalkanes (Table 2.3). Compared with winter blends gasoline, the summer blends have less oxygenate to reduce volatile organic compounds emissions. Several studies are available to link both molecular structure and carbon number to SOA forming potential (Odum et al., 1997a, 1997b; Lim and Ziemann, 2005, 2009a, 2009b; Presto et al., 2010; Tkacik et al., 2012; Loza et al., 2014). From a molecular structure perspective, SGS3 (summer gasoline sample 3) is expected to form the most SOA since it has the most aromatics content.

The top five aromatics (by mass) based on the DHA analysis (Figure 2.2) for WGS9 were selected to make an aromatics mixture, which was used to explore whether the aromatics content in the gasoline sample drives the SOA formation. The concentration of the aromatic mixture in the chamber is matched to the concentration of gasoline aromatic content (WGS9) in the chamber. The detailed composition data for this aromatics mixture is in Table 2.4.

2.6: Photo-oxidation Experiments in UCR CE-CERT Environmental Chamber

SOA and ozone formation from photo-oxidation of all the chemicals and mixtures were studied in the UCR CE-CERT dual indoor smog chambers (2 mil FEP Teflon film) (Figure 2.3), which are described in detail elsewhere (Cocker, et al., 2001c; Carter, et al., 2005). The chambers were located in a temperature and humidity-controlled (<0.1%) enclosure. Before conducting each experiment, the chambers were cleaned by reducing the chamber volume to less than 5% of its original volume while flushing the chamber with 500 L/min of purified air to make sure that the chambers had no detectable nonmethane hydrocarbons (1 ppbC detection limit), NO_x (<10 ppt), and particles (<0.2 particles/ cm³). The chambers were then filled to capacity with purified air.

Known volumes of NO and NO₂ were introduced into calibrated bulbs based on calculated partial pressures and then flushed into the chambers by using 50°C pure N₂ as the carrier gas. Gas phase surrogate was injected directly into the chambers at a flow rate of 0.5 LPM. Liquid phase surrogate and tracer (perfluorohexane) were injected into a small glass tube using a microliter syringe and then were vaporized in a 50 °C pure N₂ stream. The additional OH radical was generated via photolysis of hydrogen peroxide, which was gently heated (55-60 °C) in a small oven through glass wool (tube) and evaporated into a nitrogen stream (~5 LPM) to the chambers for about 20 minutes to insure an initial mixing ratio of approximately 1 ppm. The two chambers were subsequently mixed to reach identical concentrations on both sides. The two reactors were then isolated from each other and the SOA forming precursor of interest was

injected into one of the chambers. The other chamber was used as control. 272 UV black lights (115 W Sylvania 350BL, NO_2 photolysis rate 0.4 min^{-1}) were turned on to initiate photo-oxidation. All experiments were conducted at 300 K in the absence of seed. Table 2.5 lists the experimental types and corresponding description.

Decay of SOA-forming precursor was monitored using dual Agilent 6890 (Palo Alto, CA) gas chromatographs equipped with flame ionization detectors (GC-FID) and a Syft Technologies Voice200 Selected Ion Flow Tube-Mass Spectrometer (SIFT-MS). Ozone concentration was monitored by a Dasibi Environmental Corp. Model 1003-AH O_3 analyzer. A Thermo Environmental Instruments Model 42C chemiluminescence NO_x analyzer was used to evaluate concentrations of NO, NO_2 and NO_x .

Particle concentrations inside the chambers were monitored using a pair of scanning mobility particle sizers (SMPS). Particle wall loss was corrected using the method described in Cocker et al. (2001c). A house-built volatility tandem differential mobility analyzer (VTDMA) equipped with a Dekati thermodenuder (CSi32) was used to track the evolving volatility of SOA produced within the reaction chamber (residence time = 17 sec; temperature 100°C) (Rader and McMurry, 1986; Cocker et al., 2001c). Particle density was measured by a Kanomax aerosol particle mass analyzer (APM) coupled to a house-built SMPS (Malloy et al., 2009).

The nonrefractory submicrometer particle mass and composition were monitored by an Aerodyne high-resolution time-of-flight aerosol mass spectrometer (HR-ToF-AMS) (DeCarlo et al., 2006). The HR-ToF-AMS was alternatively operated in V- and W-modes to provide both high sensitivity and high mass resolution data. AMS data were analyzed using the standard AMS data analysis software SQUIRREL v1.57 and PIKA v1.16, the standard ToF-AMS analysis toolkits written in Igor Pro 6.30 (WaveMetrics Inc., Lake Oswego, OR). Table 2.6 lists all the analytical and characterization instruments used in this dissertation.

Work by the Ziemann group at UCR (now at University of Colorado, Boulder) (Matsunaga and Ziemann, 2010) has more recently challenged the conventional assumption that the highly hydrophobic Teflon surfaces used for chamber wall material do not participate in the gas-particle equilibrium achieved within the reaction mixture inside the chamber. Matsunaga and Ziemann (2010) point out those sufficiently low vapor pressure products could participate in an equilibrium process with the wall, providing a sink for VOCs during the initial part of the experiment and a possible source later in the experiment. More recently, papers by Yeh and Ziemann (2014), Krechmer et al. (2016), Ye et al. (2016), and Zhang et al. (2014) have provided additional insight into the potential effects of chamber walls with their impacts ranging from very significant to minor. Considering direct loss of vapors to the chamber walls would likely result in higher SOA mass yields. However, these losses are uncertain and have not been

accounted for by most of current smog chamber studies. Therefore, we do not make any corrections for direct loss of vapors to the chamber walls.

Tables & Figures

Table 2. 1: Composition of Surrogate ROG Mixture 1.

ppb/ppmC	Compound
20.6	<i>m</i> -Xylene
89.8	n-Butane
20.7	n-Octane
13.6	trans-2-Butene
23.1	Toluene
16.3	Ethylene
13.6	Propylene

Table 2. 2: Composition of Anthropogenic Surrogate ROG Mixture.

ppb/ppmC	Compound
46	Acetaldehyde
5	<i>m</i> -Xylene
5	1,2,4-Trimethylbenzene
90	n-Butane
14	trans-2-Butene
14	Toluene
22	2-Methylbutane
13	Methylcyclopentane
16	Ethylene
14	Propylene
3	1-Pentene
17	Methyl Ethyl Ketone
2	Isoprene

Table 2. 3: Composition information of all the gasoline blends.

Winter gasoline blend composition (%)						
Sample #	Aromatics	n-Alkanes	Oxygenates	Isoalkanes	Olefins	Cycloalkanes
WGS1	23.2	11.5	10.2	30.0	18.0	2.6
WGS2	16.5	9.9	11.4	44.0	15.8	0.0
WGS3	19.2	11.4	10.5	32.6	19.3	3.0
WGS4	25.1	9.5	8.1	38.9	11.9	3.3
WGS5	27.7	11.7	8.9	29.3	16.3	2.5
WGS6	14.9	9.4	12.8	44.0	16.2	0.0
WGS7	26.6	11.3	8.2	31.4	16.1	2.0
WGS8	25.7	9.7	9.8	34.9	14.4	2.4
WGS9	24.1	11.0	8.3	33.1	16.6	1.9
WGS10	19.6	11.7	8.7	43.8	13.1	2.0
Summer gasoline blend composition (%)						
SGS1	20.5	6.5	10.8	35.0	17.2	5.2
SGS2	26.1	12.7	9.2	28.6	14.9	3.6
SGS3	31.3	14.9	10.5	21.5	14.9	4.1
SGS4	24.8	16.6	13.0	22.9	15.2	3.1
SGS5	28.3	11.1	9.4	26.0	15.9	4.5
SGS6	19.6	6.5	12.0	35.9	15.7	5.5
SGS7	30.2	11.8	13.3	22.4	14.6	2.2
SGS8	21.9	6.1	10.3	36.7	15.3	4.8
SGS9	27.9	10.5	10.6	24.5	16.9	4.7
SGS10	19.0	6.5	10.7	36.7	17.1	5.6

Table 2. 4: Composition information of the aromatic mixture.

Aromatic	Mass (%)	Volume injected (ul)
Benzene	0.017	5
Toluene	0.070	21
M-xylene	0.062	19
1-Methyl-4-ethylbenzene	0.014	4
1,2,4-Trimethylbenzene	0.029	9

Table 2. 5: Experimental conditions for SOA formation from select individual IVOCs.

Experimental conditions	Description
IVOC + H ₂ O ₂ + UV	Simplest oxidation experiment to study SOA formation from IVOC, no surrogate added. The photolysis of H ₂ O ₂ increases both OH and HO ₂ radical concentrations.
IVOC + NO + UV	Photo-oxidation system with individual IVOC to study directly IVOC oxidation and SOA formation.
Surrogate + NO _x + UV	Performed in parallel as control for surrogate containing experiments described immediately below.
IVOC + Surrogate + NO _x + UV	Photo-oxidation system where a surrogate mixture is used to study the effects of individual compounds on overall SOA and ozone formation.
Surrogate + NO _x + UV + H ₂ O ₂	Performed in parallel as control for surrogate containing experiments described immediately below.
IVOC + Surrogate + NO _x + H ₂ O ₂ + UV	Introduction of a test compound into the surrogate mixture can lead to competition for the hydroxyl radical. Experiments are conducted with 1 ppm H ₂ O ₂ to reduce the impact of hydroxyl radical loss.

Table 2. 6: List of analytical and characterization instrumentation.

Type	Model or Description	Species	Sensitivity	Comments
Gas Calibrator	Model 146C Thermo Environmental Dynamic Gas Calibrator	N/A	N/A	Used for calibration of NO _x and other analyzers.
Data Acquisition System	Windows PC with custom LabView software, 16 analog input, 40 I/O, 16 thermo-couple, and 8 RS-232 channels.	N/A	N/A	Used to collect data from most monitoring instruments and control sampling solenoids. In-house LabView software.
Temperature sensors	Various thermocouples, radiation shielded thermocouple housing	Temperature	~0.1 °C	Primary measurement is thermocouples inside reactor.
Ozone Analyzer	Dasibi Model 1003-AH. UV absorption analysis.	O ₃	2 ppb	Standard monitoring instruments.
NO - NO _y Analyzer	Chemiluminescent analysis for NO, NO _y by catalytic conversion.	NO NO _y	1 ppb 1 ppb	Useful for NO and initial NO ₂ monitoring.
GC-FID #1	HP 6890 Series II GC with dual columns, loop injectors and FID detectors. Various megabore GC columns available. Controlled by computer interfaced to network.	VOCs	~10 ppbC	Equipped with: 30 m x 0.53 mm GS-Alumina column used for the analysis of light hydrocarbons and 30 m x 0.53 mm DB-5 column used for the analysis of C ₅₊ alkanes and aromatics.
GC-FID #2	HP 6890 Series II GC with dual columns and FID detectors, one with loop sampling and one set up for cartridge sampling. Various megabore GC columns available. Controlled by computer interfaced to network.	VOCs	~10 ppbC	30 m x 0.53 mm GSQ column. Loop injection suitable for low to medium volatility VOCs that are not too "sticky". Sorption cartridge sampling was used for low volatility or moderately "sticky" VOCs that cannot go through GC valves but can go through GC columns.
Humidity Monitor	LiCor Li-840	Humidity	Dew point range: -60 - 50°C	Used for determination of RH in system. RH for dry experiments often below detection limit (<0.1% RH).
Spectroradiometer	LiCor LI-1800 Spectroradiometer	300-850 nm Light Spectrum Spherical	Adequate	Resolution relatively low but adequate for its purpose. Used to obtain relative spectrum. Also gives an absolute intensity measurement at Teflon surface useful for assessing relative trends.
Spherical Irradiance Sensors	Biospherical QSL-2100 PAR Irradiance Sensor or related product. Responds to 400-700 nm light. Spectral response curve included.	Broad-band Light Intensity	Adequate	Provides a measure of absolute intensity and light uniformity that is more directly related to photolysis rates than light intensity on surface.
Scanning Mobility Particle Sizer (SMPS)	Consists of TSI 3081L differential mobility analyzer, TSI 3077 ⁸⁵ Kr neutralizer, TSI 3760A condensation particle counter.	Aerosol Number and Volume concentration	Adequate	Provides information on size distribution of aerosols in the 28-730 nm size range, which accounts for most of the aerosol mass formed in our experiments.
Tandem Differential Mobility Analyzer (TDMA)	Comprised of two TSI 3081L differential mobility analyzer, TSI 3077 ⁸⁵ Kr neutralizer, TSI 3760A condensation particle counter and thermal denuder.	Aerosol volatility	Adequate	Provides information on the volatility of SOA produced during the reaction.
APM-SMPS	Kanomax APM coupled to custom SMPS similar to that described above	Aerosol Density	Requires ~5 ug m ⁻³ PM	Used to obtain real time (every 100 sec) density data necessary to convert aerosol volume (from SMPS) to aerosol mass
SIFT-MS	SYFT Voice200 single ion flow tube mass spectrometer	VOCs	Sub ppb	Online, real time (1 hz) acquisition of VOC data including LVP-VOCs
HR-ToF-AMS	Aerodyne High Resolution (W and V-mode) time of flight aerosol mass spectrometer	PM chemical composition	Requires ~5 ug m ⁻³ PM	Online measurement of aerodynamic particle mobility and EI mass fragmentation pattern from chamber aerosol.

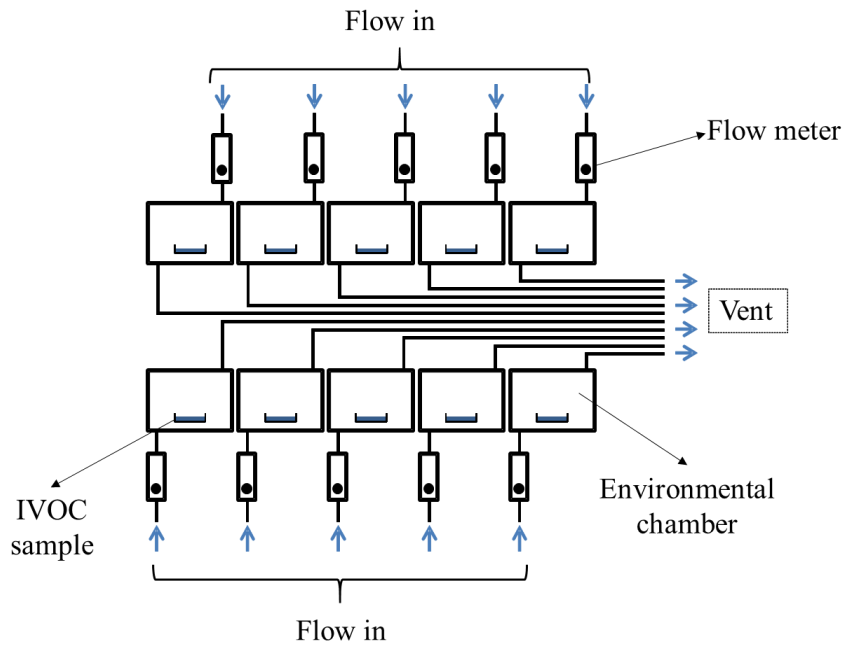


Figure 2. 1: Schematic for IVOC volatilization measurement.

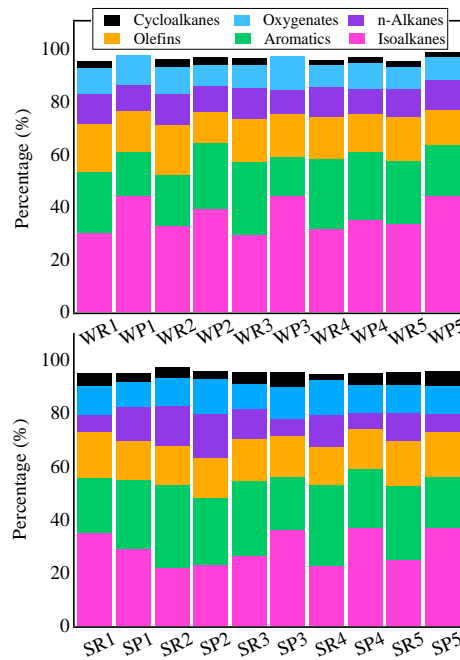


Figure 2. 2: DHA analysis for winter and summer gasoline blends.

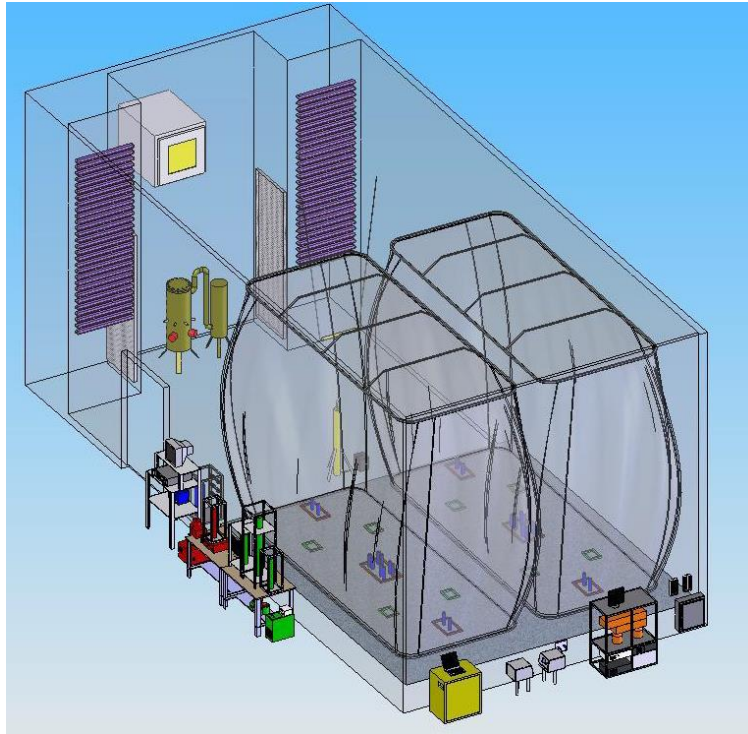


Figure 2. 3: The UCR/CE-CERT dual 90 m³ chambers.

Chapter 3: Potential of select intermediate-volatility organic compounds and consumer products for secondary organic aerosol and ozone formation under relevant urban conditions.

3.1: Introduction

Atmospheric fine particulate matter is considered to have significant effects on the earth's energy budget, human health, and visibility (Yee et al., 2013; Naeher et al., 2007; Qin et al., 2013). Secondary organic aerosol (SOA) is estimated to account for a dominant fraction of the fine particle mass in the troposphere (Hallquist et al., 2009; Cappa et al., 2016; Jathar et al., 2017; Ma et al., 2017). However, current models still cannot explain a significant portion of ambient SOA (Presto et al., 2009). In addition, emissions of volatile organic compounds (VOCs) into the air contribute to tropospheric ozone formation, higher concentration of which is a threat to human health and plant ecosystems (Finlayson-Pitts and Pitts, Jr., 1993).

The California Air Resources Board (CARB) defines a low vapor pressure-volatile organic compound (LVP-VOC) as a chemical "compound" containing at least one carbon atom with vapor pressure less than 0.1 mm Hg at 20°C, or having more than 12 carbon atoms, or having a boiling point greater than 216°C, or as a chemical mixture being comprised solely of compounds with more than 12 carbon atoms, or as the weight percent of a chemical mixture that boils above 216°C (CARB, 2015). The CARB estimates LVP-VOC usage in California to be 290 tons/day (Cocker et al., 2014). These low-volatility organic compounds are widely used to produce industrial solvents, coatings, cosmetic,

perfume, and pharmaceutical products (Bernard et al., 2013; Vo and Morris, 2014). Vo and Morris (2014) demonstrate that some LVP solvents being categorized as meeting the LVP-VOC nonvolatile standards clearly volatilize at ambient conditions, nearly as rapidly as the traditional high volatility solvents they are meant to replace. Shin et al. (2016) develop and evaluate environmental modeling tools and find that when the LVP-VOC in a consumer product is volatilized from the surface to which it has been applied, greater than 90% is available for photochemical reactions either at the source location or in the downwind areas.

Select LVP-VOCs are considered as intermediate-volatility organic compounds (IVOCs) according to their vapor pressures and molecular formulas. These IVOCs have saturation concentrations ranging from 300 to $3 \times 10^6 \mu\text{g m}^{-3}$ (1 to 1000 mg m^{-3}) and are found almost entirely in the vapor phase (Donahue et al., 2012). Much heavier and less volatile IVOCs can potentially form SOA more efficiently than the more abundant but much more volatile traditional VOC SOA precursors (Robinson et al., 2007; Chan et al., 2009). Therefore, conducting research on SOA forming potential from these IVOCs helps to explain the gap between SOA model prediction and ambient measurement. However, not very much experimental work has been published on SOA formation from IVOCs. Most of the work has focused on the SOA forming potential of alkanes (straight chain, branched, and cyclic), naphthalene, alkylnaphthalenes, and exhaust from gasoline and diesel powered vehicles (as summarized below).

Several smog chamber experiments under both high and low NO_x conditions confirm that SOA generated from photo-oxidation of IVOCs may be an important contributor to urban organic aerosol (OA) and should be included in SOA models (Presto et al., 2009; Tkacik et al., 2012). Gentner et al. (2012) find that on-road diesel vehicles are a major source of IVOC emissions in the Los Angeles area. Additionally, substantial formation of SOA is observed from the oxidation of diesel emissions (Weitkamp et al., 2007; Sage et al., 2008; Gentner et al., 2012). Recently, Zhao et al. (2014) estimate that primary IVOCs produce about 30% of newly formed SOA in the afternoon during the California at the Nexus of Air Quality and Climate Change (CalNex) study, about 5 times more than that from single-ring aromatics.

High SOA yields are also observed from reactions of C₁₂-C₁₇ n-alkanes, C₁₀-C₁₅ cyclic alkanes, and C₁₆ branched alkanes with OH radicals in the presence of high NO_x in an environmental smog chamber (Lim and Ziemann, 2005; Lim and Ziemann, 2009; Presto et al., 2010; Loza et al., 2014). The yields from photo-oxidation of C₁₂ cyclic alkanes are also high under low NO_x condition (Loza et al., 2014). However, Tkacik et al. (2012) do not report high yields for high-NO_x photo-oxidation of C₁₂ straight chain, branched, and cyclic alkanes at lower COA (organic aerosol concentration) that are more representative of typical atmospheric aerosol concentrations. Under low NO_x conditions, the yields are high for photo-oxidation of naphthalene, 1-methylnaphthalene, and 2-methylnaphthalene (Chan et al., 2009; Chen, et al., 2016).

This work experimentally examines SOA and ozone formation from the photo-oxidation of select IVOCs and generic consumer products containing one of the select IVOCs under urban low NO_x (18.7-36.4 ppb) concentrations in the presence of a surrogate mixture used to control the chamber reactivity and mimic urban atmospheric activity. Controlling chamber reactivity with a surrogate reactive organic gas (ROG) mixture has been previously explored to study ozone formation by measuring incremental reactivities of representative volatile organic compounds (VOCs) (Carter et al., 1995, 2005). The atmospheric availability of select IVOCs, SOA mass yields, ozone formation, and bulk SOA chemical composition and physical properties from select IVOCs and mixtures containing some of them are explored. This paper provides fundamentals for constraining modeling research to better estimate SOA and ozone formation from IVOCs.

3.2: Selection of individual IVOCs and mixtures and their initial concentrations

The selection of individual IVOCs and consumer products mixtures was made in direct consultation with CARB staff and the advisory committee (industry experts) set-up by CARB based on use and chemical classes. Fourteen LVP-VOCs were initially selected for analysis (Table 3.1); however as three (glycerol, methyl palmitate, and triethanolamine) were not evaporate under ambient conditions over a six-month time period they were not studied as part of the subsequent environmental chamber work. Additionally, five IVOC containing consumer products were selected (recipes shown in Table 3.2). These generic consumer products were formulated with guidance from the Consumer Specialty Products Association (CSPA). Initial precursor concentrations of

IVOC (40 to 160 ppb, Sigma-Aldrich ($\geq 95.0-99.0\%$)) were selected based on preliminary SAPRC-11 ozone modeling (lumped gas-phase kinetic model, see Carter et al., 2012) to ensure that a measurable and kinetically comparable change in ozone formation would be observed compared to the surrogate only case. Table 3.3 lists all of the experiments conducted for this study.

3.3: Results and discussion

3.3.1: Atmospheric Availability of the Select IVOCs

Table 3.1 lists chemical and physical properties of individual compounds investigated as part of this work. Oxidation state of carbon (\overline{OSc}) for each select chemical compound is calculated as $\overline{OSc} = 2O:C - HC$ (Kroll et al., 2011). Figure 3.1 shows a 2-D space with the volatility (saturation concentration C^* , $\mu\text{g m}^{-3}$) as the x-axis and the extent of oxidation of the select IVOCs (oxidation state of carbon) as the y-axis (Donahue et al., 2012). C^* determines the amount of organic aerosol. The volatility ranges are identified with colored bands. In the order of increasing volatility, gray shading refers to extremely low volatility organic compound (ELVOC, $C^* < 3 \times 10^{-4} \mu\text{g m}^{-3}$), which stays almost entirely in the aerosol phase under ambient conditions.

Light red shading stands for low volatility organic compound (LVOC, $3 \times 10^{-4} < C^* < 0.3 \mu\text{g m}^{-3}$). Light green shading represents semi-volatile organic compound (SVOC, $0.3 < C^* < 300 \mu\text{g m}^{-3}$). Light blue shading refers to intermediate volatility organic compound (IVOC, $300 < C^* < 3 \times 10^6 \mu\text{g m}^{-3}$). Yellow shading stands for volatile organic

compound (VOC, $C^* > 3 \times 10^6 \mu\text{g m}^{-3}$). The C^* values are obtained from Donahue et al. 2012. All of the individual compounds studied in this work are labeled on the figure with all compounds in the IVOC range except glycerol and Triethanolamine.

Evaporation mass loss rates of the IVOCs tested are evaluated gravimetrically with individual IVOC evaporation experiments commencing with 200 μl placed into a weighing boat. Benzyl alcohol, DEGBE, n-Tridecane, DBE-5, DPGMEA, DEGEE, and propylene glycol lose more than 95% of their mass within 1 month and Texanol® within 3 months (Abbreviations are defined in Table 3.1). Glyceryl triacetate, diethylene glycol, and n-Heptadecane lose half of their weight within 6 months. Glycerol, triethanolamine, and methyl palmitate lose less than 5% of their mass within six months.

Correlations of the IVOC evaporation rates to physical and chemical properties of the IVOCs are explored in an effort to provide semi-empirical prediction of the evaporation behavior for IVOCs studied. Previous studies show that evaporation rate from inert surfaces correlates well with vapor pressure (Woodrow et al., 1997, 2001; Guth et al., 2004). Later, Mackay and Wesenbeeck (2014) develop a simpler one parameter correlation for the evaporation rate of chemicals as a function of not only vapor pressure, but also molar mass. The relationship agrees with the assumption that the air immediately in contact with the liquid surface achieves a partial pressure of P (Pa). Therefore, the evaporation rate can be estimated as the product of the saturated vapor concentration and a mass-transfer coefficient. Their equation applies only to liquid surfaces that are not

affected by the underlying solid substrate, such as selection of hydrocarbon carrier fluids used in emulsifiable concentrates in pesticide formulations and prediction of evaporation behavior of cleaning solvents applied to surfaces under fairly quiescent conditions.

In the current study, evaporation rate is calculated from the initial loss rate (initial slope) in Figure 3.2 for each individual IVOC. Figure 3.3 applies the correlation from Mackay and Wesenbeeck (2014)'s study and plots molar mass \times vapor pressure versus evaporation rate with the constant designed in our systems for all IVOCs (Eqs.1). Experimental data exhibits a linear trend ($R^2=0.98$), which indicates that the evaporation rates of IVOCs studied in this paper not only depend on their vapor pressures, but also correlate with their molar mass. This work extends the application of Mackay and Wesenbeeck's method (2014).

$$ER = 0.00284 \times VP \times MW \quad (1)$$

where ER is the individual IVOC evaporation rate in g day^{-1} , VP is the vapor pressure in mmHg, and MW is the molar mass in g mol^{-1} .

3.3.2: SOA Formation

As the extent of gas-particle partitioning is a function of organic aerosol concentration, the atmospheric representativeness of a given aerosol formation experiment is related to the final organic aerosol formed during a given experiment. Typically, ambient fine particle organic aerosol concentrations tend to be less than $10 \mu\text{g m}^{-3}$. Rather than invest

in obtaining full data sets necessary for yield curve determinations for just a few IVOCs, it is determined to measure SOA formation from a variety of IVOC precursors. Therefore, the SOA formation observed is used as guidance as to the extent of SOA formation that might be expected from a variety of SOA precursors. The relative amounts of SOA formation from the IVOC precursors provide a strong indication of which IVOC precursors are important (or unimportant) SOA producers warranting further investigation. To calculate the mass concentration of the SOA, the SOA volumes established by SMPS measurements are wall-loss corrected following procedures detailed in Cocker et al. (2001c) and then multiplied by measured SOA density.

3.3.2.1: Adding an IVOC to a Surrogate ROG Mixture

As mentioned in the previous section, the surrogate consists of a simplified mixture designed to represent the major classes of hydrocarbons measured in ambient urban atmospheres, with one compound used to represent each model species used in condensed lumped-molecule mechanism (Carter, 2005). The surrogate is used as a tool to better simulate atmospheric reactivity during SOA and ozone formation in an urban environment. Figure 3.4 shows SOA formation from photo-oxidation of DEGEE in the presence of NO only, H₂O₂ only, and both the surrogate mixture and NO_x. A surrogate/NO_x experiment (no added IVOC) is also provided for comparison. Experimental conditions are summarized in Table 3.4. SOA formation is the highest for conditions that favored greater IVOC consumption, as illustrated in Figure 3.4, where the higher OH radical concentration in the H₂O₂ only experiment is available to consume

more DEGEE (Table 3.4). The second highest hydroxyl radical concentration is generated in the surrogate-NO_x-DEGEE experiment and therefore has the second greatest DEGEE consumption and SOA formation (Table 3.4). Without the presence of the surrogate mixture, the progression of the DEGEE-NO experiment to a point where NO consumption is complete is suppressed, thus delaying the evolution of excess peroxy and hydroperoxy radicals. Therefore, it is not until the end of the DEGEE-NO experiment that conditions favoring SOA formation are achieved and measurable aerosol formation commenced in the relative absence of NO. NO depletion is achieved much earlier with surrogate mixture present. Further, due to the lower reactivity (hydroxyl radical generation) without the surrogate mixture, a smaller amount of DEGEE is consumed under NO only conditions. The surrogate-NO_x run (no additional IVOC) does not form much SOA.

3.3.2.2: SOA Formation from Select Individual IVOCs

Figure 3.5 presents the SOA formation from individual IVOCs when oxidized in the presence of the surrogate, NO_x and UV. SOA mass concentration is normalized by total precursor consumed. One might expect that the selected IVOCs with lower vapor pressures than traditionally studied VOCs would have greater propensity to form SOA. However, these findings demonstrate that half of the select IVOCs did not form appreciable SOA. Benzyl Alcohol, n-Heptadecane, and DEGBE have the most significant aerosol formation, while DEGEE, n-Tridecane, and DBE-5 show moderate aerosol formation. The largest rate of SOA formation occurred within the first two hours of

photo-oxidation, coinciding with highest OH concentrations, estimated from decay of *m*-xylene. The higher the SOA formation is, the faster the formation rate of SOA is during the first two hours of photo-oxidation. The SOA formation from n-Tridecane and DBE-5 are delayed, which may have been due to formation of low-volatility compounds through multi-generation processes.

A series of experiments are conducted with enhanced OH reactivity by injecting 1.0 ppm H₂O₂, which allows for greater consumption of the initial IVOC by offsetting losses in reactivity due to hydroxyl radical consumption. Figure 3.6 illustrates the normalized SOA formation from individual IVOCs with surrogate, NO_x, UV, and H₂O₂. Benzyl Alcohol, n-Heptadecane, DPGMEA, DEGBE, and n-Tridecane all show significant aerosol formation. DEGEE, Propylene Glycol, and DBE-5 show moderate aerosol formation. The SOA formed from DEGEE and DEGBE is observed to decrease slightly during the last 3 hours of the experiments, which may indicate that some semi-volatile species partition back from aerosol phase to gas phase and fragmented during further oxidation (Li and Cocker, 2018). The SOA formations from n-Tridecane, DPGMEA, DBE-5, Propylene Glycol, DEGEE and DEGBE are all delayed, which may be due to formation of low-volatility compounds through multi-generation processes.

Figure 3.7 confirms that more SOA formation occurs for IVOCs in the presence H₂O₂. DPGMEA does not form observable SOA without H₂O₂ addition, but forms appreciable amount of SOA in the presence of H₂O₂. Adding H₂O₂ creates twice and five times the

SOA formation from Benzyl Alcohol and n-Tridecane, respectively. Adding H₂O₂ does not significantly affect SOA formation from n-Heptadecane indicating that the SOA formation is dominated by sufficiently first generation low volatility products which do not react further to form appreciable additional SOA. The other reason could be that some semi-volatile products partition back to gas phase through continuous oxidation.

3.3.2.3: SOA Mass Yields of Select Individual IVOCs

To compare the SOA formation across individual IVOCs, an effective SOA mass yield is calculated for each IVOC using an approach similar to that of Odum et al. (1996, 1997a, 1997b). The definition of the effective SOA mass yield (Y) used in this study is the ratio of the particle wall-loss-corrected SOA mass (ΔM_0) to the estimated mass of IVOC reacted (ΔHC) (Eqs.2).

$$Y = \frac{\Delta M_0}{\Delta HC} \quad (2)$$

The amount of IVOC reacted is calculated by assuming that each IVOC undergoes a first order reaction with the OH radical (Eqs.3),

$$\frac{d[C_i]}{dt} = -k_{OH,C_i}[OH][C_i] \quad (3)$$

where $[C_i]$ is the individual IVOC concentration in $\mu\text{g m}^{-3}$, k_{OH} is the reaction rate constant in $\text{cm}^3 (\text{molecules}\cdot\text{s})^{-1}$, $[OH]$ is the OH radical concentration in molecules cm^{-3} . The reaction rate constants (k_{OH}) for each IVOC are taken from the literature and are listed in Table 3.5. $[OH]$ is estimated using decay of *m*-xylene. Excellent consistency is seen between yields obtained from calculated and measured IVOC decay for IVOCs with

available concentration data (Figure 3.8). SOA yields from photo-oxidation of IVOCs with surrogate and NO_x range from <0% (negligible) to 41% (Table 3.6). SOA yields from photo-oxidation of select IVOCs with surrogate, NO_x , and H_2O_2 range from <1% (negligible) to 56% (Table 3.6). Individual aerosol yield experiments are insufficient to fit empirical two-product models or Volatility Basis Sets (VBS) (Donahue et al., 2012). However, the values obtained still provide insight into those IVOCs that are most likely to form SOA. While the initial hypothesis is that IVOCs would form significant SOA, only Benzyl Alcohol, n-Heptadecane, and DEGBE have yields greater than 0.1 (without additional H_2O_2). Addition of H_2O_2 adds DEGBE, and DPGMEA to the list of SOA precursors with yields > 0.1.

3.3.2.4: SOA Formation from Select IVOC-containing Consumer Products

Figure 3.9 plots the SOA formation from several consumer products in the presence of surrogate and NO_x . SOA formation from corresponding individual IVOCs present in the consumer product is shown as comparison. The IVOC in consumer product quantity matches to the individual IVOC experiment except for laundry detergent and lotion runs, where the Propylene Glycol quantity are 2 times higher than that in individual Propylene Glycol experiments. For the caulk remover without water run, the top three major components (dimethyl glutarate, dimethyl succinate, and dimethyl adipate) in the caulk remover mixture are injected instead of adding the whole mixture. The amount of the three IVOCs injected matches the amount of the three IVOCs present in the caulk remover with water run. Figure 3.9 illustrates that laundry detergent, general purpose

spray cleaner, and paint stripper (from most to least) each forms appreciable amounts of SOA compared to that formed from the surrogate ROG mixture alone while the hand lotion and caulk remover (with or without water) form only minimal amounts of SOA compared to that formed from the surrogate only experiment. General purpose spray cleaner contains DEGBE and more aerosols are formed in the general spray cleaner mixture than by that from DEGBE alone. Similarly, the laundry detergent mixture forms more aerosol than its IVOC, propylene glycol. Both paint stripper and caulk remover contain DBE-5. However, DBE-5 aerosol behaves differently in the two different product mixtures. Paint stripper forms more aerosol than DBE-5 while caulk remover forms fewer aerosols than DBE-5.

Clearly, the presence of other chemicals in the consumer product influences the reactivity and aerosol formation routes. For instance, the paint stripper contains 5% d-limonene, a known reactive compound individually capable of forming significant amounts of SOA (and ozone) (Kundu et al., 2012), which is expected to have an additive effect on the SOA formed from the individual IVOC. The additive effect includes both increased reactivity of the IVOC (More is consumed) as well as the additional SOA produced by the d-limonene itself. This further leads to greater SOA formation as more SOA present increases the expected SOA yield of the compound through increased sorptive partitioning. Conversely, other ingredients in the caulk remover may be acting as a hydroxyl radical scavenger reducing the extent of IVOC oxidation and thus SOA formation from the caulk remover compared to the individual compound itself.

Two consumer products (laundry detergent and lotion) are studied in the presence of the surrogate mixture with enhanced H₂O₂ (Figure 3.10). The hand lotion still produces little SOA while the SOA formation from laundry detergent is greatly enhanced. The SOA enhancement for laundry detergent is consistent with enhancements seen for individual IVOCs (however, SOA formation is much greater than that anticipated from Propylene Glycol). The hand lotion is difficult to inject, which may have led to lower SOA formation than expected from the mixture.

3.3.2.5: Trends in SOA Elemental Composition and SOA Physical Properties

Table 3.1 summarizes the oxygen-to-carbon (O:C) and hydrogen-to-carbon (H:C) ratios along with other physical properties of SOA, including density and volatile fraction remaining (VFR) for all the experiments. VFR ($VFR = d^3/d_0^3$, d (particle final mobility diameter) and d_0 (particle initial mobility diameter)) is used to describe bulk SOA volatility after heating SOA at a fixed temperature (17°C) in a thermodenuder for a short period of time (17s). Figure 3.11 plots Δ O:C against SOA mass concentration. The Δ O:C is calculated by subtracting the initial O:C of SOA forming precursor from the final O:C, which is an averaged value over the last one hour. A general increase of the Δ O:C ratio as the SOA mass concentration increases is observed, suggesting that the amount of SOA formed is dependent on SOA chemical composition. Several experiments, most notably DPGMEA, are observed to have Δ O:C less than zero, attributable to loss of oxygen during fragmentation processes or through dehydration reactions. Figure 3.12 explores the relationship among oxidation of carbon (\overline{OSc}), volatility, and SOA yield for photo-

oxidation of select IVOCs in the presence of surrogate, NO_x , and H_2O_2 . Circle markers are scaled to SOA yield and triangle markers represent the corresponding averaged final one hour $\overline{\text{OSc}}$. $\overline{\text{OSc}}$ increases during the course of the experiment except for DPGMEA ($\overline{\text{OSc}}$ decreases slightly due to fragmentation). However, no significant correlation is found between $\overline{\text{OSc}}$ and yield or between volatility and yield. Figure 3.13 explores the relationship among oxidation of carbon ($\overline{\text{OSc}}$), volatility, and SOA yield for photo-oxidation of select IVOCs in the presence of surrogate and NO_x . Circle markers are scaled to SOA yield and triangle markers represent the corresponding averaged final one hour $\overline{\text{OSc}}$. $\overline{\text{OSc}}$ Increases during the course of the experiment except for DPGMEA, which is due to fragmentation. No general trend is observed between $\overline{\text{OSc}}$ and yield or between volatility and yield. Figure 3.14 (a) and (b) show the relationship of both O:C and $(\text{OS})\bar{c}$ with VFR, respectively. The three values are averaged over the last one hour of the experiments. VFR shows a significant increasing trend with increasing O:C ($R^2=0.92$) and $(\text{OS})\bar{c}$ ($R^2=0.87$), which implies that SOA formation results from formation of lower volatility compounds from photo-oxidation of individual IVOCs and their mixtures.

3.3.3: Ozone Formation

3.3.3.1: Ozone Formation from Select Individual IVOCs

Figure 3.15 presents the results of ozone formation from individual IVOCs with surrogate and NO_x . The final ozone concentrations range from 145 to 222 ppb. DEGEE, Diethylene

Glycol, Glycerol Triacetate, and Propylene Glycol show enhanced O₃ formation, while DBE-5 and DEGBE are similar to the surrogate only O₃ formation, and the presence of n-Tridecane, n-Heptadecane, Benzyl Alcohol, and Texanol® reduces the O₃ formed from the surrogate mixture.

It is important to note that a decrease in ozone formed with the addition of the IVOC does not necessarily indicate that the IVOC will suppress ozone formation in the atmosphere—only that it is negatively impacting the specific surrogate mixture ozone formation. This may be attributed to larger changes in radical concentrations, NO_x loadings, etc. than expected to occur within the more complex ambient atmosphere with its more significant reservoir. This has been observed and discussed previously (Carter, 2011). For example, in the n-Tridecane and n-Heptadecane case, heavy alkanes could be radical inhibitors, which will prevent cycling OH radicals back by generating RONO₂ instead of RO· (Carter, 2011). Therefore, addition of n-Tridecane and n-Heptadecane reduces the overall hydroxyl concentrations available to oxidize both the IVOC and the ozone forming surrogate hydrocarbons relative to the amount of oxidation and ozone that forms in the surrogate photo-oxidation alone. If the reduction is large enough and the experiment is sensitive enough to this reduction in hydroxyl radical then less net O₃ formation will occur when the added IVOC is present. The sensitivity of the experiment to reduced radical levels depends on the conditions of the experiment, and calculations indicate that most of our experiments are more sensitive to reduced radical levels than is the case for

atmospheric conditions where the relative abundance of the IVOC to other VOCs participating in the reaction is lower (Carter, 2011).

As to the Benzyl alcohol and Texanol® case, the ozone formation rate is faster than that of the surrogate but also plateaus at a lower ozone concentration. The probable explanation is that under low NO_x conditions, the availability of NO_x throughout the experiment determines how much ozone will ultimately form. Although the ozone forms faster under this condition, if there is a VOC or IVOC that removes NO_x at a faster rate and the experiment is sensitive enough to NO_x conditions, there will be less NO_x available to form ozone. Once the NO_x is consumed, ozone will stop forming. The experiments measure the effects of the test compounds or mixtures on ozone formation under the chamber environment. Because of different sensitivities to effects on radical levels and other factors, the effects on ozone in the chamber are not exactly the same as their effects on ozone in the atmosphere.

An additional series of experiments with enhanced hydroxyl radical concentration is performed to exercise the performance of the model and offset losses in hydroxyl reactivity in the mixture due to the addition of the IVOC. Figure 3.16 plots the ozone formation for eight IVOCs within the surrogate mixture with enhanced hydroxyl radical concentration (added H₂O₂). These series of experiments are performed following similar methods (test compound plus surrogate mixture, NO_x, and H₂O₂) used to evaluate SOA formation. The formed ozone concentrations range from 135 to 193 ppb. DEGEE and

Propylene Glycol enhances O₃ formation at elevated OH concentration. DBE-5 and DEGBE form comparable ozone with that formed from the surrogate plus H₂O₂ condition. The presence of n-Tridecane, n-Heptadecane, and Benzyl Alcohol reduces the O₃ formed from the surrogate mixture. Even the addition of 1 ppm H₂O₂ does not sufficiently enhance OH production to offset consumption by the IVOCs. The ozone formations decrease at the end of the experiment for photo-oxidation of Benzyl Alcohol and DEGBE, which may be due to depletion of NO_x at the end of the experiments.

Direct comparisons of ozone formation for select IVOCs with and without H₂O₂ are shown in Figure 3.17. Ozone formation rate is faster when adding H₂O₂. Similar amounts of ozone are formed at the end of the experiments, which indicates that the system entered a NO_x limited regime.

3.3.3.2: Ozone Formation from Select IVOCs-containing Consumer Products

Ozone formation for each consumer product (plus surrogate mixture) is presented (Figure 3.18). Only the laundry detergent (15% propylene glycol) significantly influences ozone formation with the laundry detergent increasing ozone formation. These trends are consistent with the impacts of the IVOCs investigated. Propylene glycol (laundry detergent component) in the individual experiments also forces ozone formation in the surrogate mixture upward, while DBE-5 and DEGBE (components of other consumer products studied) have little impact as individual IVOCs on ozone formation. Insufficient chemical reactivity information is available for the components of the complete laundry

detergent simulant (Pareth 25-9 (alcohols, C₁₂₋₁₅, ethoxylated) and fatty coconut oil) to model completely the ozone formation of the laundry detergent plus surrogate mixture. Ozone formation from caulk remover with water forms a little bit more ozone than that without water. The water is not expected to have a significant effect on the gas-phase oxidation chemistry, as the water will disassociate from the IVOCs in caulk remover upon evaporation into the chamber. The total water added to the chamber is only sufficient to raise relative humidity (RH) by approximately 0.007%, which is not expected to have any impact on ozone formation. The small difference in ozone is attributed to slightly different (~10%) amounts of NO_x present in the two experiments. Select consumer products are also evaluated for ozone formation with increased H₂O₂ (Figure 3.19). Hand lotion is found to elevate ozone produced by the surrogate mixture while laundry detergent is found to have little effect with added H₂O₂. It is important to note that the hand lotion and laundry detergent are extremely difficult to inject into the chamber due to their overall low volatility, which may have impacted some of the results for ozone formation from those consumer products. When deviations from the ozone formation of the surrogate are observed, the increase is consistent with that seen individually for propylene glycol.

3.3.3.3: Ozone Modeling Results from the SAPRC-11 Mechanism

The SAPRC-11 mechanism, which includes the rate constant and reactions updates based on current data, is applied to estimate O₃ formation and to evaluate the ability of current

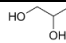
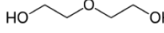
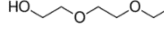
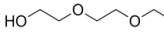
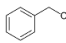
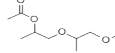
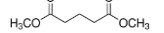
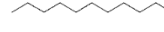
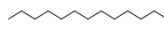
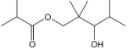
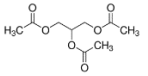
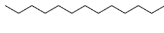
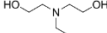
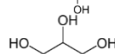
models to accurately predict observed ozone formation for the experiments conducted. Figure 3.20 presents the summary of O₃ prediction results for photo-oxidation of n-Tridecane (n-C₁₃) and n-Heptadecane (n-C₁₇) in the presence of surrogate and NO_x by the SAPRC-11 model. The upper figures compare calculated and measured ozone results (O₃) while the lower figures show differences in the predicted incremental reactivity, which is defined as the change in ozone formation or OH radical levels caused by adding the IVOC to a "base case" experiment, divided by the amount added. The base case experiments refer to ones with only surrogate and NO_x or surrogate, NO_x and H₂O₂ present. The empty square represents the base experiment. The dashed line shows the model calculation for base experiment. The blue diamond indicates test experiment, which adding target IVOC into the base experiment. The solid line expresses model calculation for test experiment. Generally, acceptable agreement is observed between the IVOC experiments within this work and that predicted by the current SAPRC-11 model, with the model giving good simulations (Figure 3. 20), and simulating the impacts of the added compounds within the range observed previously for similar compounds (Carter, 2010). In particular, the model correctly predicts that the relative impacts on ozone formation when adding the test compounds to these experiments is small and generally within experimental variability. This indicates that this mechanism may be adequate for the purpose of examining the gas-phase results of the experiments carried out for this study.

3.4: Conclusion

The evaporation rates of 14 IVOCs that are also classified as LVP-VOCs are measured. Half of these IVOCs lose more than 95% of their mass within a month suggesting that these compounds, which are exempted from VOC regulations as LVP-VOCs, may be evaporate under ambient conditions for SOA and ozone formation. SOA formations from the individual IVOCs studied vary widely with nearly half of the IVOCs explored not forming measurable SOA while other IVOCs producing appreciable SOA. Further detailed studies are required to determine functional relationships of other IVOC compound types to improve forecasting of ability of other types of IVOCs to form SOA. Ozone formations from several individual IVOCs are suppressed, which indicates that the IVOCs act as either radical inhibitors or removed NO_x at a faster rate than the surrogate mixture. The current SAPRC-11 model predicts ozone formation from select IVOCs well, and the current maximum incremental reactivity (MIR) values associated with the compounds are expected to be good. The addition of lab created generic consumer products (general purpose spray cleaner, paint stripper, caulk remover, laundry detergent, and hand lotion) has a weak influence on ozone formation from the surrogate mixture but strongly affects SOA formation. Other components, beyond the individually identified IVOCs also strongly contribute to aerosol formation as the total aerosol formation observed could not be explained solely by the individual aerosol forming IVOCs studied. The overall SOA and ozone formation of the generic consumer product could not be explained solely by analyzing the results of the pure IVOC experiments.

Tables & Figures

Table 3. 1: Chemical and physical properties of the select IVOCs tested.

IVOC Compound ^a Name	CAS #	Chemical Formula	Molecular Structure	Boiling Point ^b	Vapor Pressure ^a	\overline{OSc}_o ^c	$\log_{10}(C^*)$
				°C	mm Hg		
Propylene Glycol	57-55-6	C ₃ H ₈ O ₂		188	0.08	-1.3	5.72
Diethylene Glycol	111-46-6	C ₄ H ₁₀ O ₃		245	0.002	-1.0	4.51
Diethylene Glycol Ethyl Ether (DEGEE)	111-90-0	C ₆ H ₁₄ O ₃		202	<0.1	-1.3	5.96
Diethylene Glycol Monobutyl Ether (DEGEBE)	112-34-5	C ₈ H ₁₈ O ₃		230	0.02	-1.5	5.28
Benzyl Alcohol	100-51-6	C ₇ H ₈ O		205	0.094 @ 25 °C	-0.9	5.74
Dipropylene Glycol Methyl Ether Acetate (DPGMEA)	88917-22-0	C ₉ H ₁₈ O ₄		209	0.08	-1.1	5.91
Dimethyl Glutarate (DBE-5)	1119-40-0	C ₇ H ₁₂ O ₄		215	0.097	-0.6	4.33
n-Tridecane (n-C ₁₃)	629-50-5	C ₁₃ H ₂₈		234	0.08 @25 °C	-2.2	5.74
n-Heptadecane (n-C ₁₇)	629-78-7	C ₁₇ H ₃₆		302	<0.001	-2.1	4.61
2,2,4-Trimethyl-1,3-Pentanediol Monoisobutyrate (Texanol®)	25265-77-4	C ₁₂ H ₂₄ O ₃		244	0.01	-1.5	4.64
Glyceryl Triacetate	102-76-1	C ₉ H ₁₄ O ₆		260	0.0025 @ 25 °C	-0.2	4.50
Methyl Palmitate	112-39-0	C ₁₇ H ₃₄ O ₂		417	0.038 @ 25 °C	-1.8	2.90
Triethanolamine	102-71-6	C ₆ H ₁₅ NO ₃		335	8.38e-6 @ 25 °C	-1.5	1.80
Glycerol	56-81-5	C ₃ H ₈ O ₃		290	0.003 @50 °C	-0.7	1.83

a. All the chemicals are purchased from Sigma-Aldrich ($\geq 95.0-99.0\%$);

b. Values are obtained from ACD/Labs Percepta Predictors—Software Modules;

c. \overline{OSc}_o is calculated based on the molecular structure of the IVOCs studied.

Table 3. 2: Formulation recipes of consumer products tested.

Product Name	Formulations (weight percent)
Laundry detergent	51% water; 15% propylene glycol; 5% coconut fatty acid; 25% Pareth 25-9; 4% triethanolamine.
General-Purpose Spray Cleaner	90.2% water; 5% diethylene glycol monobutyl ether; 0.5% tetrasodium EDTA; 1% ethylene glycol butyl ether; 3% cocamidopropylamine oxide (34% active); 0.3 % triethanolamine.
Caulk Remover	30% dimethyl glutarate, 10% dimethyl succinate, 5% dimethyl adipate, 1% ethanolamine, 1% ethylene glycol, 53% water.
Paint Stripper Gel	40% N-methylpyrrolidone, 30% dimethyl glutarate, 20% dimethyl adipate, 5% PEG-15 cocamine, 5% d-limonene.
Hand Lotion	86.67% water; 4% propylene glycol; 2% glycerol; 0.25% Carbopol Ultrez 20 Polymer; 0.28% Chlorphenesin Powder; 0.25% Methylparaben; 0.2% Xanthan Gum; 0.5% Sorbitan Laurate; 0.25% Behenyl Alcohol; 1% Petrolatum; 4% Squalane; 0.25% Dimethicone; 0.35% Arginine.

Table 3. 3: List of experiments.

Compound	IVOC ^a	NO ^b	NO ₂ ^b	Surr ^c	H ₂ O ₂ ^b	Time ^d	Density ^e	O ₃	SOA	O:C ^f	H:C ^f	VFR ^f
	ppb	ppb	ppb	ppmC	ppm	mins	g/cm ³	ppb	µg/m ³			
DEGEE ^g	40.0	26.0	10.4	1.1	*	540	1.5	221.7	22.7	-	-	0.34
Diethylene Glycol	80.0	20.6	9.4	1.1	*	484	1.5	205.2	2.6	-	-	0.40
Propylene Glycol	80.0	23.6	9.7	1.1	*	413	1.6	200.6	0.2	-	-	0.30
S1	*	23.3	10.1	1.1	*	413	1.5 ^h	175.5	0.6	-	-	-
DEGEE ⁱ	40.0	20.2	10.2	1.1	*	480	1.5	177.8	48.8	-	-	0.42
n-C ₁₃ ^j	40.0	20.1	9.9	1.1	*	570	1.3	160.0	14.4	-	-	0.41
S1	*	20.2	9.5	1.1	*	420	1.5 ^h	182.8	2.3	-	-	0.44
n-C ₁₇ ^k	40.0	23.0	10.8	1.1	*	480	1.0	172.3	104.6	-	-	0.30
DBE-5 ^l	160.0	18.0	13.4	1.1	*	505	1.4	178.7	9.9	-	-	0.36
Benzyl Alcohol	80.0	20.3	10.9	1.1	*	480	1.4	144.5	76.9	0.86	1.45	0.71
n-C ₁₃ ^j	40.0	17.8	12.7	1.1	1	493	1.4	163.2	82.2	0.30	1.78	-
S2	*	17.9	12.6	1.1	1	493	1.5 ^h	183.4	15.2	-	-	-
DEGEE	40.0	*	*	*	1	403	1.6	-	49.1	0.69	1.67	-
DEGEE	40.0	25.0	*	*	*	525	1.6	86.8	4.7	0.60	1.82	-
Benzyl Alcohol	80.0	20.1	8.3	1.1	1	380	1.4	134.9	152.9	0.80	1.45	-
DPGMEA	40.0	21.5	9.5	1.1	*	478	1.4	185.1	6.0	0.24	1.30	-
Texanol	80.0	17.6	10.5	1.1	*	472	1.4	163.5	1.1	0.32	1.69	-
Glyceryl triacetate	80.0	20.4	9.1	1.1	*	425	1.4	169.6	0.7	0.63	1.37	-
DBE-5	160.0	20.4	10.9	1.1	1	418	1.5	182.0	7.7	0.72	1.77	-
Propylene Glycol	80.0	21.3	11.2	1.1	1	380	1.5	190.5	5.6	0.55	1.46	-
DEGEE	40.0	21.9	9.5	1.1	1	422	1.4	193.1	34.9	1.16	1.93	-
DEGEE	40.0	18.9	9.7	1.1	1	450	1.3	179.9	91.5	0.83	1.92	-
Caulk Remover Mixture	160.0	16.2	7.6	1.1	*	479	1.4	167.0	2.5	0.22	1.35	-
S1	*	16.3	7.2	1.1	*	479	1.5 ^h	163.1	3.0	-	-	-
Paint Stripper Mixture	160.0	17.1	9.6	1.1	*	509	1.4	158.8	29.4	0.45	1.51	-
General Purpose Spray Cleaner Mixture	40.0	15.1	8.5	1.1	*	488	1.4	161.8	61.6	0.48	1.65	-
Caulk Remover Mixture w/out water added	160.0	15.5	5.9	1.1	*	465	1.4	153.3	1.8	0.50	1.51	-
n-C ₁₇ ^k	40.0	15.8	8.1	1.1	1	426	1.5	160.2	108.7	0.53	1.44	0.25
DPGMEA	40.0	11.8	6.9	1.1	1	398	1.1	130.4	82.3	0.24	1.80	-
Laundry Detergent	160	16.8	9.0	1.1	*	339	1.4	183.7	53.8	0.25	1.75	0.04
Laundry Detergent	160	12.0	10.9	1.1	1	328	1.4	147.7	203.1	0.20	1.82	-
Hand Lotion	160	12.7	7.4	1.1	*	325	1.3	160.2	1.4	0.42	1.59	0.32
Hand Lotion	160	15.9	8.6	1.1	1	380	1.4	179.6	7.2	0.48	1.56	0.27

A: West reactor; B: East reactor; “-”: Data not collected; “*”: Chemicals not injected; O:C: Oxygen-to-carbon ratio; H:C: Hydrogen-to-carbon ratio; VFR: Volume fraction remaining; S1: Surrogate-NO_x only runs; S2: Surrogate-NO_x-H₂O₂ only run;

- Target concentrations provided. Typically, actual concentrations in these chamber systems are within 5% of target concentration.
- Initial NO, NO₂, and H₂O₂ concentration;
- Initial surrogate reactive organic gas (ROG) mixture concentration;
- Irradiation time;
- Averaged density over the entire course of the experiment;
- Data represent the average over the final one hour of the experiment;
- Diethylene Glycol Ethyl Ether;
- Assumed density of 1.5 g cm⁻³ for S1 and S2 experiments based on EPA1894 density result;
- Diethylene Glycol Monobutyl Ether;
- n-Tridecane;
- Heptadecane;
- Dimethyl Glutarate.

Table 3. 4: Experimental conditions for runs listed in Figure 3.4.

Experimental conditions	Surrogate ₀ ^a (ppmC)	NO ^b (ppb)	NO ₂ ^b (ppb)	DEGEE ₀ ^c (ppb)	OH (molec cm ⁻³)	ΔDEGEE ^d (μg m ⁻³)	ΔM ^e (μg m ⁻³)	Yield
Surrogate + NO _x	1.1	~16	~9	-	1.52E+08	-	2.3	-
DEGEE + NO	-	~20	-	40	6.49E+07	168.0	4.6	0.03
Surrogate + NO _x + DEGEE	1.1	~16	~9	40	9.96E+07	338.2	23.0	0.07
DEGEE + H ₂ O ₂	-	-	-	40	3.66E+8	360.9	49.1	0.2

a: Initial surrogate ROG mixture concentration; b: Initial NO and NO₂ concentration; c: Initial DEGEE concentration; d: DEGEE reacted; e: SOA formed

Table 3. 5: Reaction rate constant for each individual IVOC tested.

IVOC	k _{OH} (cm ³ /molecule·s)
Propylene Glycol	2.15E-11
Diethylene Glycol	2.75E-11
DEGEE	5.16E-11
DEGBE	7.44E-11
n-Tridecane	1.63E-11
n-Heptadecane	2.32E-11
DBE-5	3.50E-12
Benzyl Alcohol	2.80E-11
DPGMEA	3.36E-11
Texanol®	1.29E-11
Glyceryl Triacetate	8.49E-12

Table 3. 6: Yields for individual IVOC runs with surrogate and NO_x in the absence and presence of H₂O₂.

Compound	H ₂ O ₂	ΔHC(μg m ⁻³)	ΔM(μg m ⁻³)	Yield
Benzyl Alcohol	Y ^b	272.11	152.90	0.56
	N ^c	186.91	43.20	0.41
n-Heptadecane ^a	Y	332.89	109.45	0.33
	N	199.86	103.60	0.38
DEGBE	Y	265.56	91.50	0.28
	N	293.13	47.80	0.16
DPGMEA ^a	Y	301.34	80.27	0.27
	N	255.06	6.00	0.02
n-Tridecane	Y	381.91	82.20	0.22
	N	183.76	14.69	0.08
DEGEE	Y	355.87	34.90	0.10
	N	338.18	23.00	0.07
Propylene Glycol	Y	81.14	5.60	0.07
	N	84.93	0.16	0.00
DBE-5	Y	181.41	7.70	0.04
	N	158.00	9.73	0.06
Diethylene Glycol	N	309.95	2.58	0.01
Texanol®	N	151.29	1.10	0.01
Glyceryl Triacetate ^a	N	713.91	0.63	0.00

a: Initial concentration based on assumption that 100% IVOC is injected into chamber; b: With H₂O₂; c: Without H₂O₂.

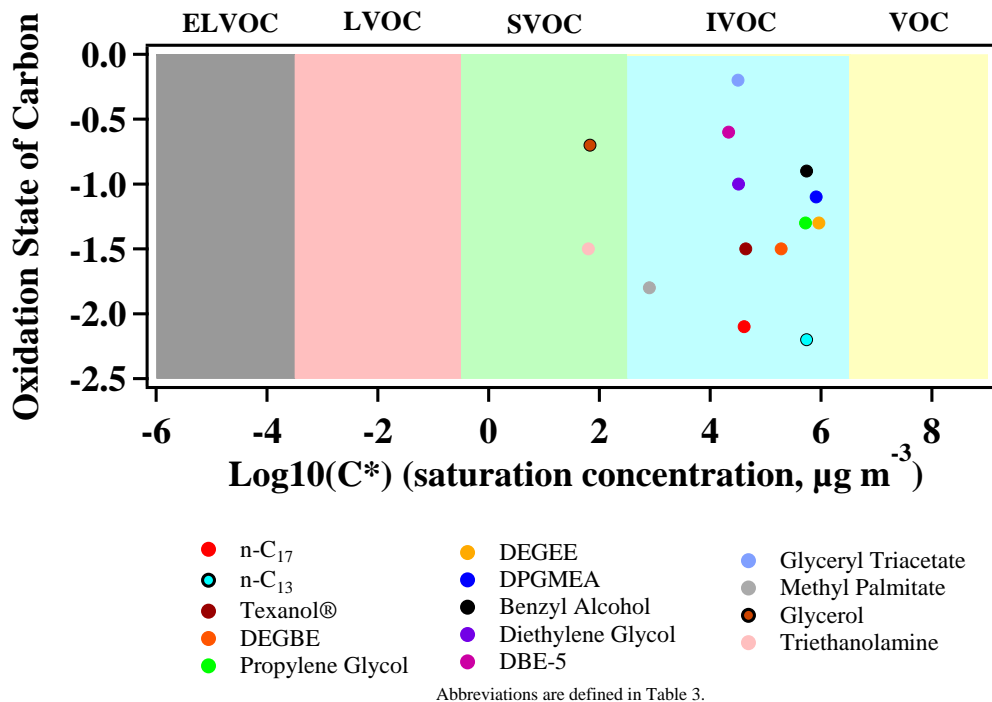


Figure 3. 1: Volatility and the extent of oxidation of the select IVOCs.

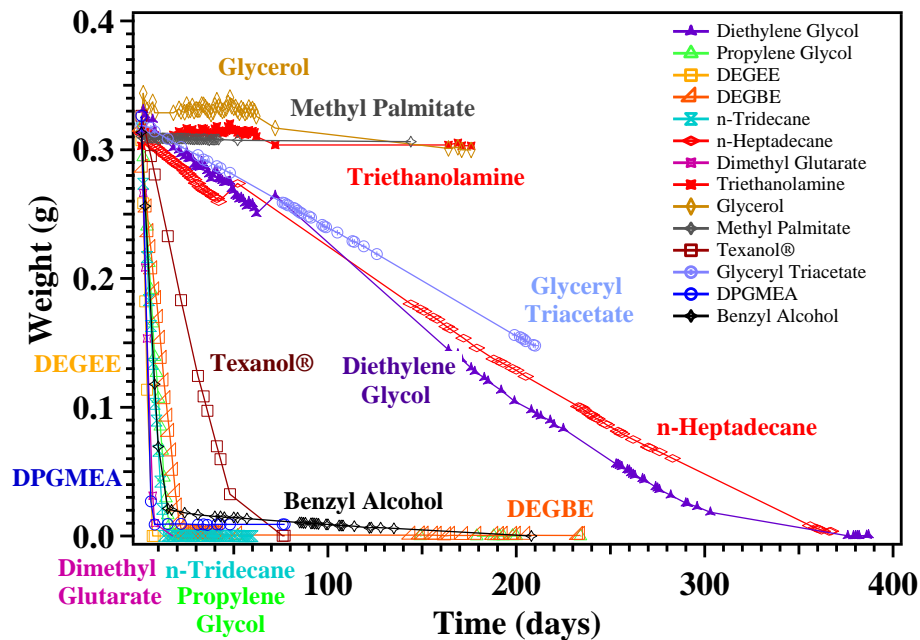


Figure 3. 2: Weight loss of the select IVOCs in Evaporation chambers (Abbreviations are defined in Table 3.1).

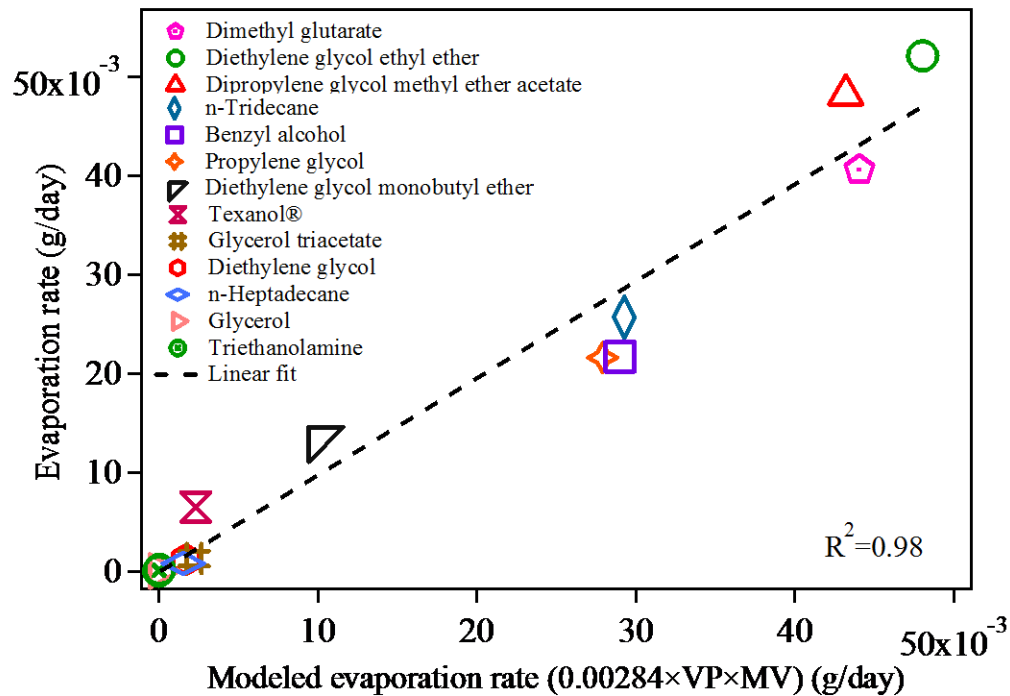


Figure 3. 3: Evaporation rate measured by the experiments and predicted by the evaporation model of the select IVOCs (calculated from weight loss results (Figure 3.2).

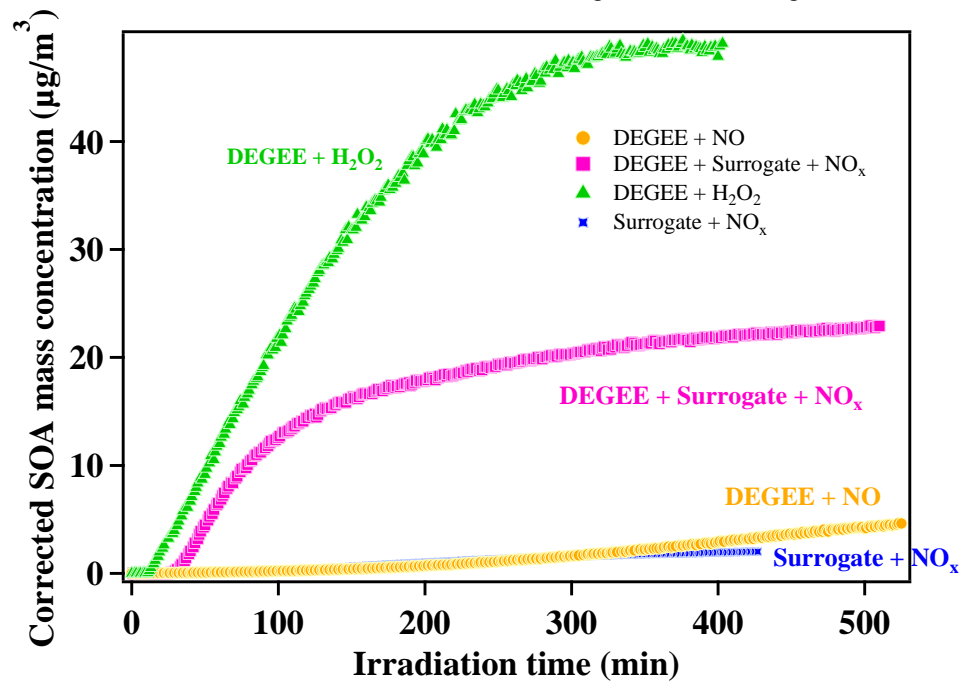


Figure 3. 4: Comparison of SOA formations from three different photo-oxidation systems.

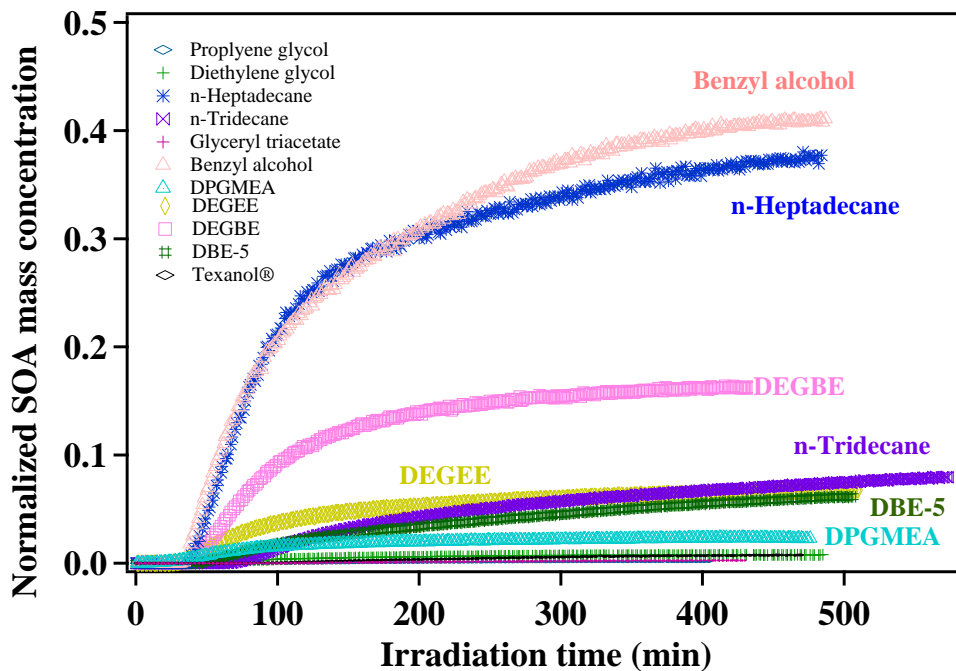


Figure 3. 5: Normalized SOA formation by total precursor consumed from select individual IVOCs with surrogate and NO_x .

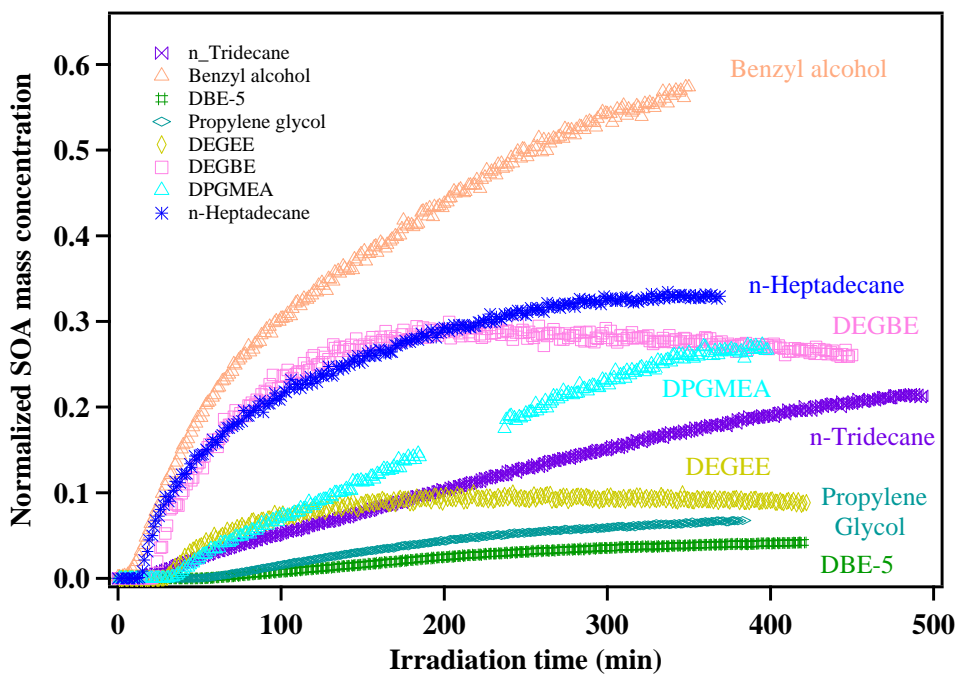


Figure 3. 6: Normalized SOA formation by total precursor consumed from individual IVOCs with surrogate, NO_x , and H_2O_2 .

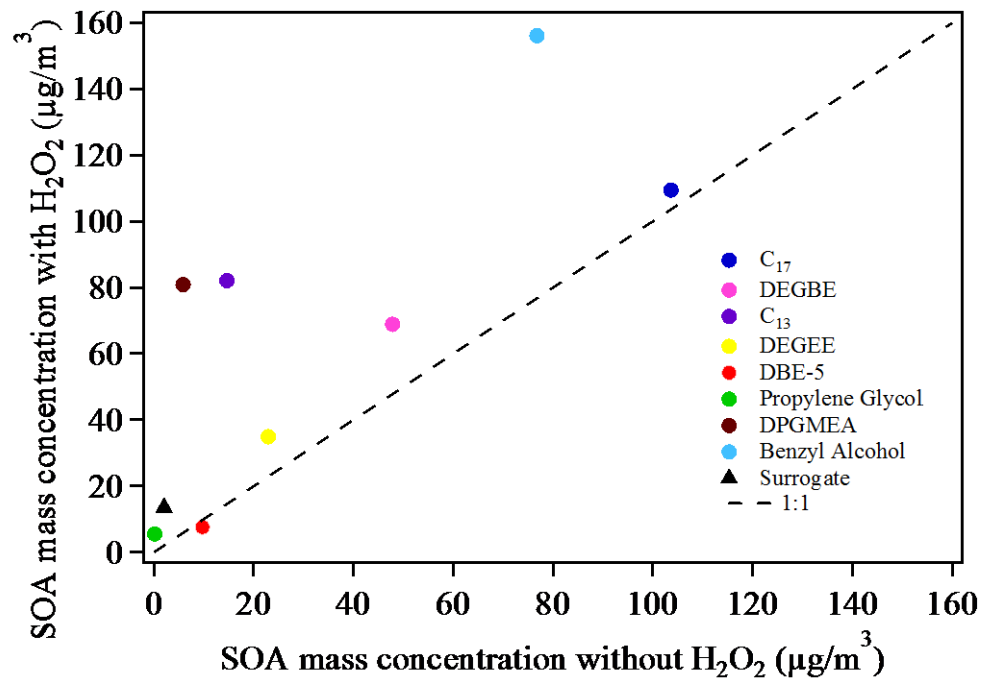


Figure 3. 7: Comparison of SOA formation with and without H₂O₂ for select IVOCs in the presence of NO_x and surrogate.

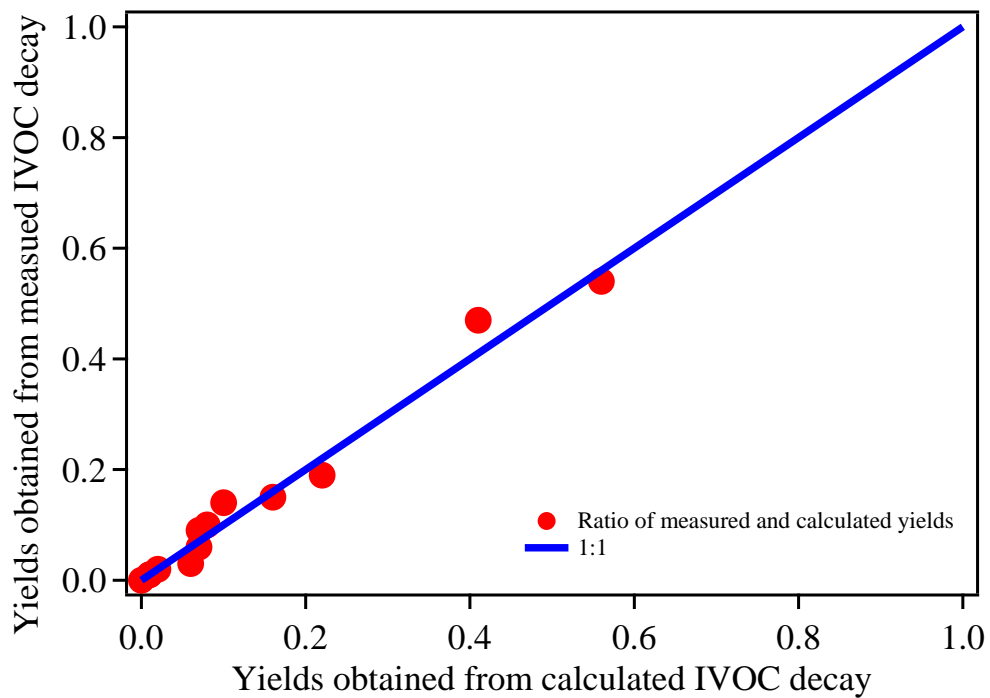


Figure 3. 8: Comparison of yields obtained from calculated and measured IVOC decay.

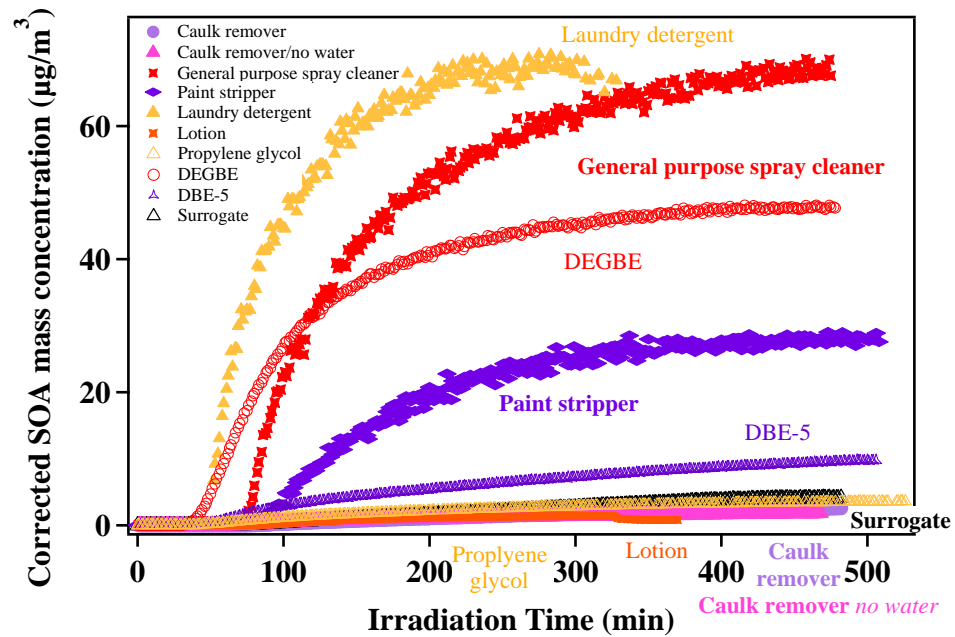


Figure 3. 9: Comparison of SOA formation from single IVOCs with that from mixtures in the presence of surrogate and NO_x .

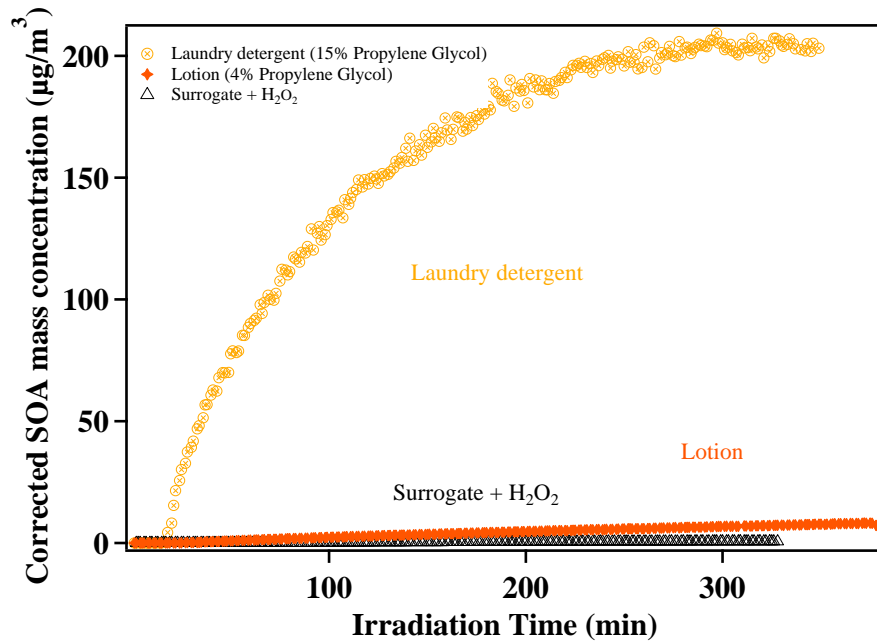


Figure 3. 10: SOA formation from IVOCs containing generic consumer products with surrogate, NO_x , and H_2O_2 .

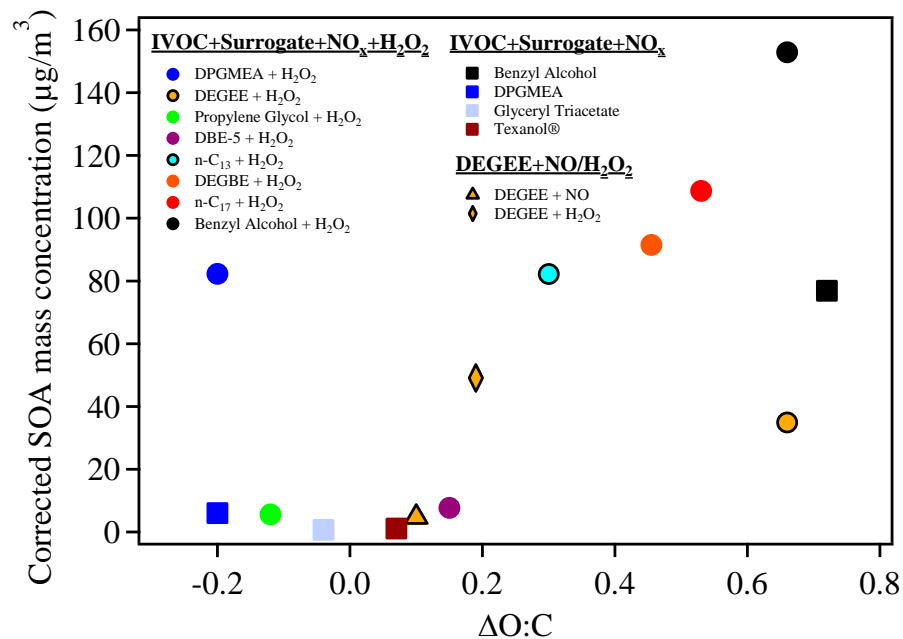


Figure 3.11: Correlation between the change of oxygen to carbon ratio ($\Delta O:C$) and SOA mass concentration for all the runs producing $> 2 \mu\text{g m}^{-3}$ of aerosol with available AMS data. Data collected under different experimental conditions are identified by different markers.

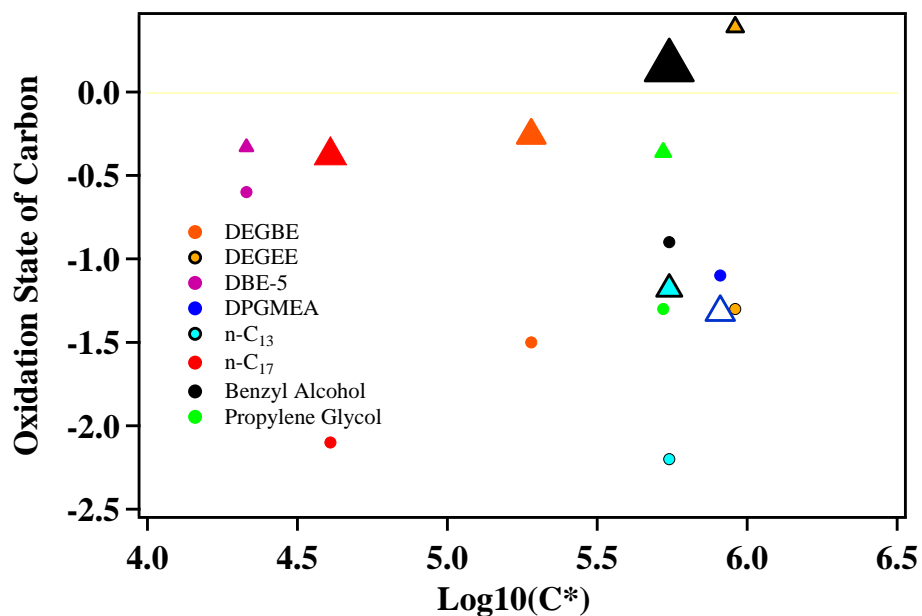


Figure 3.12: Saturation concentration and the extent of oxidation of photo-oxidation of select IVOCs in the presence of surrogate, NO_x, and H₂O₂. Circle marker represents the \overline{OS}_c of SOA forming precursor. Triangle marker displays the averaged final one hour \overline{OS}_c and its size is scaled to corresponding SOA yield.

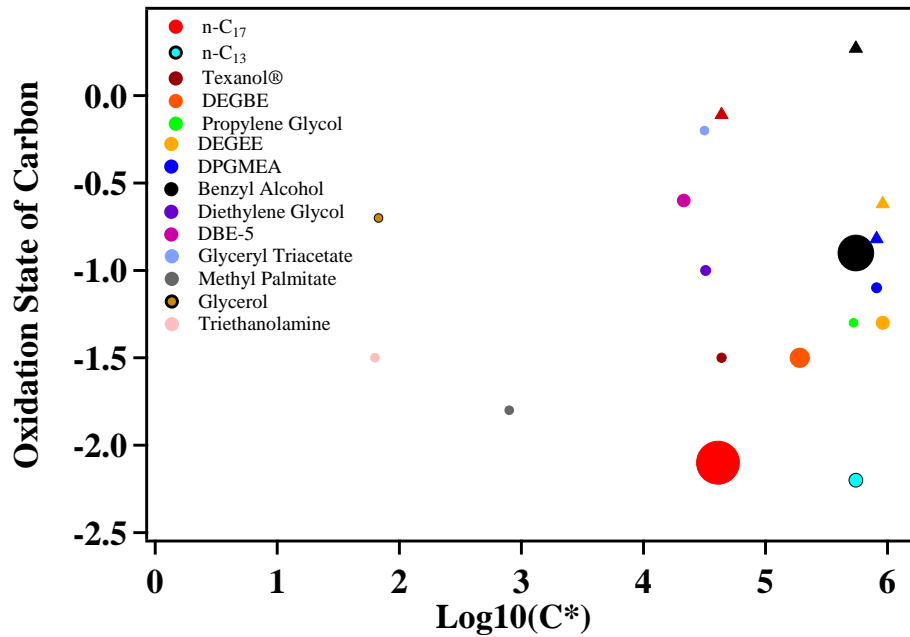


Figure 3. 13: Saturation concentration and the extent of oxidation of photo-oxidation of select IVOCs in the presence of surrogate and NO_x . Circle marker represents the \overline{OS}_c of SOA forming precursor and its size is scaled to corresponding SOA yield. Triangle marker displays the averaged final one hour \overline{OS}_c .

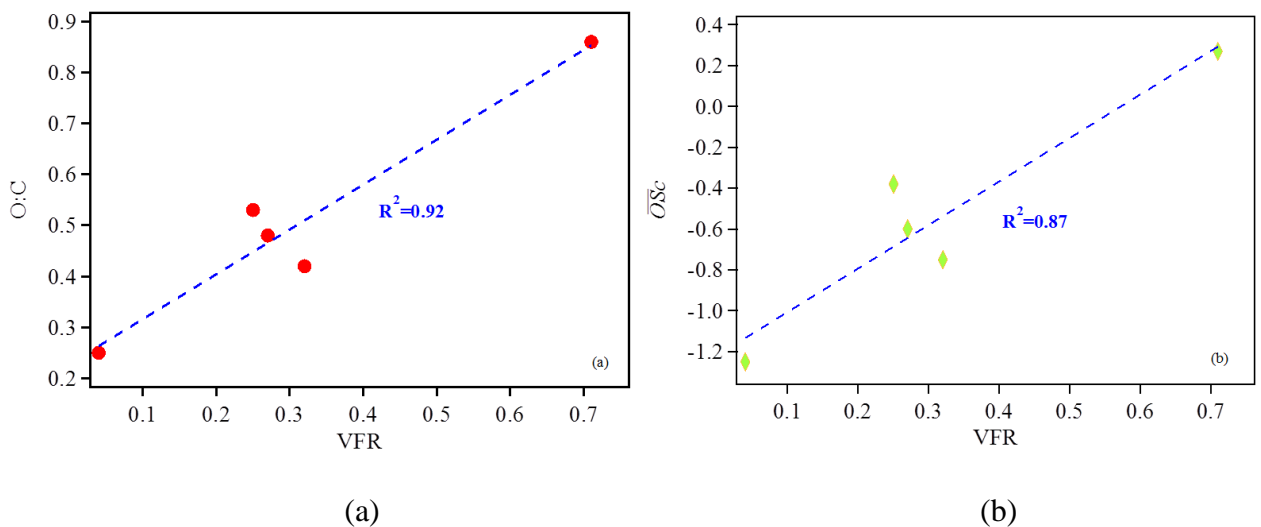


Figure 3. 14: Relationship between (a) SOA volatility and O:C and (b) SOA volatility and oxidation state (\overline{OS}_c) from individual IVOCs and their mixtures photooxidation under low NO_x condition.

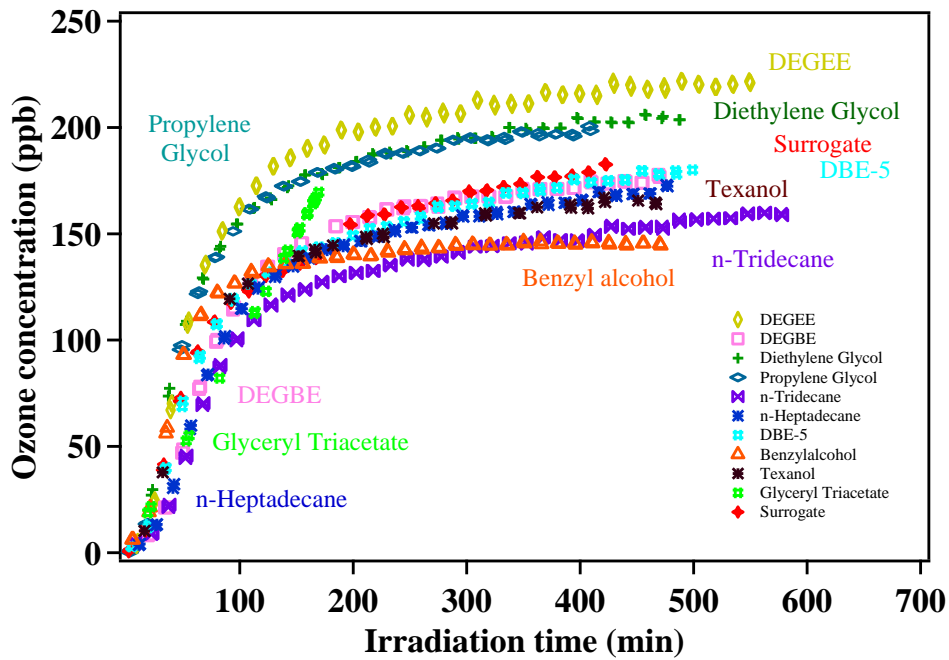


Figure 3. 15: Ozone formation from individual IVOCs with surrogate and NO_x .

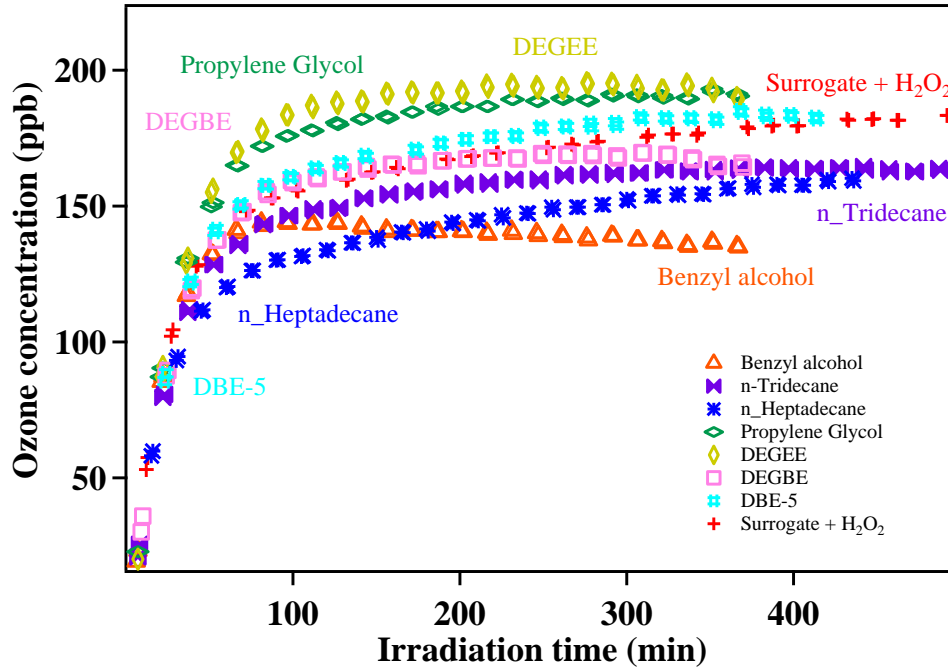


Figure 3. 16: Ozone formation from individual IVOCs with surrogate, NO_x , and H_2O_2 .

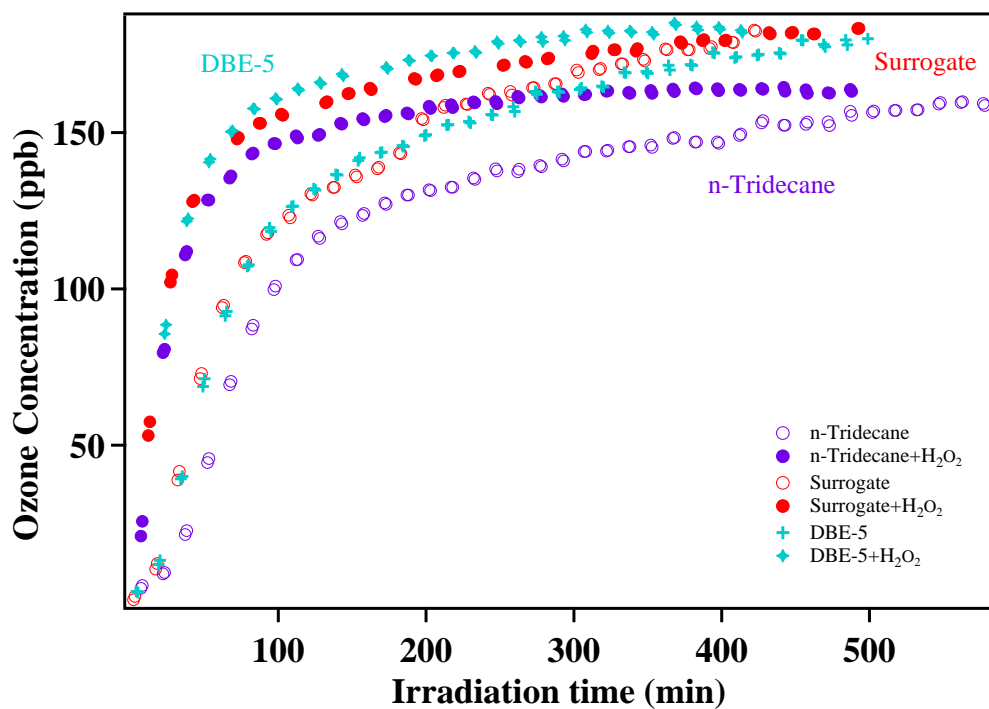


Figure 3. 17: Typical ozone formation comparison between runs with or without H₂O₂.

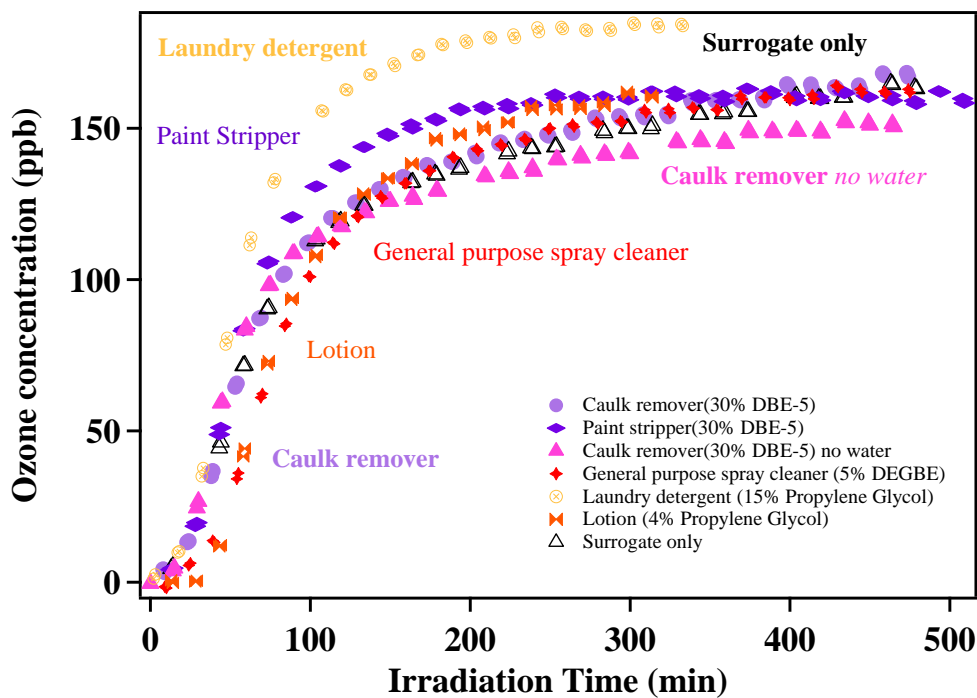


Figure 3. 18: Ozone formation trends for each consumer product injected into surrogate mixture.

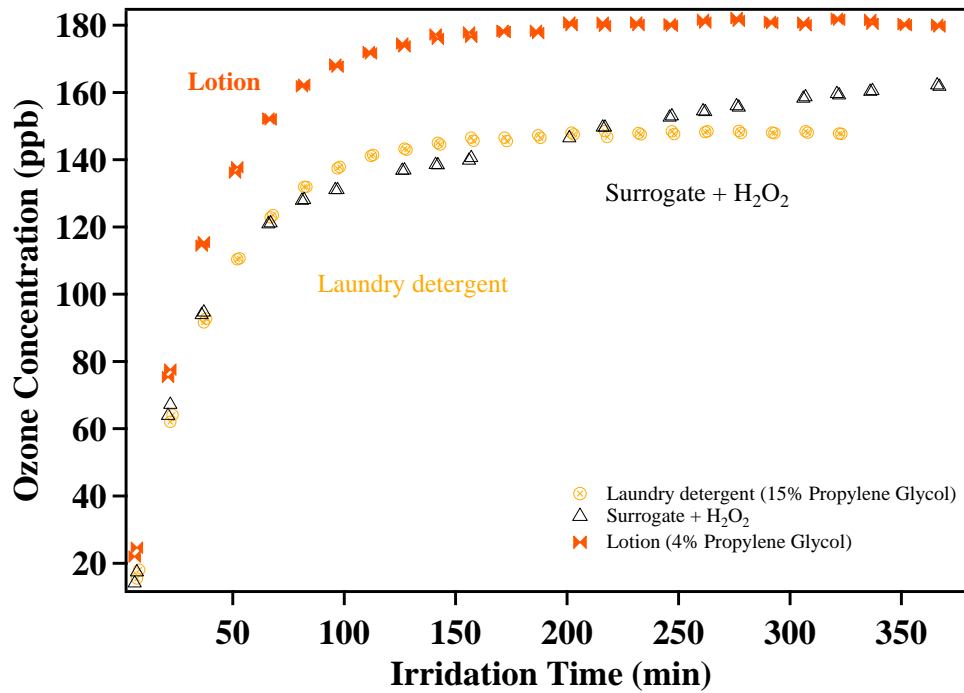
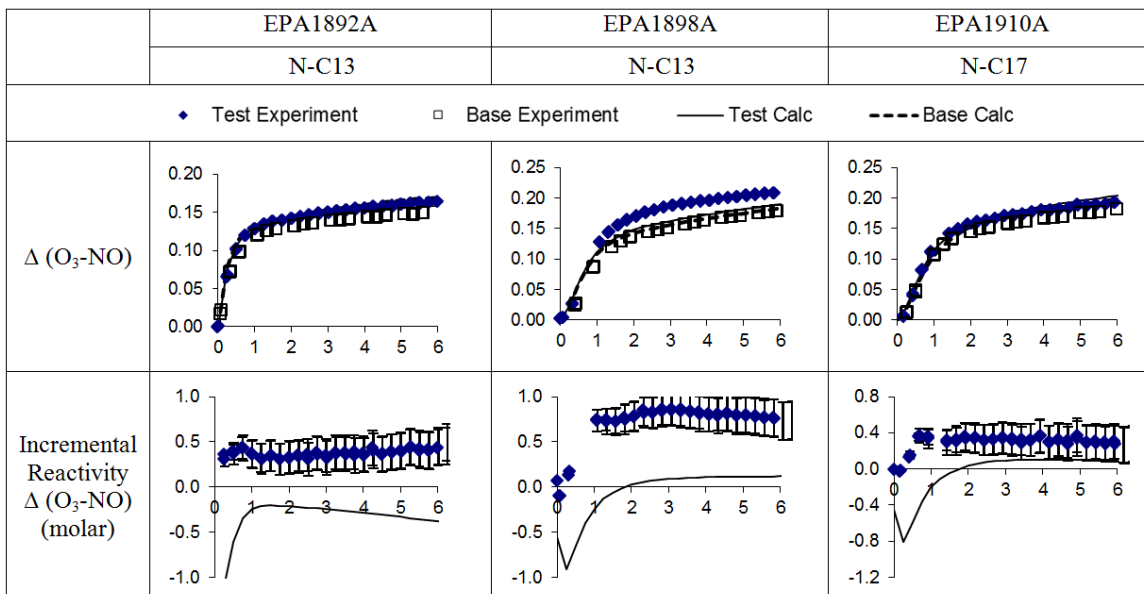
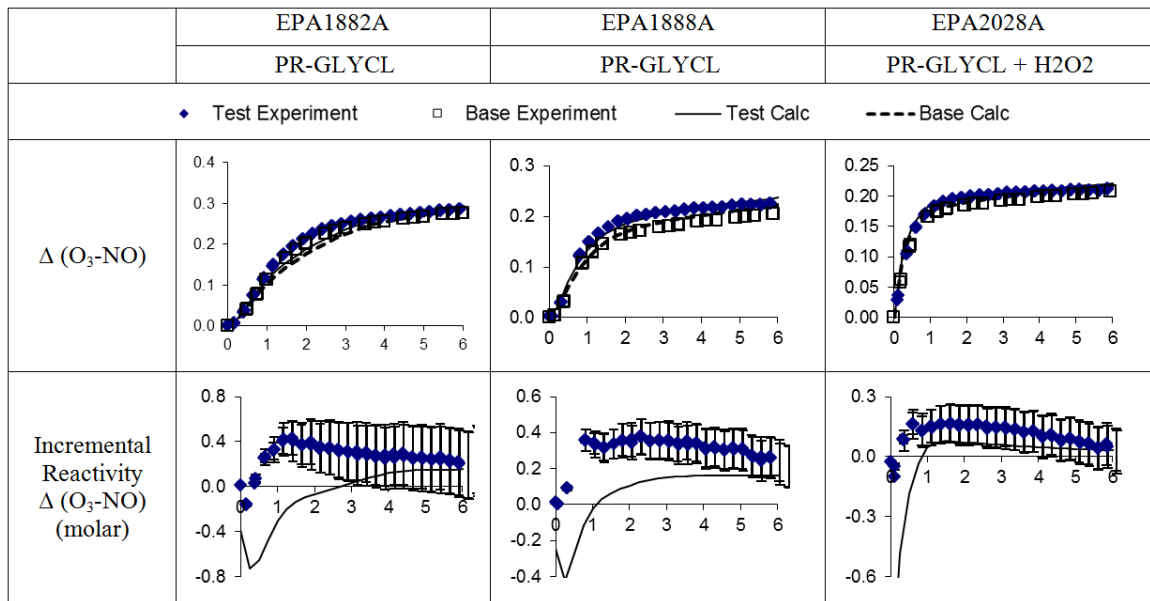
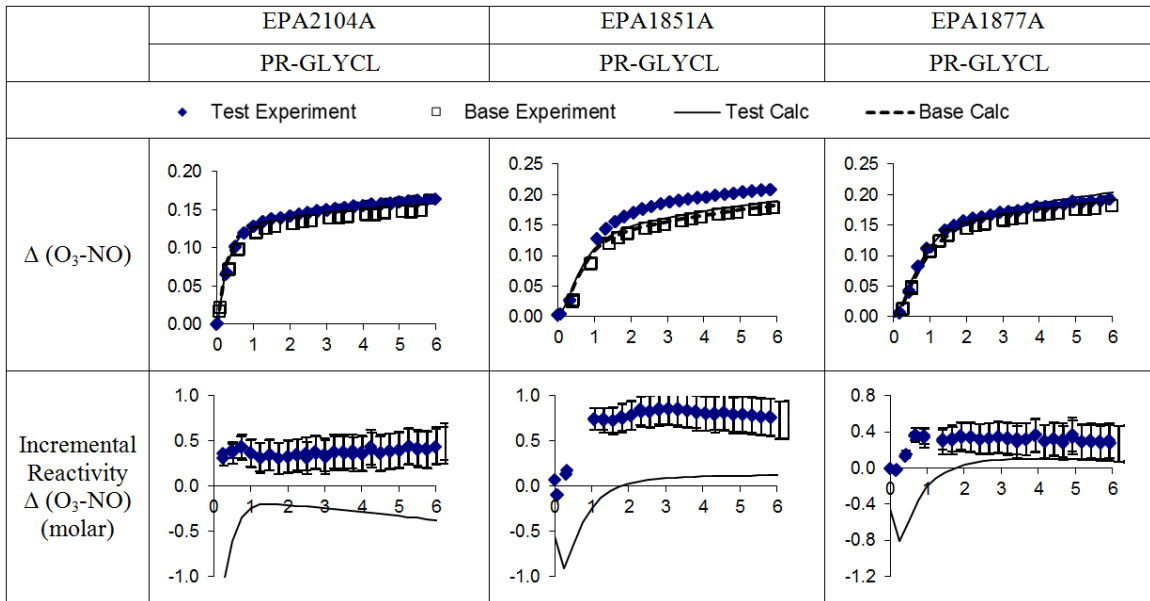
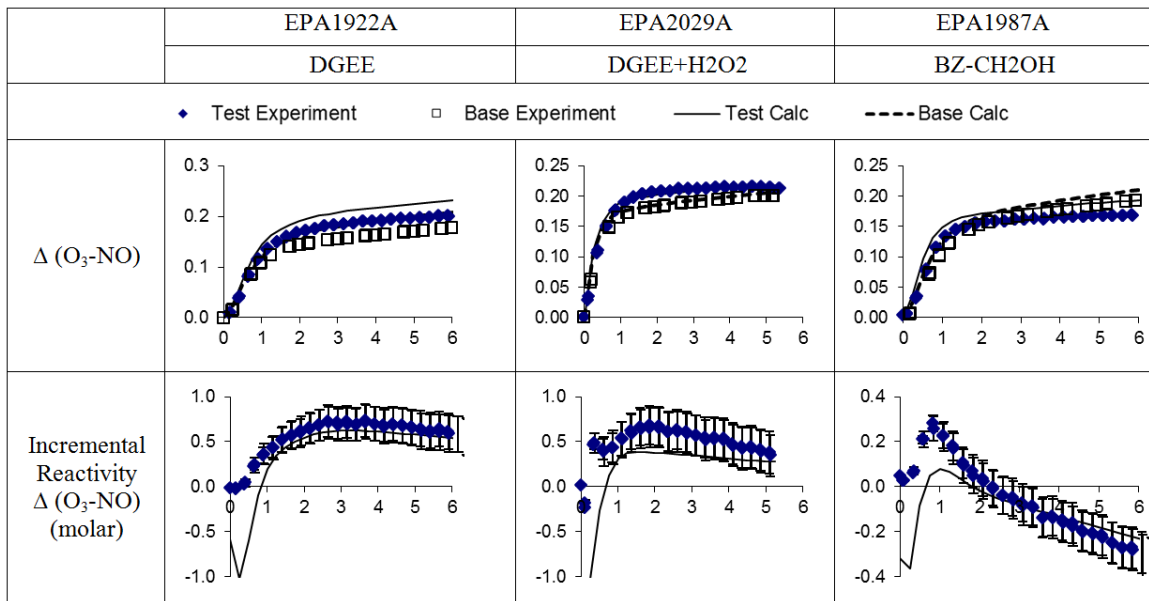
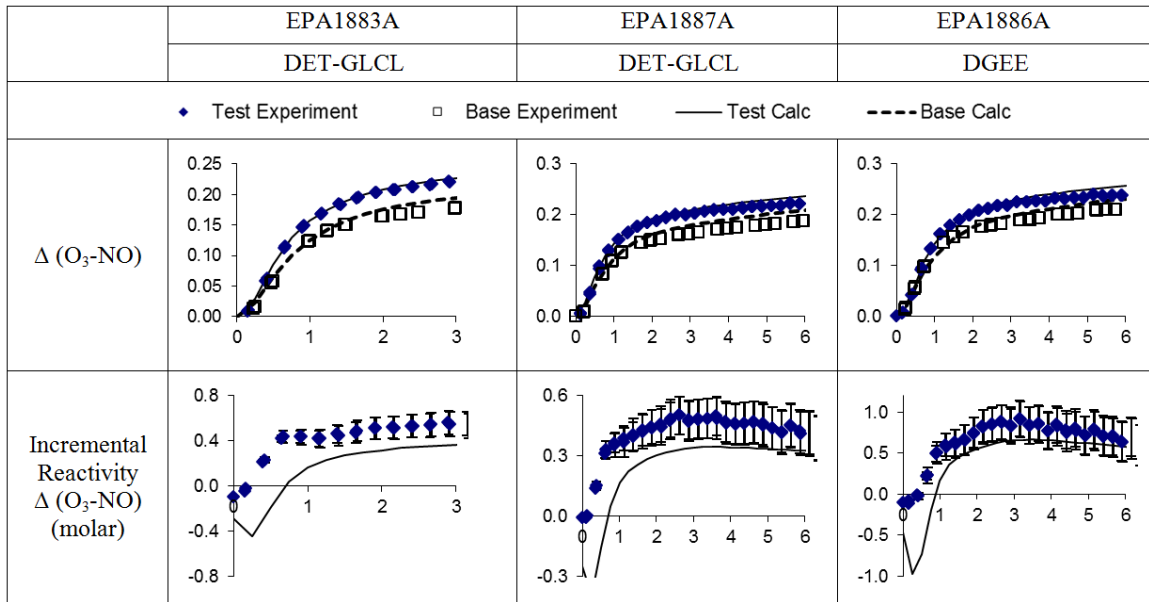
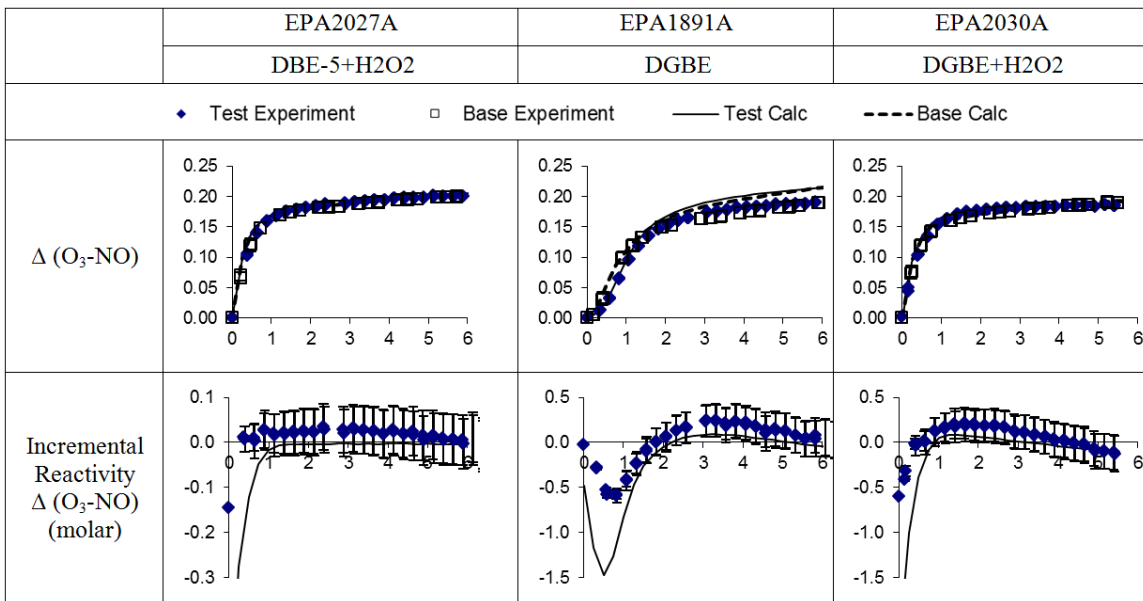
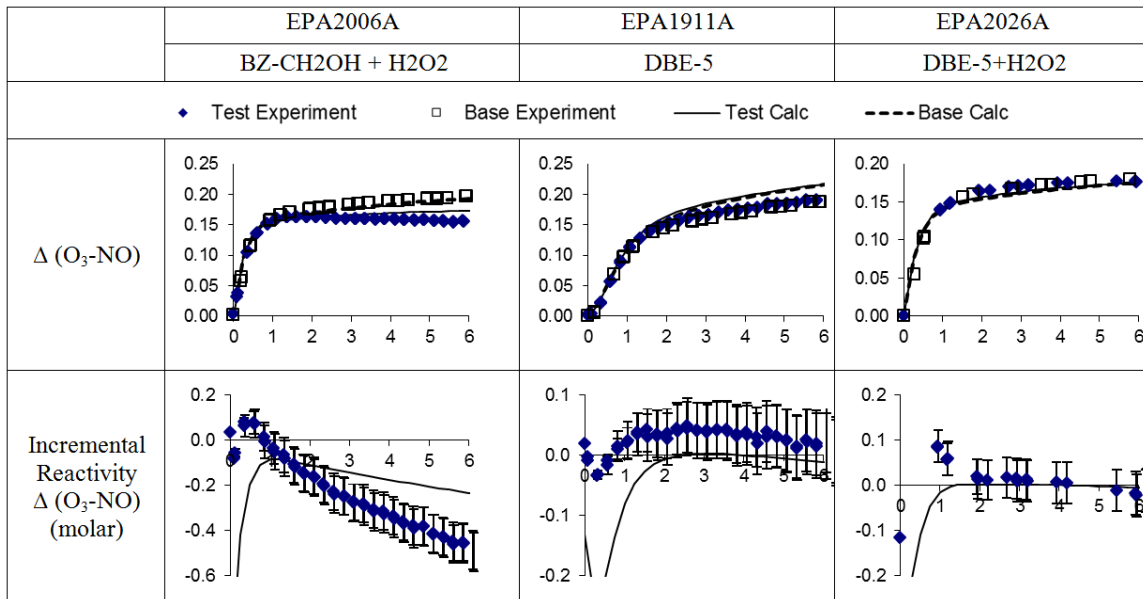


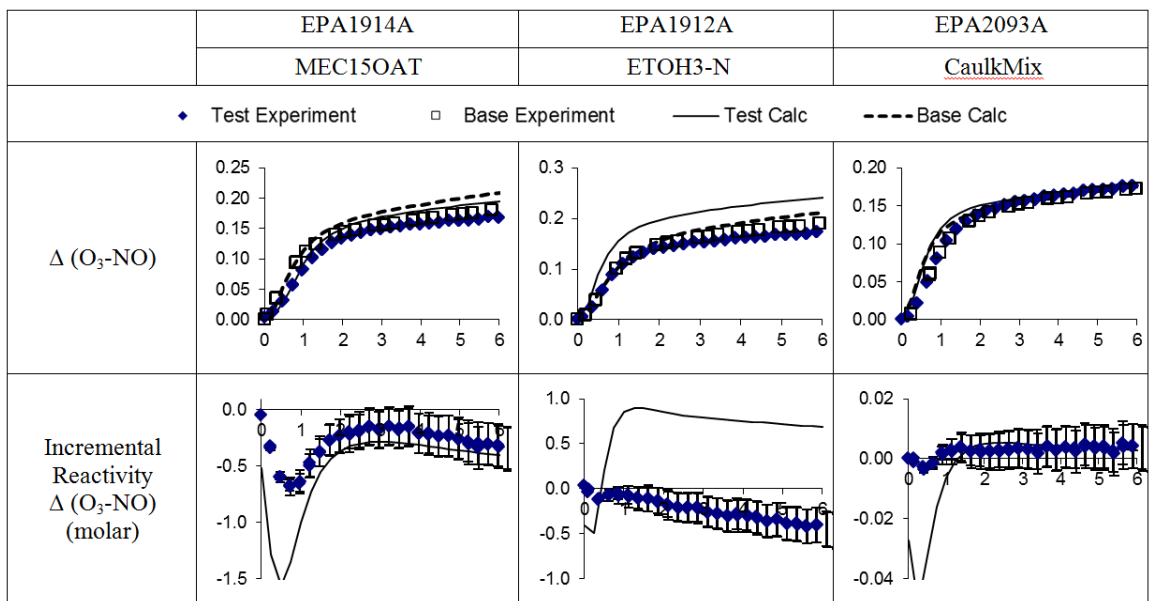
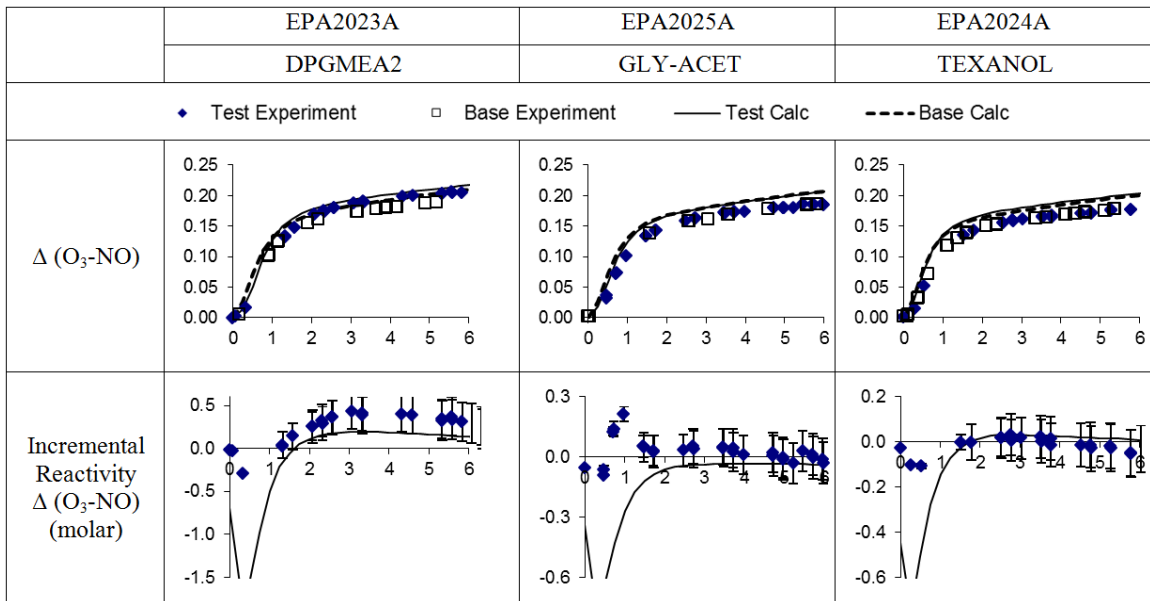
Figure 3. 19: Ozone formation from consumer products in surrogate mixture with enhanced H₂O₂.











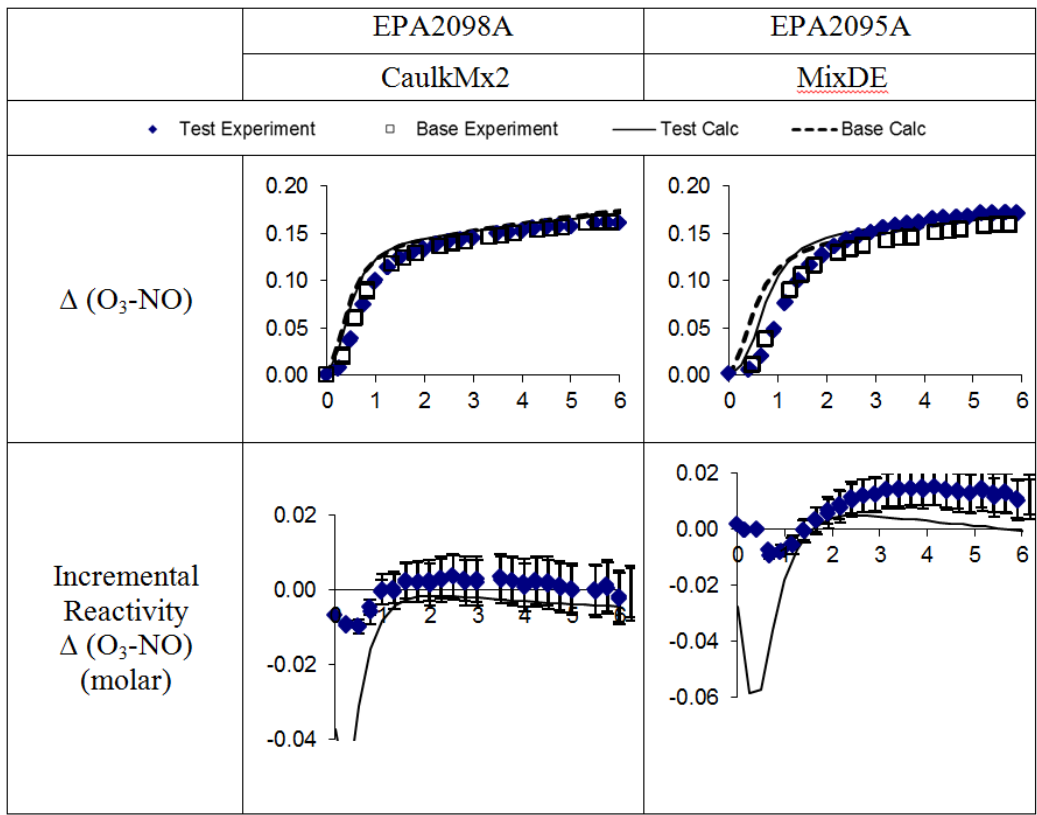


Figure 3. 20: SAPRC-2011 Ozone modeling results for n-Tridecane and n-Heptadecane.

Chapter 4: Secondary organic aerosol forming potential from heavy n-alkanes and hydrocarbon solvents under relevant urban atmospheric conditions

4.1: Introduction

A significant portion of ambient secondary organic aerosol (SOA) is underpredicted by models based on current inventory estimates (Presto et al., 2009; Cappa et al., 2016; Jathar et al., 2017; Ma et al., 2017). Many previous studies suggest that the missing SOA can be explained by the evaporation and subsequent oxidation of intermediate-volatility organic compounds (IVOCs) (Yee et al., 2012; Zhao et al., 2014), which have saturation concentrations ranging from 10^3 to 10^6 $\mu\text{g m}^{-3}$ and in ambient conditions are found almost entirely in the vapor phase (Donahue et al., 2012). Due to their lower volatility and heavier molar mass than traditional volatile organic compounds (VOCs), IVOCs are expected to be important SOA-forming contributors (Robinson et al., 2007; Chan et al., 2009). Moreover, emissions of VOCs into the troposphere additionally impact ozone formation, which at elevated concentrations is harmful to human health and the Earth ecosystems (Finlayson-Pitts and Pitts, Jr., 1993).

Alkanes and their mixtures represent a subset of IVOCs. A majority of ambient IVOC mass has been measured as an unresolved complex mixture (UCM) of branched and cyclic saturated alkanes (Tkacik et al., 2012; Chan et al., 2013). Moreover, heavy alkanes are present in varying fractions in diesel and motor oil, and are also abundant in diesel-powered vehicle emissions (Schauer et al., 1999; Lim and Ziemann, 2005; Brandenberger et al., 2005; Caravaggio et al., 2007; Houssni et al., 2017). Therefore, heavy alkanes and

their mixtures are good model systems for research on the SOA and ozone formation potential from an important class of IVOCs.

There have been several studies of the SOA formation from heavy alkanes using environmental smog chambers. High yields (>40%) were reported for the SOA formation from photo-oxidation reactions of C₁₂-C₁₇ *n*-alkanes, C₁₀-C₁₅ cyclic alkanes, and C₁₆ branched alkanes with OH radicals in the presence of high NO_x (Lim and Ziemann, 2005, Lim and Ziemann, 2009b, Presto et al. 2010, Loza et al. 2014). High SOA yields were also reported for photo-oxidation of C₁₂ cyclic alkanes under low NO_x conditions (Loza et al. 2014). However, Tkacik et al. (2012) did not observe high yields for high-NO_x photo-oxidation of C₁₂ straight chain, branched, and cyclic alkanes when studied at a lower organic aerosol concentrations (C_{OA}) that is more representative of typical atmospheric aerosol concentrations. SOA yields had been observed to increase with increasing carbon number for linear *n*-alkanes and cyclic alkanes (Presto et al. 2010, Lim and Ziemann, 2009a). For a given carbon number, yields follow the order cyclic > linear > branched (Lim and Ziemann, 2009b, Tkacik et al. 2012, Loza et al. 2014). The SOA yield of branched alkanes depends on the methyl branch position on the carbon backbone (Tkacik et al. 2012). Loza et al. (2014) reported that SOA yields are higher or the same under high-NO_x conditions in comparison to those measured for low-NO_x conditions.

Lim and Ziemann (2009b) further observed that SOA products formed from the reactions of linear, branched, and cyclic alkanes are similar. Yee et al. (2012) studied SOA

formation from the C₁₂ alkane under low-NO_x conditions. They found that RO₂· + HO₂· chemistry dominates the fate of the RO₂· radical. Zhang et al. (2014) and Fehner et al. (2015) addressed the importance of particle-phase chemistry in alkane SOA formation. Zhang et al. showed that NO_x greatly enhances the formation of δ-hydroxycarbonyl and its subsequent heterogeneous conversion to substituted dihydrofuran. Under conditions prevalent in urban and rural air, the ozone-dihydrofuran reactions dominates over the OH-dihydrofuran initiated oxidation. Highly oxygenated products are generated from dihydrofuran chemistry. Fehner et al. (2015) found particle-phase oligomer-producing reactions based on chemical composition data for each alkane system.

Lambe et al. (2012) examined the SOA generated from C₁₀, C₁₅, C₁₇ *n*-alkanes, tricyclo decane, and vapors of diesel fuel and Southern Louisiana crude oil in a flow reactor in the absence of NO_x and observed that decreasing SOA yield with increasing oxygen content of the secondary products and decreasing carbon content of the *n*-C₁₀, *n*-C₁₅, and tricyclo decane, consistent with transitions from functionalization to fragmentation. Zhang et al. (2013) also used a photochemical flow tube reactor to study the OH initiated heterogeneous oxidation pathways of cyclic alkanes (C₂₇H₄₈). Their analysis revealed that the first-generation functionalization products (cholestanones, cholestanals, and cholestanols) are the dominant reaction products.

Significant work has been carried out on the SOA formation from heavy alkanes, but these studies were all performed either at relatively high NO_x condition or in the absence

of NO_x . In this paper, a surrogate reactive organic gas (ROG) mixture designed to mimic urban atmospheric reactivity was applied in chamber studies of the photo-oxidation of several *n*-alkanes and alkane-containing hydrocarbon solvents. The SOA and ozone forming potential, bulk SOA chemical composition and physical properties, the influence of surrogate ROG mixture, and the effects of OH concentration on SOA production are investigated at urban relevant NO_x levels (<50ppb) using the advanced dual environmental chamber facility housed at the College of Engineering, Center for Environmental Research and Technology (CE-CERT) at University of California, Riverside (UCR). Table 4.1 lists all the experiments conducted for this section. To the best of the authors knowledge, this represents the first reported environmental chamber work on hydrocarbon solvents Isopar[®] M and Conosol[®] C-200.

4.2: Results and discussion

4.2.1: SOA formation

Figure 4.1 compares SOA formation from photo-oxidation of *n*-C₁₃ in the presence of H₂O₂ only, the surrogate + NO_x , and the surrogate + NO_x + H₂O₂. SOA formation from surrogate mixtures with and without enhanced hydroxyl radical (no added *n*-C₁₃) is shown for baseline comparison of SOA formation from the surrogate mixture. As mentioned in the previous section, the surrogate ROG mixture used in this work is designed to simulate urban-atmosphere gas-phase chemical reactivity. As expected, the surrogate-only experiments (no added *n*-C₁₃) have low SOA formation relative to those with the test IVOC. Experiments containing the *n*-C₁₃ and surrogate ROG mixture with

enhanced hydroxyl radical (H_2O_2 added) have the greatest SOA formation followed by $n\text{-C}_{13}$ with surrogate only (no H_2O_2), followed by the $n\text{-C}_{13}$ reaction with only enhanced hydroxyl radical (no surrogate). The SOA formation trend follows the consumption rate of $n\text{-C}_{13}$. The greater the $n\text{-C}_{13}$ consumed, the higher the SOA is formed (Figure 4.2 and Table 4.2). Moreover, the SOA formation rate follows the same trend, where the higher the reactivity of the photo-oxidation system, the faster the SOA formation rate occurs.

Lim and Ziemann (2009b) observed that yields increase with increasing carbon number for n -alkanes up to $n\text{-C}_{17}$ in the presence of NO_x . Figure 4.3 compares SOA mass concentration from photo-oxidation of $n\text{-C}_{13}$, $n\text{-C}_{14}$, $n\text{-C}_{15}$, and $n\text{-C}_{16}$ with enhanced hydroxyl radicals (H_2O_2) only. The previously observed trend of increasing SOA with increasing carbon number in the presence of NO_x also holds for OH only reaction for $n\text{-C}_{13}$ through $n\text{-C}_{16}$. The trend reflects two different phenomena at work; the higher the carbon number the greater the rate of reaction with OH (reflected in the slope of the curve) as well as the higher the carbon number the lower the vapor pressure of the test compound likely leading to lower volatility products (reflected in both slope and final aerosol volume).

Figure 4.4 plots the SOA formation from photo-oxidation of n -alkanes and hydrocarbon solvents in the presence of the surrogate ROG mixture and NO_x . Significant aerosol formation is observed for $n\text{-C}_{17}$ and Conosol[®] C-200 with $n\text{-C}_{17}$ greater than Conosol[®] C-200 even though less $n\text{-C}_{17}$ was added. $n\text{-C}_{17}$ also has the greatest SOA formation rate,

followed by Conosol[®] C-200, Isopar[®] M, and *n*-C₁₃. The aerosol formation from the surrogate mixture itself is seen to be minimal compared to the aerosol production from the *n*-alkanes and hydrocarbon solvents. The measured composition of the hydrocarbon solvents is shown in Figure 4.5; To estimate the average volatility of each hydrocarbon solvent, the primary retention axis was divided into bins centered on the retention time of each *n*-alkane; GC×GC-TOFMS chromatograms displaying the compound classifications are included in Figure 4.6. Because branched alkanes may elute significantly earlier than their straight-chain isomer (Rappoport and Gaumann, 1973), Figure 4.5 can be considered as an indication of the *n*-alkane equivalent volatility distribution for each solvent rather than a well-defined carbon number distribution. The observed distributions indicate that the volatility of Isopar[®] M and Conosol[®] C-200 were generally similar; for both solvents, the peak-area weighted volatility average is approximately equivalent to that of *n*-C₁₃. Therefore, the differences in observed SOA formation can be attributed to structural differences between the solvents rather than differences in SOA precursor volatility: Isopar M was dominated by isoalkanes (89%) whereas Conosol[®] C-200 was dominated by cycloalkanes (64%). Also, the carbon number overall looks to be dominated by lower carbon numbers in the range (Figure 4.5) so the fact that SOA formed from Conosol[®] C-200 in the presence of NO_x and surrogate is similar to *n*-C₁₇ means that the cyclic nature is offsetting SOA-forming capability on the order of 4 carbon numbers when considering SOA formation.

Effective SOA mass yields were calculated for Conosol[®] C-200 and Isopar[®] M using a similar approach to that of Odum et al. (1996, 1997a, 1997b) based on the GC×GC data.

The effective SOA mass yield (Y) is equal to the ratio of the particle wall-loss-corrected SOA mass (ΔM_0) to the estimated mass of hydrocarbon solvents reacted (ΔHC) (Eq.1). The percentages of hydrocarbon solvents components reacted are calculated by assuming that these components go through a first order reaction with hydroxyl radical, which is shown in equation 3. Reordering equation 2 generates equation 3.

$$Y = \frac{\Delta M_0}{\Delta HC} \quad (1)$$

$$\frac{d[C_i]}{dt} = -k_{OH,C_i}[OH][C_i] \quad (2)$$

$$\ln\left(\frac{C_0}{C}\right) = k_{OH,C_i}[OH] * t_r \quad (3)$$

where $[C_i]$ is the concentration of individual hydrocarbons in $\mu\text{g m}^{-3}$, k_{OH} is the reaction rate constant in $\text{cm}^3 (\text{molecules}\cdot\text{s})^{-1}$ of that compound, $[OH]$ is the hydroxyl radical concentration in molecules cm^{-3} , which is estimated from the measured decay of toluene or *m*-xylene (Eq.1) (Hildebrandt et al. 2009). t_r is the reaction time. Based on the hydrocarbon solvent composition (Figure 4.5) and the estimated k_{OH} of each compound class (Table 4.3), we estimate both hydrocarbon solvents completely reacted under the experimental conditions. The calculated yield is shown in Table 4.1. Conosol[®] C-200 has higher yields than those of Isopar[®] M, which is due to the presence of more cyclic alkanes in Conosol[®] C-200 (Figure 4.5). Moreover, the yields of Conosol[®] C-200 and Isopar[®] M are greatly enhanced by the addition of H_2O_2 .

These experiments were then repeated with enhanced OH concentration (Figure 6). As seen for *n*-C₁₃ (Figure 4.7), the enhanced H_2O_2 increased the amount of aerosol formed,

likely due to a combination of increased kinetics, increased radical oxidant concentrations, and the added increase in aerosol due to the fact that more aerosol was available to condense upon due to the first two reasons. Conosol[®] C-200 forms tremendous amount of SOA. Different from non-H₂O₂ runs, both Conosol[®] C-200 and Isopar[®] M form more SOA than *n*-C₁₇, which indicates that OH mechanism dominates SOA formation.

4.2.2: SOA elemental analysis and physical properties

Van Krevelen diagrams (H:C vs. O:C) are one common approach for characterizing photochemical evolution and can provide an indication of the change in chemical functionality following oxidation. For instance, oxidizing an aliphatic carbon (–CH₂–) to a carbonyl group (–C(=O)–) leads to a loss of 2 hydrogen atoms and a gain of 1 oxygen atom, and therefore generates a slope of –2 in Van Krevelen space (Heald et al., 2010). The Van Krevelen diagram for the photo-oxidation of *n*-C₁₇ in the presence of NO_x and surrogate ROG mixture with and without additional H₂O₂ can be found in Figure 4.8 (corresponding data is summarized in Table 4.1 along with other physical properties of SOA, including density and volume fraction remaining (VFR) for all the experiments.) *n*-C₁₇-derived SOA data line up in the Van Krevelen diagram along a line with a slope of -0.5 and -1 in the absence and presence of H₂O₂, respectively. A slope of -1 could indicate addition of a carboxylic acid group or both carbonyl and alcohol moieties to form a hydroxycarbonyl. A slope of -0.5 can be generated by the addition of both acid and alcohol/peroxide functional groups without fragmentation or the addition of acid

groups with fragmentation (Ng et al., 2011). The SOA formed from *n*-C₁₇ in the presence of the surrogate ROG mixture and H₂O₂ under urban-relevant NO_x levels was the most oxidized, as indicated by the high O:C ratio observed compared with those formed from *n*-C₁₃ and hydrocarbon solvents (Table 4.1). However the VFR is only 0.25 at the end of the experiment (Table 4.1). If the VFR is low, fragmenting happens. It is unclear how *n*-C₁₇ obtains 10 oxygen atoms in such a short time. Possible reasons could be occurrence of auto-oxidation reactions for heavy alkanes, which happen really fast. This puzzle is raised by Presto et al. (2009) before and they also find highly oxygenated SOA from photo-oxidation of *n*-C₁₇ under high NO_x conditions in the presence of seed particles.

Tkacik et al. (2012) found that the mass spectrum of SOA produced from photo-oxidation of alkanes with varying structures is similar to the semi-volatile-oxygenated and hydrocarbon-like organic aerosol (SV-OOA and HOA) factors derived from ambient data. A method established previously by Ng et al. (2010) is applied in Figure 4.9, which plots the mass fraction of the AMS organic signal at $m/z = 44$ (f_{44}) against that at $m/z = 43$ (f_{43}) for the same *n*-C₁₇ SOAs displayed in Figure 4.8. The m/z 44 ion signal is dominated by CO₂⁺, which is generated predominantly from acids or acid-derived species. The m/z 43 ion is dominated by both C₃H₇⁺ and C₂H₃O⁺ ions, where C₃H₇⁺ is a hydrocarbon fragment and C₂H₃O⁺ results mostly from non-acid oxygenated species. The triangle space defined by two dotted lines illustrates the region where ambient OOA components concentrate. Atmospheric aging leads to an increase of f_{44} and a decrease of f_{43} toward the apex of the triangle area (Ng et al., 2011). *n*-C₁₇ (no H₂O₂ added) SOAs

occupy the lower portion of the plot, which is more similar to the less oxidized ambient SV-OOA whereas $n\text{-C}_{17}$ (H_2O_2 added) SOAs became more similar to the LV-OOA. Van Krevelen diagrams and triangle plots of other n -alkanes and hydrocarbon solvents are available in Figure 4.10-4.13.

SOA volatility determines the SOA production and gas-particle partitioning. It could be influenced by functionalization, fragmentation, oligomerization, oxidation, and SOA mass (Tritscher, T., et al 2011). Volume fraction remaining (VFR) is used to describe bulk SOA volatility after heating SOA at a fixed temperature ($17\text{ }^\circ\text{C}$) in a thermodenuder for a short period of time (17s). Figure 4.14 plots the VFR as a function of irradiation time for n -Alkane and Alkane mixtures SOAs in the presence of NO_x and surrogate ROG mixture with or without H_2O_2 . The VFR from surrogate ROG mixture SOA is shown as comparison. VFRs for SOA formed from C_{13} , C_{17} , and Conosol[®] C-200 increase continuously as the experiment progresses, which indicates the formation of low volatility and more oxidized compounds due to functionalization, fragmentation, and oligomerization. The VFR of Isopar[®] M SOA increases during the first three hours of the experiments and then reaches a plateau. From Figure 4.14, we could also conclude that adding H_2O_2 does not change the SOA composition dramatically.

4.2.3: Ozone formation

Figure 4.15 presents the results of ozone formation from photo-oxidation of n -alkanes and hydrocarbon solvents in the presence of the surrogate ROG mixture and NO_x , which

illustrates that ozone formation is suppressed and ozone formation rates are slower compared with that of the surrogate run. Conosol[®] C-200 suppresses ozone more than Isopar[®] M. Conosol[®] C-200 contains predominantly cycloalkanes (64% by GC×GC peak area) and isoalkanes (35%) whereas Isopar[®] M contains mainly iso-alkanes (89%). Cycloalkanes suppress ozone less than isoalkanes based on their maximum incremental reactivity (MIR) values (A measure of the increase in ozone formation per unit weight of a hydrocarbon when added to the atmosphere) (Table 4.4).

The possible explanation is that heavier alkanes inhibit the cycling of radicals back to hydroxyl radicals by sequestering peroxy radicals as organic nitrates (RONO₂) from RO₂· + NO reactions rather than cycling to RO·. Consequently, the presence of heavy alkanes reduces the overall hydroxyl radical concentration available to oxidize both the *n*-alkanes or hydrocarbon solvents and the ozone forming surrogate ROG mixture relative to the amount of oxidation and ozone that forms in the surrogate photo-oxidation alone (Carter, 2011). In addition, the increased nitrate formation increases the rates of reactive NO_x removal from the system, which limits the maximum amount of O₃ formed under a NO_x-limited scenario. Conosol[®] C-200 suppresses ozone more than Isopar[®] M. Conosol[®] C-200 contains only cycloparaffin and isoparaffin while Isopar[®] M contains mainly iso-alkanes. Cycloalkanes suppress ozone less than isoalkanes based on their maximum incremental reactivity (MIR) values (A measure of the increase in ozone formation per unit weight of a hydrocarbon when added to the atmosphere) (Table 4.4).

In the experiments with added H₂O₂, the impact of hydroxyl radical loss was reduced and yet the ozone suppression trend was still observed (Figure 4.16). This could be due in part to the role of nitrate formation in enhancing NO_x removal rates in these relatively low NO_x experiments. Figure 4.16 also shows that similar amount of ozone is formed from photo-oxidation of *n*-C₁₇, Conosol[®] C-200, and Isopar[®] M, which may be due to the presence of similar amount of NO_x. More NO_x was added to the *n*-C₁₃ run and therefore more ozone formed.

Figure 4.17 compares the ozone formation from photo-oxidation of *n*-C₁₃ in the presence of surrogate and NO_x with and without H₂O₂. Similar amounts of ozone are formed for *n*-C₁₃ in the presence of surrogate and NO_x with and without H₂O₂. The addition of H₂O₂ increases the overall ozone formation rate as measured by the slope of the rapid rise of ozone in the early segment of the reaction.

4.3: Conclusion

Conosol[®] C-200, Isopar[®] M, *n*-C₁₇, and *n*-C₁₃ form significant amounts of SOA under urban relevant NO_x levels in the presence of a surrogate ROG mixture and H₂O₂. Compared with H₂O₂ only and surrogate only experiments, SOA formation is the highest for the experiment where the surrogate ROG mixture providing a baseline reactivity in the system with enhanced hydroxyl radical (H₂O₂ added). SOA formation is enhanced for larger *n*-alkanes in the presence of H₂O₂, which is caused by decreased volatility. Ozone formation is suppressed in general because of the formation of organic nitrates from

heavy alkanes. It is still unclear about how highly oxygenated SOA is formed from the photo-oxidation of $n\text{-C}_{17}$ in the presence of the surrogate ROG mixture and H_2O_2 at urban relevant NO_x levels. This study provides implications for the understanding of SOA formation from photo-oxidation of IVOCs and IVOC mixtures in the Earth's atmosphere. Photo-oxidation of IVOCs is potential source of oxygenated OA at urban relevant NO_x concentration. The conclusions drawn for n -alkanes and hydrocarbon solvents could be extrapolated to similar individual IVOCs or IVOC mixtures.

Tables & Figures

Table 4. 1: List of experiments.

Compound	HC ₀ ^a	NO ^b	NO ₂ ^b	NO _x ^b	Surr ^c	H ₂ O ₂ ^b	Tim	OH	SOA	O:C ^g	H:C ^g	VFR
	ppb	ppb	ppb	ppb	ppmC	ppm	min	Molec (cm ³ hr) ⁻¹	μg			
<i>n</i> -C ₁₃	40.0	20.1	9.9	30.0	1	-	570	8.7	19.0	-	-	0.4
<i>n</i> -C ₁₃	40.0	17.8	12.7	30.5	1	1	493	13.4	81.9	0.3	1.9	-
<i>n</i> -C ₁₃	40.0	*	*	*	*	1	280	9.3	3.5	-	-	-
<i>n</i> -C ₁₄	40.0	*	*	*	*	1	339	-	40.6	-	-	-
<i>n</i> -C ₁₅		*	*	*	*	1		-		-	-	-
<i>n</i> -C ₁₆	40.5	*	*	*	*	1	346	-	82.3	-	-	-
<i>n</i> -C ₁₇	40.0	23.0	10.8	33.8	1	-	480	13.0	104.	-	-	-
<i>n</i> -C ₁₇	40.0	15.8	8.1	23.9	1	1	426	17.3	108.	0.7	1.7	0.3
Conosol [®] C-	156.4 ^h	16.7	8.9	25.6	1	-	325	-	72.4	0.3	1.8	0.2
Conosol [®] C-	156.4 ^h	13.5	11.4	24.9	1	1	329	8.7	220.	0.3	1.8	0.2
Isopar [®] M	158.9 ^h	13.2	8.3	21.5	1	1	351	3.9	126.	0.3	1.9	0.1
Isopar [®] M	158.9 ^h	14.3	7.9	22.2	1	-	366	-	27.5	0.3	1.9	0.2
S1 ⁱ	-	20.2	9.5	29.7	1	-	420	13.0	0.7	-	-	0.4
S2 ^j	-	15.7	10.3	26	1	1	325	-	2.0	-	-	-

a. Target concentrations provided. Typically, actual concentrations in these chamber systems are within 5% of target concentration; b. Initial NO, NO₂, NO_x, and H₂O₂ concentration before turning on black lights; c. Surrogate ROG mixture; d. Irradiation Time; e. Calculated from toluene or *m*-xylene decay; f. Averaged density over the entire course of the experiment; g. Averaged data over the final one hour of the experiment; h. Molecular weights are obtained from manufacturer. i. Surrogate-NO_x-H₂O₂ only runs; j. Assumed 1.5 g cm⁻³ is chosen for surrogate only experiment based on previous experimental data; “*”: Chemicals not injected; “-”: Data not collected; O:C: Oxygen-to-carbon ratio; H:C: Hydrogen-to-carbon ratio; VFR: Volume fraction remaining;

Table 4. 2: SOA yields for experiments listed in Figure 4.1.

Experimental Conditions	% C ₁₃ Reacted	ΔM (μg/m ³)	Yield*
<i>n</i> -C ₁₃ + Surrogate + NO _x + H ₂ O ₂ + UV	0.66	81.9	0.41
<i>n</i> -C ₁₃ + Surrogate + NO _x + UV	0.49	19.0	0.13
<i>n</i> -C ₁₃ + H ₂ O ₂ + UV	0.34	3.5	0.03

*: Yield is calculated based on assumption that 100% *n*-C₁₃ injected into the chamber.

Table 4. 3: The $k_{OH\cdot S}$ of Conosol[®] C-200 and Isopar[®] M components.

	n-alkane	Isoalkane	Cycloalkane	% reacted
<C ₁₁	1.04E-11	>1.04E-11	>1.04E-11	100
Undecane	1.23E-11	>1.23E-11	>1.23E-11	100
C ₁₁ -C ₁₂	1.27E-11	>1.27E-11	>1.27E-11	100
Dodecane	1.32E-11	>1.32E-11	>1.32E-11	100
C ₁₂ -C ₁₃	1.41E-11	>1.41E-11	>1.41E-11	100
Tridecane	1.51E-11	>1.51E-11	>1.51E-11	100
C ₁₃ -C ₁₄	1.65E-11	>1.65E-11	>1.65E-11	100
Tetradecane	1.79E-11	>1.79E-11	>1.79E-11	100
C ₁₄ -C ₁₅	1.93E-11	>1.93E-11	>1.93E-11	100
Pentadecane	2.07E-11	>2.07E-11	>2.07E-11	100
>C ₁₅	>2.07E-11	>2.07E-11	>2.07E-11	100

Table 4. 4: Maximum incremental reactivity (MIR) values for alkanes studied.

Compound	MIR
	n-alkane 0.61
C11	cycloalkane 0.9
	isoalkane 0.73
	n-alkane 0.55
C12	cycloalkane 0.8
	isoalkane 0.63
	n-alkane 0.53
C13	cycloalkane 0.7
	isoalkane 0.6
	n-alkane 0.51
C14	cycloalkane 0.65
	isoalkane 0.55
	n-alkane 0.5
C15	cycloalkane 0.61
	isoalkane 0.5
	n-alkane 0.45
C16	cycloalkane 0.55
	isoalkane 0.47

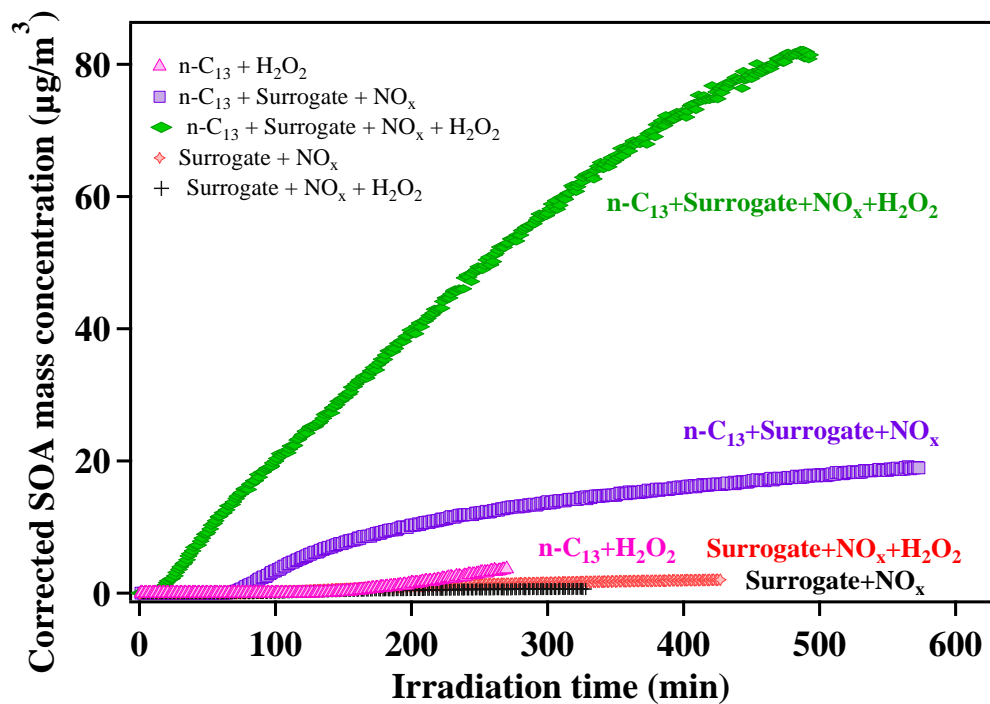


Figure 4. 1: Comparison of SOA formation of n-C₁₃ from three different photo-oxidation systems.

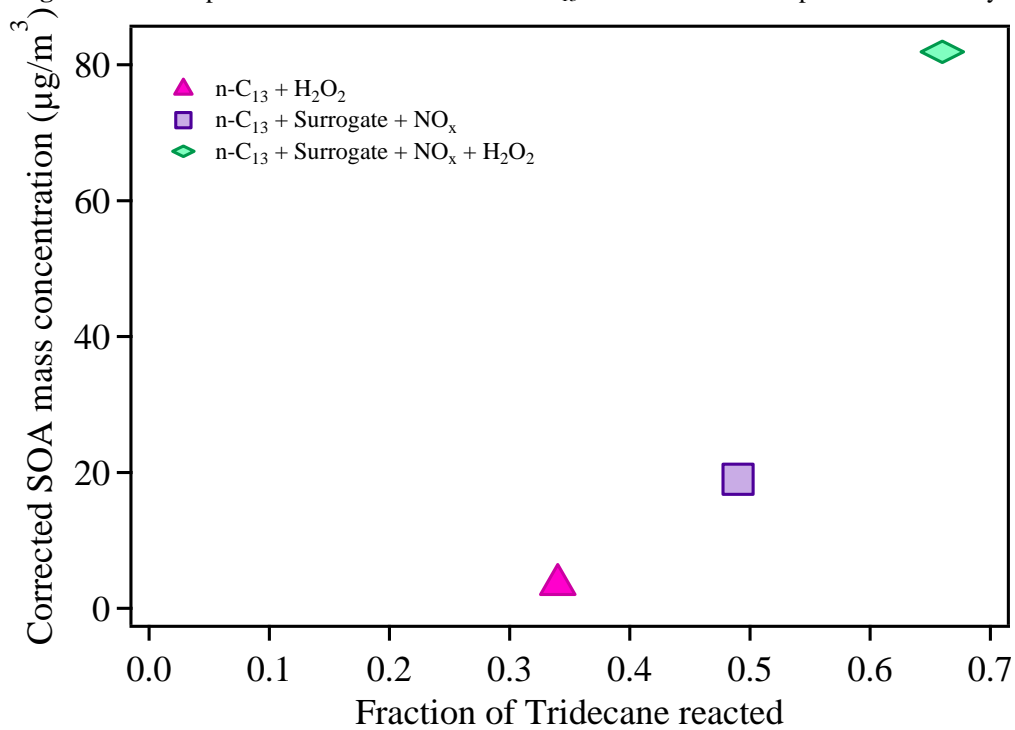


Figure 4. 2: Percentage of n-Tridecane reacted VS SOA formation of n-C₁₃ from three different photo-oxidation systems.

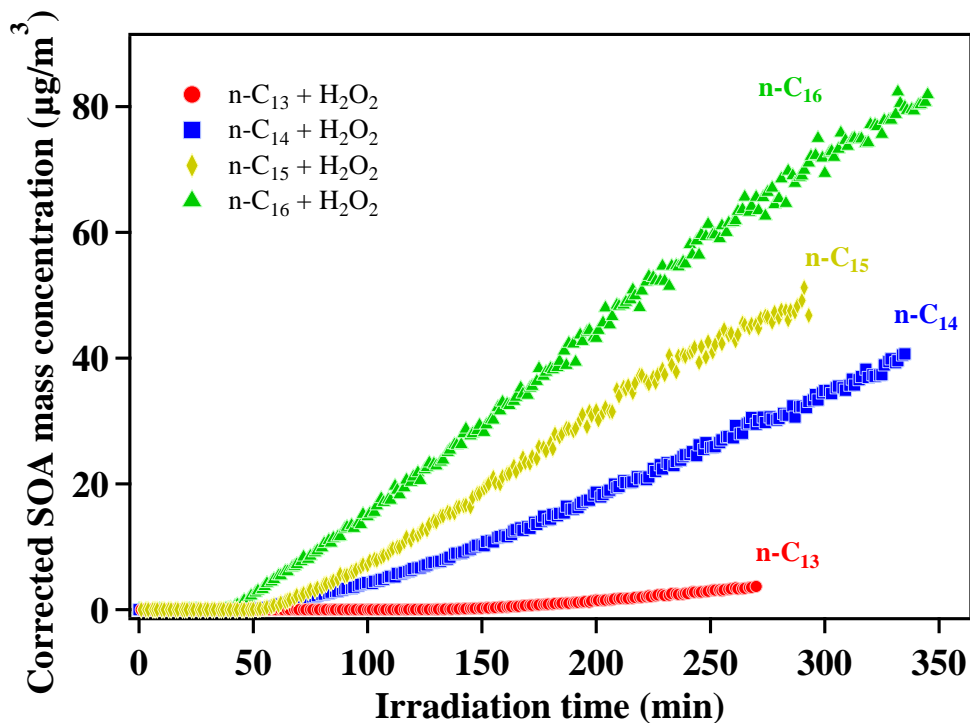


Figure 4. 3: Comparison of SOA formation from photo-oxidation of four n-alkanes.

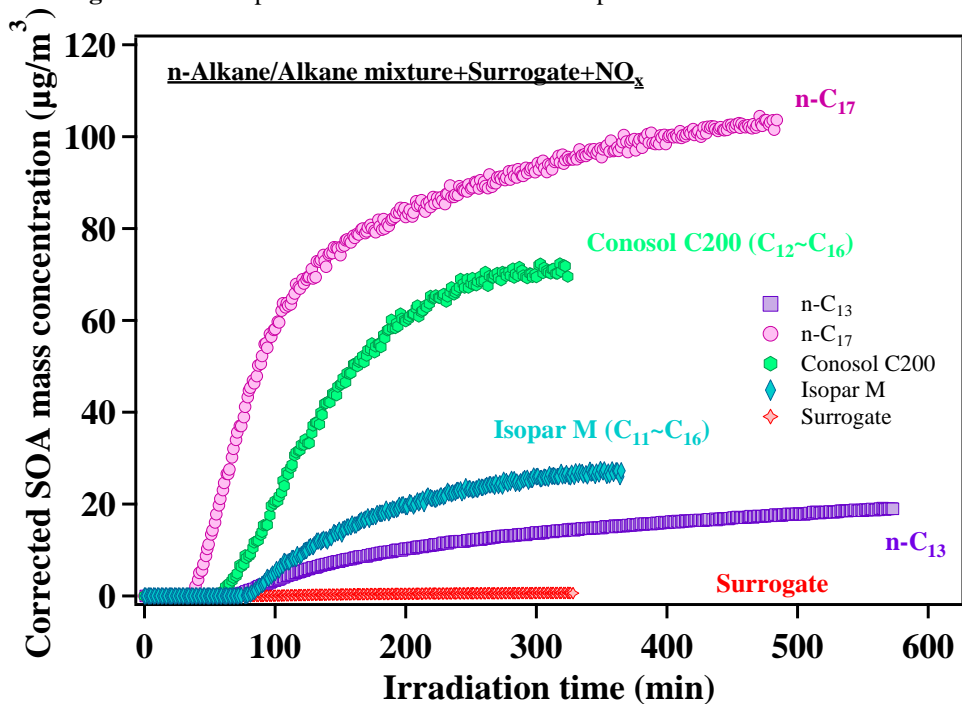


Figure 4. 4: SOA formation from photo-oxidation of *n*-alkanes and hydrocarbon solvents with surrogate and NO_x.

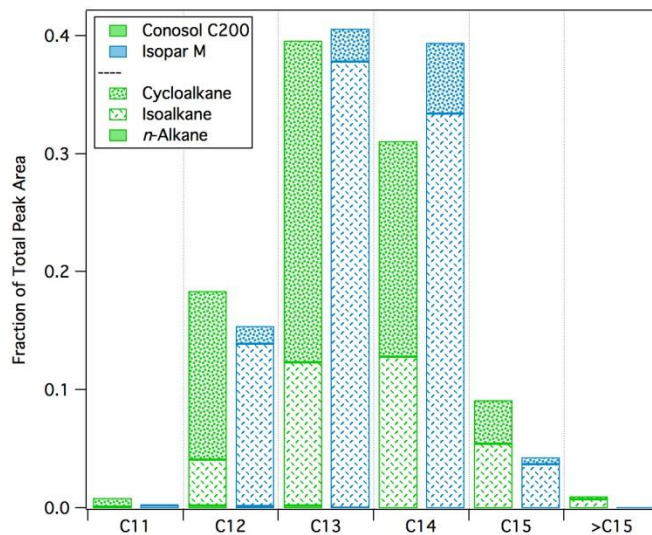


Figure 4. 5: Comparison of compound classes observed in Conosol C200 and Isopar M by GC×GC-TOFMS.

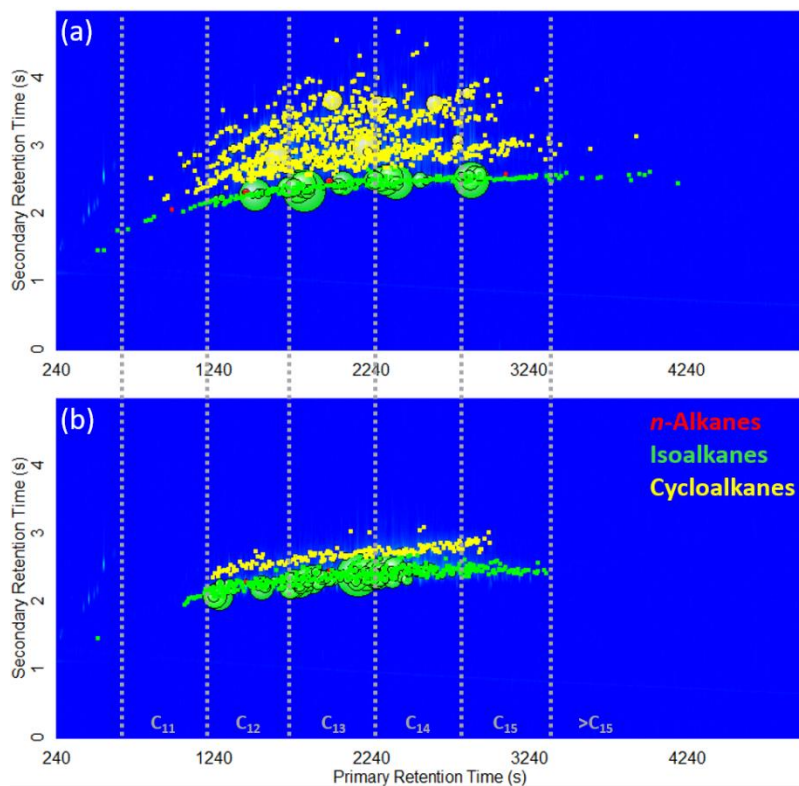


Figure 4. 6: GC×GC-TOFMS chromatograms for (a) Conosol[®] C200 and (b) Isopar[®] M. *n*-Alkanes, branched alkanes, and cycloalkanes are indicated by the classification bubbles, for which the size is proportional to the measured peak area.

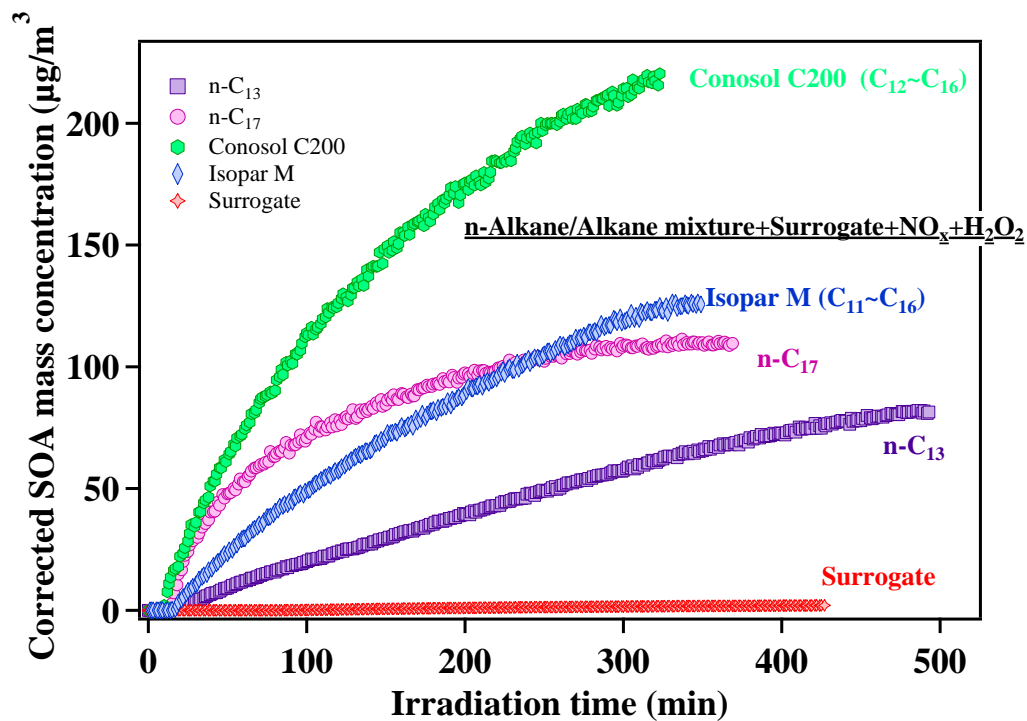


Figure 4. 7: SOA formation from photo-oxidation of *n*-alkanes and hydrocarbon solvents with surrogate, H₂O₂, and NO_x.

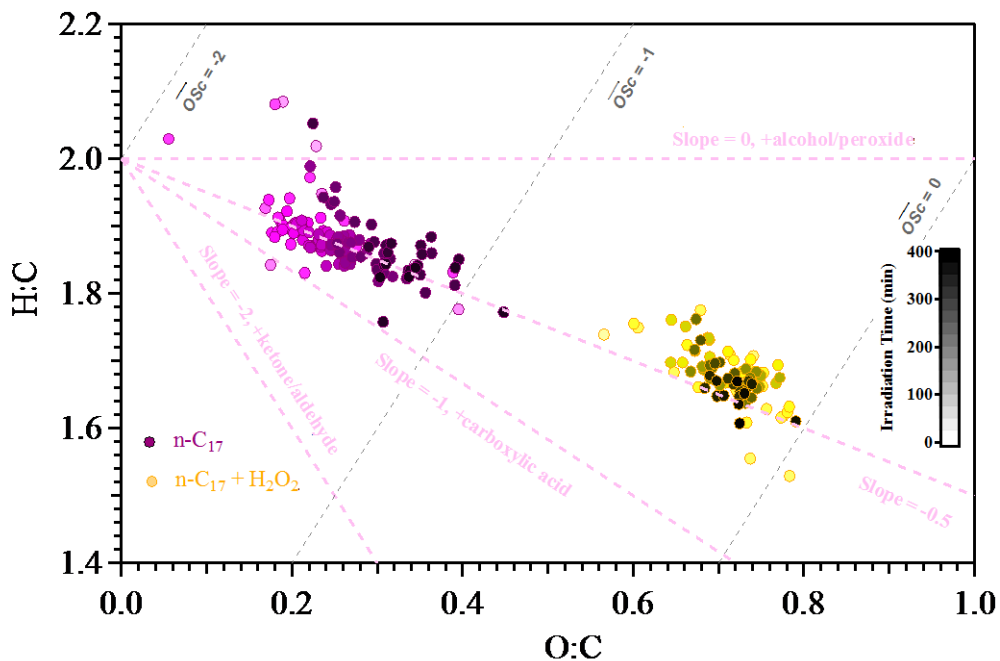


Figure 4. 8: Van Krevelen diagram of *n*-C₁₇ with the presence of surrogate and NO_x. H₂O₂ is added to one of the experiments to enhance OH radical concentration.

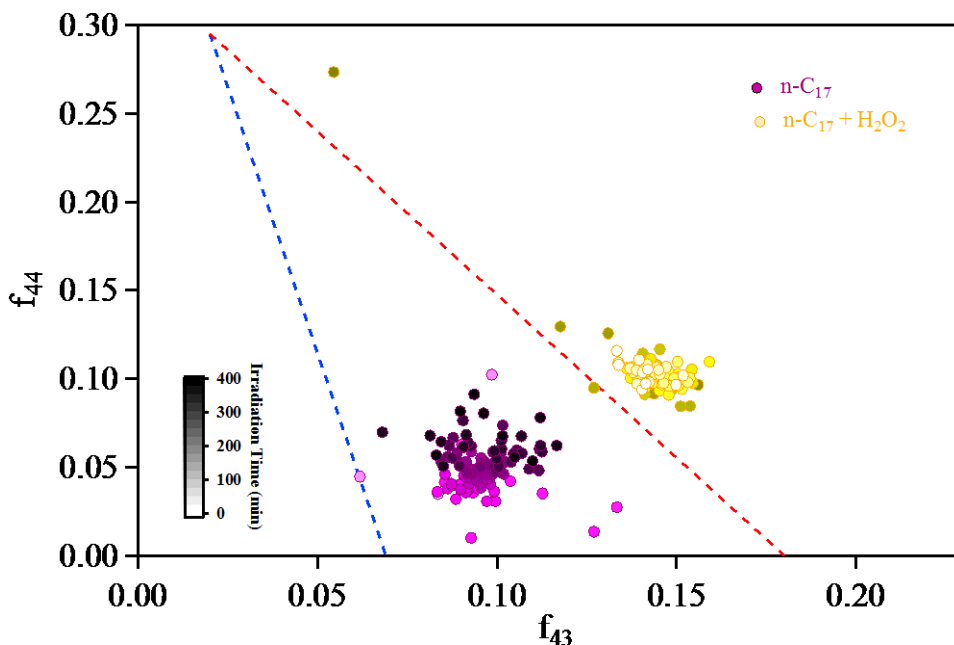


Figure 4. 9: f_{44} vs. f_{43} for the SOA generated from photo-oxidation of n -C₁₇ with the presence of surrogate, NO_x and H₂O₂. The dotted lines define the triangular space where ambient OOA components fall, following Ng et al. (2010)

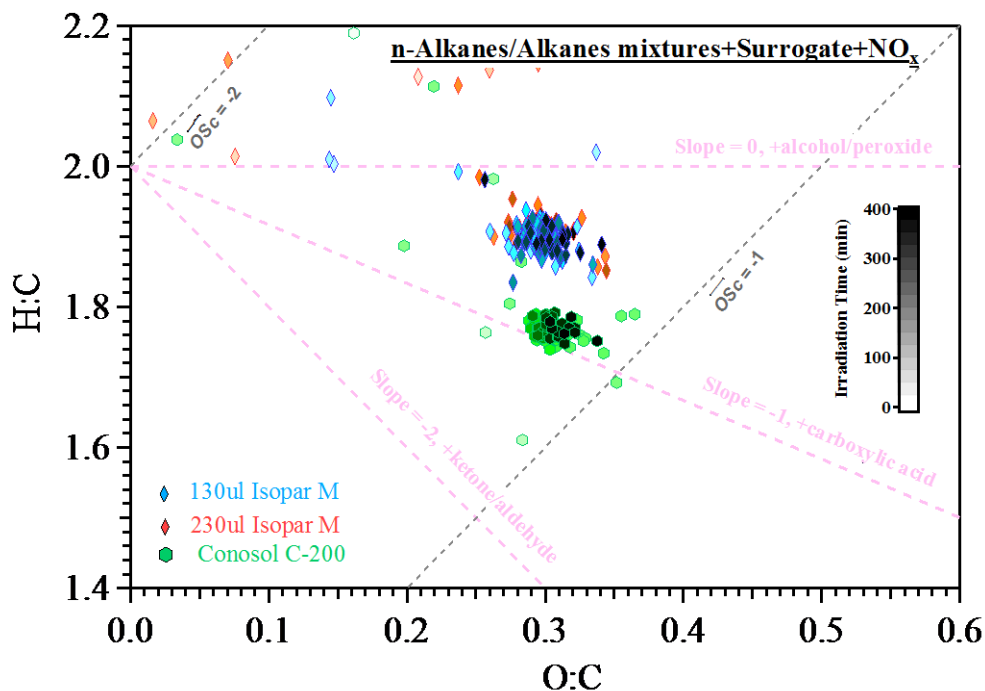


Figure 4. 10: Van Krevelen Diagram of select n -alkanes and hydrocarbon solvents with the presence of surrogate and NO_x.

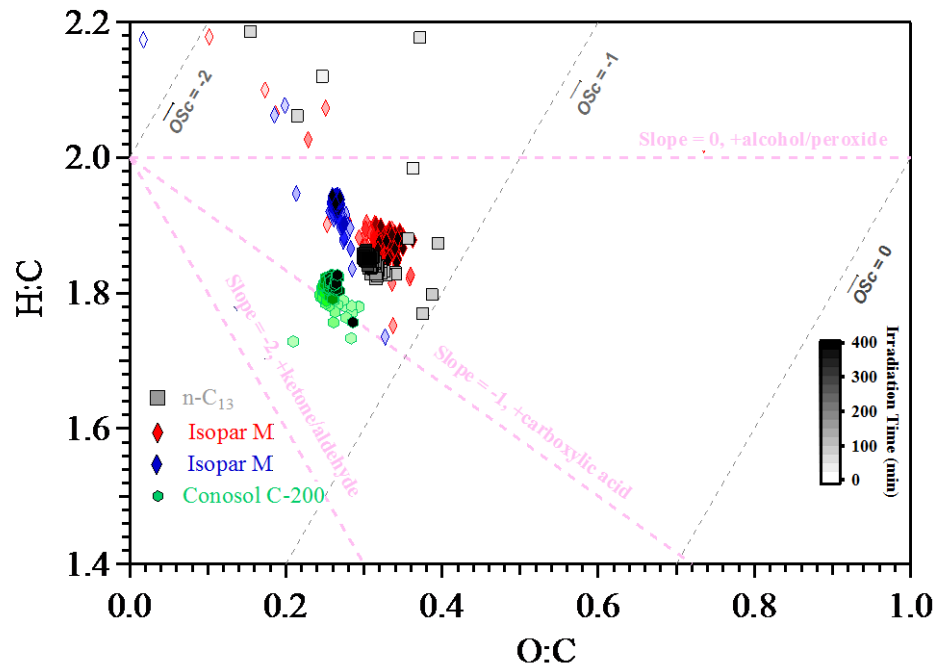


Figure 4. 11: Van Krevelen Diagram of select n-alkanes and hydrocarbon solvents with the presence of surrogate, NO_x and H₂O₂.

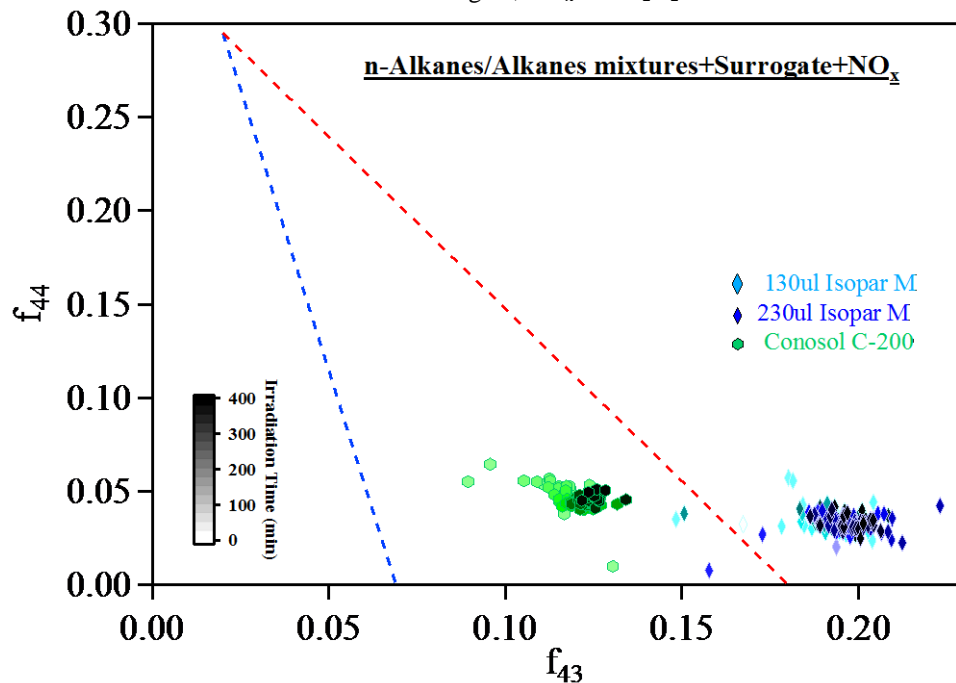


Figure 4. 12: f_{44} vs. f_{43} for the SOA generated from photo-oxidation of hydrocarbon solvents with the presence of surrogate and NO_x. The dotted lines define the triangular space where ambient OOA components fall. The slope and intercept of the line on the left hand side are -6.0204 and 0.4154; the slope and intercept of the line on the right hand side are -1.8438 and 0.3319.

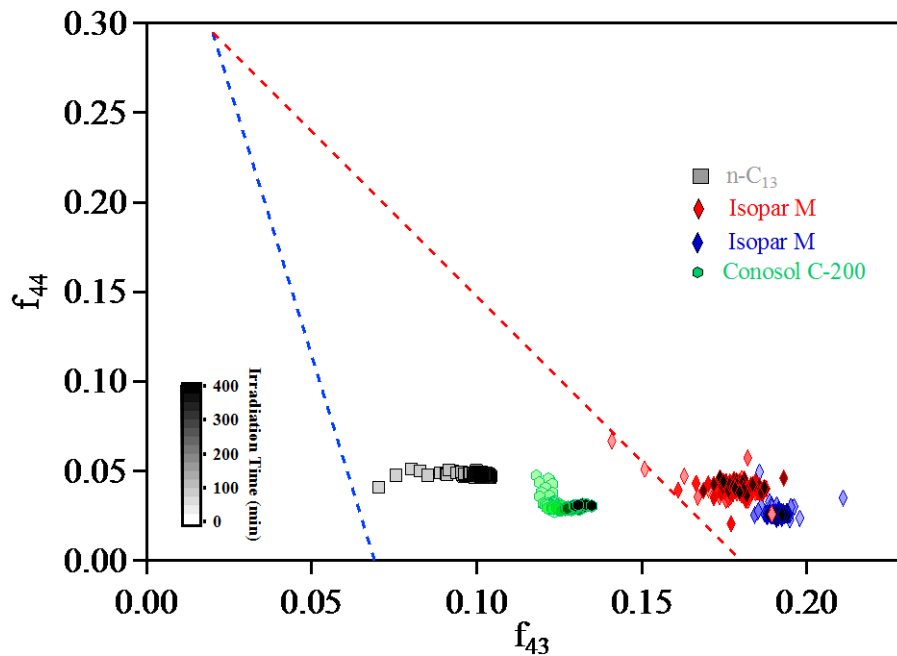


Figure 4. 13: f_{44} vs. f_{43} for the SOA generated from photo-oxidation of n-C₁₃ and hydrocarbon solvents with the presence of surrogate, NO_x and H₂O₂. The dotted lines define the triangular space where ambient OOA components fall. The slope and intercept of the line on the left hand side are -6.0204 and 0.4154; the slope and intercept of the line on the right hand side are -1.8438 and 0.3319.

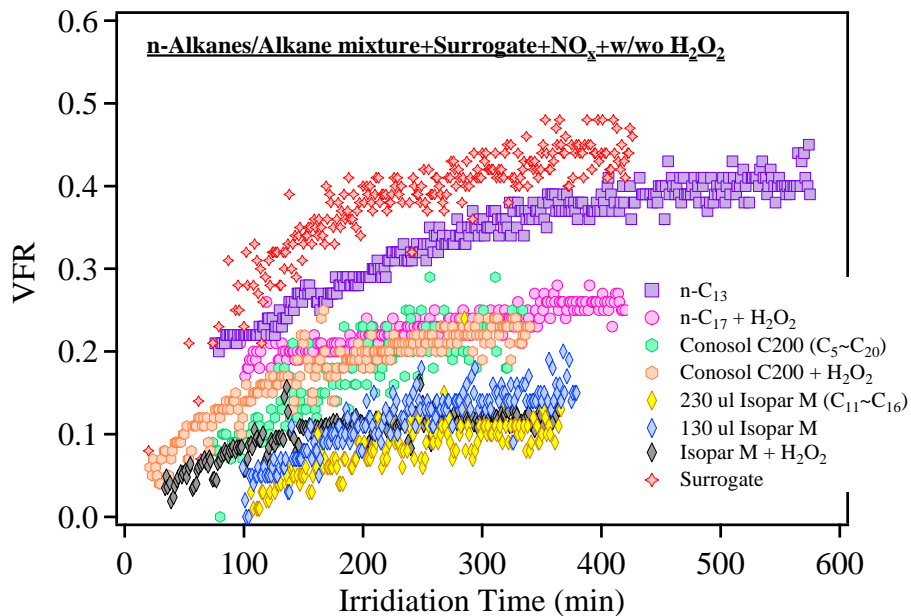


Figure 4. 14: VFR of n-alkanes and hydrocarbon solvents with the presence of surrogate and NO_x (H₂O₂ as needed).

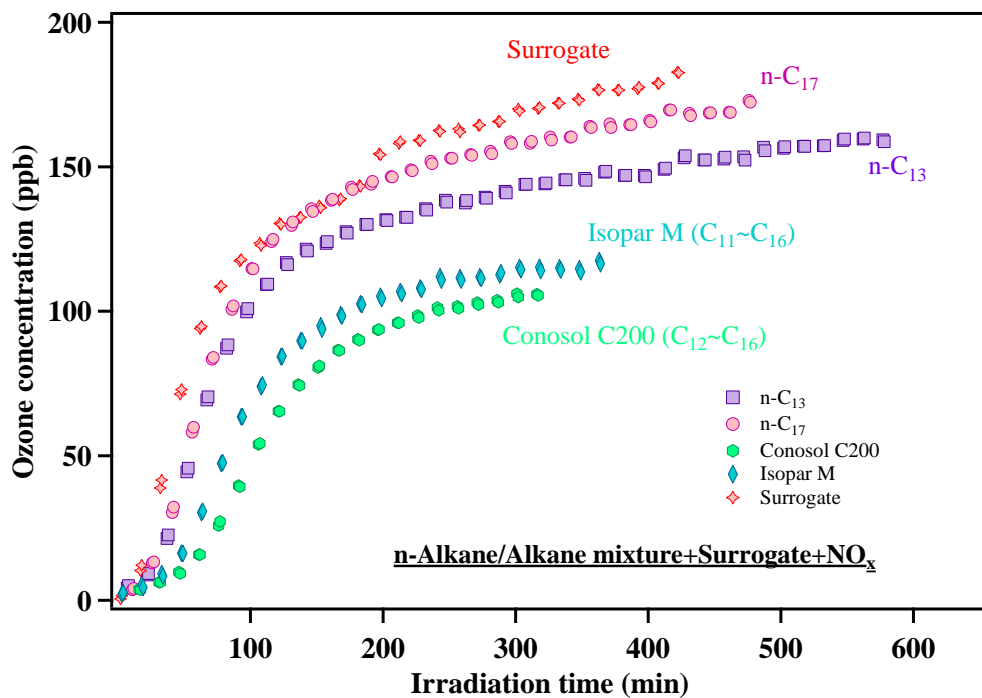


Figure 4. 15: Ozone formation from photo-oxidation of *n*-alkanes and hydrocarbon solvents with surrogate and NO_x .

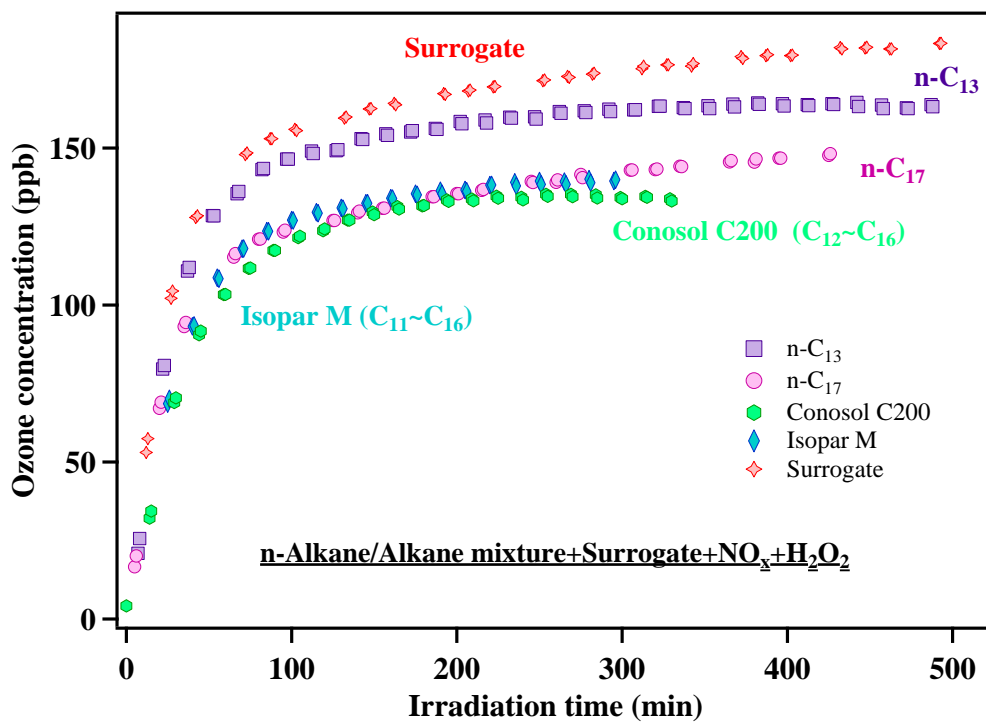


Figure 4. 16: Ozone formation from photo-oxidation of *n*-alkanes and hydrocarbon solvents with surrogate, H_2O_2 , and NO_x .

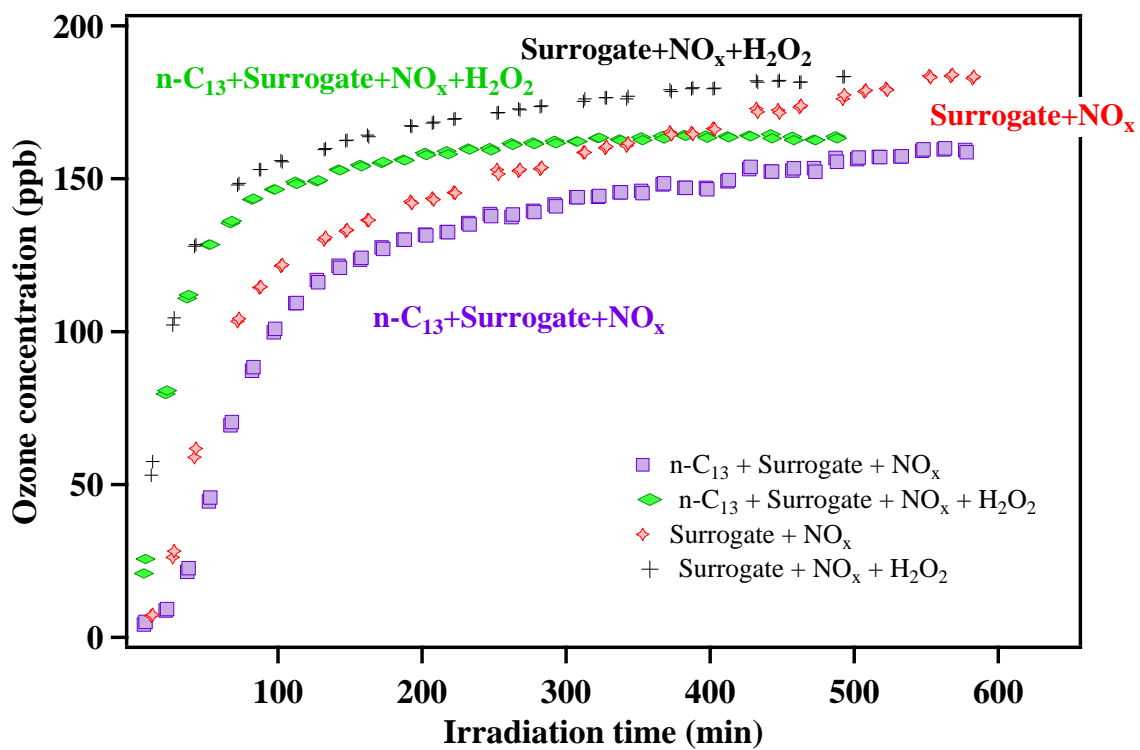


Figure 4. 17: Comparison of ozone formation from photo-oxidation of *n*-C₁₃ in the presence of surrogate and NO_x with or without H₂O₂.

Chapter 5: Secondary Organic Aerosol and Ozone Formation from Photo-Oxidation of Unburned Diesel Fuel in a Surrogate Atmospheric Environment

5.1: Introduction

Oxidation products of volatile and intermediate-volatility organic carbon (VOC and IVOC, respectively) vapors may partition themselves into aerosol phase to form secondary organic aerosol (SOA) (Pankow et al., 1994; Odum et al., 1996; Ng et al., 2007; Tkacik et al., 2012; Zhao et al., 2014). SOA constitutes a significant portion of ambient fine particulate matter affecting global climate change, visibility, and human health (Naeher et al. 2007; Hallquist et al., 2009; Yee et al., 2013; Qin et al., 2013). Nevertheless, uncertainties remain between model estimation and measured data, organic vapor sources, and SOA aging schemes (Jathar et al., 2016). Furthermore, oxidation of VOCs and IVOCs may lead to increased ground-level ozone concentration impacts human health and plant ecosystems (Finlayson-Pitts et al., 1993).

Organic vapors in diesel exhaust have received attention in previous studies including SOA formation from their photo-oxidation (e.g., Weitkamp et al., 2007, Nakao et al., 2011, Bahreini et al., 2012, Gentner et al. 2012, Gentner et al., 2017). However, studies focused on the SOA forming potential of unburnt diesel fuel are scarce. Miracolo et al. (2010) previously reported that unburned diesel fuel was a major component of exhaust from diesel engines. Additionally, diesel fuel is a complex mixture of IVOCs (carbon numbers ranging from C₈ to C₂₅ and a peak around C₁₄ (Liang et al. 2005; Brandenberger et al., 2005), which have recently been considered as important ambient SOA forming

precursors (Jathar et al., 2013). Therefore, further measurement of the SOA and ozone forming potential from photo-oxidation of diesel fuel is of tremendous interest.

SOA formation from diesel components such as heavy alkanes has been individually studied previously under controlled conditions. SOA production has been observed for photo-oxidation of C₁₂-C₁₇ n-alkanes, C₁₀-C₁₅ cyclic alkanes, and C₁₆ branched alkanes with OH radicals in the presence of high NO_x in an environmental smog chamber. (e.g., Lim and Ziemann, 2005, Lim and Ziemann, 2009, Presto et al. 2010, Loza et al. 2014) Lim and Ziemann (2009) propose that SOA yields from alkanes depend on both volatility and molecular structure. While Presto et al. (2009) showed that the photo-oxidation of large n-alkanes can create highly oxygenated organic aerosol. However, very little literature is available about SOA and ozone formation from complex mixtures of these species. Miracolo et al. (2010) observed that photo-oxidation of diesel fuel rapidly produced substantial SOA; nevertheless, the SOA formed from diesel fuel was observed to be less oxidized than either oxygenated organic aerosol (OOA) or SOA formed from the photo-oxidation of dilute diesel exhaust (Miracolo et al. 2010). Jathar et al. (2013) reported that SOA formation from photo-oxidation of diesel fuels was not sensitive to aromatic content, highlighting the important contribution of large alkanes to SOA formation. They reported a yield of 0.02-0.3 for photo-oxidation of unburnt diesel fuel.

Previous environmental chamber experiments on evaporated diesel were carried out at relatively high NO_x concentrations. (Odum et al., 1997a; Odum et al., 1997b; Jathar et al.,

2013) In this work, SOA and ozone formation is explored from photo-oxidation of a series of in-use #2 diesel fuels at under low NO_x concentrations in the presence of a surrogate mixture designed to mimic urban atmospheric reactivity. The work is designed to provide insights on SOA and ozone formation under well controlled conditions to improve regional pollution control policies and fuel regulations. Experimental conditions and results for all the smog chamber runs are listed in Table 5.1.

5.2: Results and discussion

5.2.1: Atmospheric availability of #2 diesel

Evaporation mass loss rates of eight different #2 diesel fuel samples were evaluated gravimetrically at 25°C from evaporation chambers operating as CSTRs. Only ~20% of the diesel fuel was determined to evaporate over a period of 10-months (Figure 5.1 and Table 5.2). Evaporation rates were consistent (st.dev. of percentage weight loss ~ 1.2%) between samples.

Previous studies have shown a robust correlation of evaporation rate with vapor pressure (e.g., Wesenbeeck et al., 2008; Guth et al., 2004). Later, a new one-parameter correlation was developed for the evaporation rate of chemicals as a function of both vapor pressure and molar mass (Eqs.1). The limitation of the correlation is that it applies only to liquid surfaces that are unaffected by the underlying solid substrate and may not apply if the liquid is a mixture (Mackay and Wesenbeeck, 2014).

$$ER = 1464 \times P \times Mw \quad (1)$$

where ER is the chemical evaporation rate in $\mu\text{g m}^{-2}\cdot\text{h}^{-1}$, which is estimated as the product of the saturated vapor concentration and a mass-transfer coefficient (mass based). P is the vapor pressure in Pa , and Mw is the molecular weight in g mol^{-1} .

Diesel evaporation rate as a function of vapor pressure and molecular weight was investigated and calculated for this study (Figure.5.2). Figure.5.2 plots molecular weight \times vapor pressure versus diesel evaporation rate with the constant (0.00284) designed in our experimental systems for all the #2 diesel samples and several intermediate volatile organic compounds (IVOCs). The evaporation rates of IVOCs are described in detail in Li et al. (2018). Vapor pressure of n-Pentadecane was used as the vapor pressure for #2 diesel samples (Alnajjar et al., 2010). #2 diesel samples data fell onto the linear trend established by the IVOCs and were clustered in the lower part of the figure ($R^2=0.96$), which indicates that the diesel evaporation rates not only depend on their vapor pressures, but also correlate with their molecular weights. This work extends the application of Mackay and Wesenbeeck's method (2014) to diesel mixture.

$$ER_d = 0.00284 \times P_d \times Mw \quad (2)$$

where ER_d is the diesel fuel evaporation rate in g day^{-1} , P_d is the vapor pressure in mmHg , and Mw is the molecular weight in g mol^{-1} .

5.2.2: SOA formation

SOA formation is shown (Fig.4) from photo-oxidation of ten individual #2 diesel samples and FACE9A research diesel when oxidized in the presence of the surrogate, H₂O₂, NO_x and UV. The addition of H₂O₂ is to offset the loss of reactivity due to the addition of diesel and help form similar amount of ozone as in the surrogate-NO_x-H₂O₂ experiment. SOA formation from n-Pentadecane under the same experimental conditions is also shown for comparison (Figure 5.3). n-Pentadecane was selected as commercial #2 diesel fuels and the FACE9A research fuel have a normal distribution of n-paraffins peaking at ~C₁₅-C₁₇ and ~C₁₄-C₁₅, respectively (Chevron Corporation, 2007; Alnajjar et al., 2010); additionally, n-C₁₅ most closely matched the ER of the #2 diesel fuels. Surrogate-NO_x-H₂O₂ runs without injection of diesel formed negligible (< 9.2 μg m⁻³) amount of SOA (Figure 5.3) compared to the far greater SOA (> 288.6 μg m⁻³) formation when injecting diesel. Diesel samples formed approximately twice the SOA than that formed from n-Pentadecane, which is likely due to the presence of other heavier compounds (e.g., PAHs, heavier alkanes) in the diesel mixture, which is explained in greater detail later. Moreover, SOA formed rapidly after turning on black lights. The SOA formation from photo-oxidation of diesel in the presence of surrogate, NO_x, and H₂O₂ does not show great variability between diesel fuels (st.dev. <8.9%).

Figure 5.4 compares the SOA formation from the photo-oxidation of D1 with and without the presence of surrogate ROG mixture and with a surrogate-NO_x-H₂O₂ only run. The run

without surrogate ROG mixture formed more SOA, which are attributed to changes in the gas-phase chemistry leading to SOA formation.

5.2.3: Constraining SOA yield from diesel oxidation

Yield of D10 was estimated as a representative of all diesel fuels tested (Table S2) and yields for all other diesel samples are listed in table 1. The concentration of diesel injected was $\sim 1387 \mu\text{g m}^{-3}$ (~ 160 ppb) assuming density of 0.832 kg L^{-1} and a molecular weight of 212 g mol^{-1} (n-pentadecane). The SOA formed from photo-oxidation of D1 with surrogate, NO_x , and H_2O_2 was $417.6 \mu\text{g m}^{-3}$. n-Pentadecane also formed significant SOA ($177.6 \mu\text{g m}^{-3}$), which is, however, still much less than what we observed from diesel experiments. Chen et al., (2016) reported high SOA yields for naphthalenes, 1-methylnaphthalene, and 2-methylnaphthalene in the presence of H_2O_2 under low NO_x conditions. Therefore, both aromatics and other alkanes larger than n-Pentadecane act as significant contributors to SOA formation and close the gap between the SOA formation from diesel and n-Pentadecane.

To compare the SOA formation from diesel with that from other compounds, we calculated an effective SOA mass yield for diesel using the same approach as that of Odum and his coworkers (Odum et al. 1996, 1997a, 1997b). The effective SOA mass yield (Y) was defined as the ratio of the particle wall-loss-corrected SOA mass (ΔM_0) to the estimated mass of diesel reacted (ΔHC) (Eqs.3). The percentage of diesel reacted was

calculated by assuming that diesel undergoes a first order reaction with the OH radical (Eqs.3). Reordering Eqs. (4) gives Eqs. (5).

$$Y = \frac{\Delta M_0}{\Delta HC} \quad (3)$$

$$\frac{d[C_i]}{dt} = -k_{OH,C_i}[OH][C_i] \quad (4)$$

$$\ln\left(\frac{D_0}{D}\right) = k_{OH,C_i}[OH] * t_r \quad (5)$$

where $[C_i]$ is the diesel concentration in $\mu\text{g m}^{-3}$, k_{OH} is the reaction rate constant in cm^3 (molecules $\cdot\text{s})^{-1}$, $[OH]$ is the OH radical concentration in molecules/ cm^3 estimated from the measured decay of toluene (Eqs.4) (Hildebrandt et al. 2009, Jathar et al. 2013), D_0 is initial diesel concentration, D is final diesel concentration, and t_r is reaction time. The carbon number distribution was obtained from (Chevron Corporation, 2007) (Figure.5.5 (a)). The k_{OH} of n-alkanes (C_9 - C_{23}) are used to estimate fractional oxidation of diesel precursors, which is shown in Figure. 5.5 (b). Percentage of diesel fuel reacted and the peak shifts from C_{16} to C_{17} . The detailed calculation is in Table 5.3. The calculated yields are 20.3~37.7% for #2 diesel in the presence of surrogate and H_2O_2 with 25 ppb NO_x , which are comparable to yield of n-Heptadecane under similar experimental conditions (Li et al, 2018).

5.2.4: Effects of OH radical concentration on SOA formation from diesel

The OH concentration during diesel oxidation is estimated from the measured decay of toluene or *m*-xylene from the surrogate mixture using equation 5. Increasing SOA formation with increased OH radical concentration (Figure 5.6) is observed for low NO_x conditions. A linear regression model was applied to show this trend ($R^2=0.48$). Data reported by Jathar et al. (2013) on SOA formation from diesel fuels is also displayed in Figure 5.6. The experiments performed by Jathar et al. (2013) were under high NO_x conditions and typically had lower OH radical concentrations and lower SOA formation. The SOA formation from Jathar et al. (2013) is observed to be much lower than for the current study. To investigate whether NO_x or OH was driving this effect, an additional diesel oxidation experiment was performed with NO_x levels (1.1 ppm) comparable to the Jathar et al.'s work (2013). This run is marked as UCR very high NO. Comparable amounts of OH radical concentration to the low NO_x UCR runs were achieved by injecting H₂O₂. These experimental observations imply that the far higher SOA formation from our current diesel oxidation experiments results primarily from the lower NO_x levels, which are more consistent with urban atmospheres. Clearly at the higher NO_x concentrations the NO_x outcompetes the hydroperoxide radical for the peroxy and alkoxy radicals leading to higher vapor pressure oxidation products that therefore have a lower propensity to transition from the gas- to the aerosol-phase. The OH radical concentration achieved in this work is slightly higher than that in the Earth's atmosphere due to the addition of the surrogate ROG mixture.

5.2.5: Ozone formation

Figure 5.7 summarizes ozone formation from ten commercial diesel samples and a reference diesel fuel in the presence of the surrogate, NO_x and H_2O_2 . The ozone concentration achieved after approximately six hours ranged from 96 to 128 ppb, all considerably lower than the surrogate- NO_x - H_2O_2 only experiment. An enlarged view of the first 100 minutes of the experiment is provided as an inset to Figure 5.7 and illustrates that the ozone formation rates, indicated by the slope of the curves, were similar between the surrogate run and surrogate plus diesel runs. The reduction in total ozone formation is due to the presence of heavy alkanes in the diesel fuel, which serves as radical inhibitors by preventing HO_x cycling by generating RONO_2 instead of $\text{RO}\cdot$. Therefore, the overall hydroxyl concentrations available to oxidize both the diesel and the ozone forming surrogate are decreased resulting in lower ozone formation (Carter, 2011).

5.2.6: NO_x effects

Figure 5.8 and Figure 5.9 compare the SOA and ozone formation from photo-oxidation of D1 in the presence of surrogate and H_2O_2 at three typical urban NO_x levels and in the presence of NO and H_2O_2 at very high NO level. For these urban NO_x concentrations, contrary to earlier reported trends for very high NO_x levels, increasing NO_x loadings increased SOA and ozone formation. It is expected that components of the diesel fuels (e.g., long chain alkanes) act as a NO_x sink decreasing the ability of the system to recycle OH radicals thereby reducing the overall reactivity of the system. Therefore, increasing NO_x levels help to offset NO_x depletion allowing OH radical concentration to increase

with the increase of NO_x under low NO_x conditions (Table 5.4). The increased OH radical concentration thereby leads to higher SOA formation (Figure 5.6).

The overall ozone production for the surrogate system is known to be NO_x limited—ozone formation ceases as NO_x is depleted. In other words, greater reactivity is achieved (less fraction of NO_x consumed and greater consumption of secondary oxidation products through further oxidation) with higher NO_x concentrations. Nevertheless, the atmosphere is a very complex system, with continuous NO_x sources where combustion is present. In that case, the gas phase reactivity will be maintained. In addition, the plateau portion in Figure 5.9 is defined by depletion of NO_x . However, the run with extremely high NO injected formed far less SOA even though only one third of diesel was added compared with the 22 ppb NO_x case. Furthermore, ozone formation from the very high NO experiment was negligible.

The organic mass spectrum obtained from HR-ToF-AMS at 11 ppb NO_x concentration was plotted against the organic mass spectrum at 34 ppb NO_x concentration (Figure 5.9 (1)). The average organic mass spectra were normalized to the total organic signal. The two mass spectrums are almost identical, which indicates that NO_x concentration level does not play a significant role on diesel SOA oxidation pathway and significant changes for bulk chemical composition indicating uptake of NO_x into SOA is not observed when NO_x concentration was at high urban levels. However, Figure 5.10 (2) displays the normalized organic mass spectrum at 11 ppb NO_x concentration against the organic mass

spectrum at 1723 ppb NO concentration. The mass spectra for the experiment performed at higher NO_x concentration show higher even m/z peaks (fragments that include odd number of nitrogens), which is illustrated more clearly in the zoomed in plot. Figure 5.10 (3) shows the same high NO_x plot with the contribution of even m/z peaks removed. This normalized spectrum indicates that the fragmentation pattern of the SOA not containing nitrogen is extremely similar to that for the urban NO_x levels suggesting similarity in the non-nitrogen fragments leading to SOA formation in both systems. One third by mass of the fragments observed in the high NO_x system is attributed to nitrogen related compounds.

5.2.7: Trends in SOA elemental composition and SOA physical properties

The HR-ToF-AMS is widely used to characterize the bulk chemical composition of ambient organic aerosol. Table 5.1 summarizes the O:C and H:C ratios along with other physical properties including SOA density, volatile remaining fraction, and growth factor. Figure 5.11 displays molar ratios of H/C and O/C obtained from HR-ToF-AMS data on a Van Krevelen (VK) diagram to characterize the average oxidation products produced from photo-oxidation of unburnt diesel fuel samples under high and low NO_x conditions. Figure 5.11 (a) represents one of the photo-oxidation runs. The darker the marker, the later in the experiment the SOA composition was measured. As the SOA mass formed by photo-oxidation of diesel increased, the Oxygen-to-carbon (O/C) ratio increased very slightly, which indicates that the diesel SOA was not oxidized that much and could be first-generation oxidation products that therefore do not undergo multiple

generations of oxidation. Each data point in Figure 5.11 (b) represents the average over the final one hour of the experiment. All diesel data clustered closely, which implies that no conclusions of general differences among fuel manufacturers should be drawn from the limited number of samples obtained. The NO_x concentration does not affect SOA oxidation state.

Figure 5.12 plots the mass fraction of the AMS organic signal at $m/z = 44$ (f_{44}) versus that at $m/z = 43$ (f_{43}) for diesel SOA. This method was proposed by Ng et al., (2011). The m/z 44 and m/z 43 are prominent mass fragments in the AMS signal from SOA. The m/z 44 ion is dominated by the CO_2^+ ion and is thought to be due mostly to acids or acid-derived species. It implies the extent of oxidation of OA. The m/z 43 ion represents C_3H_7^+ and $\text{C}_2\text{H}_3\text{O}^+$ ions, where C_3H_7^+ is a hydrocarbon fragment and $\text{C}_2\text{H}_3\text{O}^+$ is predominantly due to non-acid oxygenated species. The dotted lines define the triangle space where ambient OOA components fall. Aging results in the f_{43} and f_{44} to evolve toward the apex of the triangle area ($f_{43} = 0.02$ and $f_{44} = 0.3$). Therefore, the more oxidized, low volatility organic aerosols, such as OOA and LV-OOA usually distribute in the upper portion of the triangle plot, while the less oxidized semi-volatile organic aerosols, such as SV-OOA distribute in the lower portion of the plot. Diesel SOA data under various NO_x conditions all clustered closely in the lower part of the triangle area, which is more similar to the less oxidized ambient SV-OOA.

Aerosol volatility provides indirect information on aerosol composition and vapor pressure of the condensable species (Emanuelsson, et al. 2013). The volume fraction

remaining (VFR) was collected from VTDMA, which heated particles to 100 °C for 17 seconds. Figure 5.13 presents the VFR for SOA formed from diesel fuel under high and low NO_x conditions. The VFR for diesel SOA increased sharply during the first 2 hours then reached a plateau, which indicates that the aerosol became less volatile over time then stabilized. Approximately 60% and 40% of diesel SOA evaporate under low NO_x and high NO_x at the end of the experiments, respectively.

In this dissertation, a single particle was placed in an 85% RH environment and the GF data was obtained from HTDMA. Figure 5.14 presents the GF for SOA formed from diesel fuel. The GF for diesel SOA increased slightly until reached 1.01 during the period of the experiments, which indicates that the SOA produced was quite hydrophobic.

5.3: Conclusion

Evaporation studies of diesel fuel indicate that only ~20% evaporated at 25 °C over a ten-month period; however, more is expected to evaporate at higher temperatures (e.g., typical summer roadway surface temperatures, lubrication of asphalt rollers, etc.). Environmental chamber photo-oxidation experiments of unburned diesel indicate rapid and significant amounts of SOA formation. Approximately twice the SOA was formed from diesel fuel compared with that from n-pentadecane leading us to the conclusion that there is a large potential of both aromatics and other alkanes larger than n-Pentadecane to contribute to SOA formation. Increasing NO_x concentration at urban NO_x levels enhanced SOA and ozone production due to enhancement of hydroxyl radical

concentrations within the environmental chamber. Nevertheless, SOA formation under previously reported extremely high NO_x concentrations led to nearly 14 times lower SOA formation while ozone formation was negligible compared with those under low NO_x condition. Therefore, operating the chamber under more relevant urban concentrations and reactivities greatly enhanced the measured aerosol formation potential of diesel fuel. Furthermore, two distinct SOAs were formed under low and high NO_x conditions in this study with a major fraction of the high NO_x system forming organic nitrates while little organic nitrate formation occurs when NO_x concentrations are in the tens of ppb. The trends observed during the current experiments demonstrate the importance of atmospheric NO_x concentrations; however, it is important to note that NO_x is continuously injected into the atmosphere in urban areas so further study is needed to determine the full impact of lowering NO_x emissions on atmospheric SOA formation from diesel fuel. The SOA produced in this work at urban NO_x concentrations is observed to be similar to the ambient semi-volatile oxygenated organic aerosol (SV-OOA) from AMS high resolution data. The diesel SOA produced does not undergo appreciable oxidation once formed suggesting that the SOA formed from photo-oxidation of diesel is first generation.

Tables & Figures

Table 5. 1: List of experiments.

Expt. #	Compound	HC ₀ ^a	NO ^b	NO ₂ ^b	H ₂ O ₂ ^b	Surr ^c	Time ^d	OH exposure ^e × 10 ⁸	SOA	Yield	O:C ^g	H:C ^g	VFR ^g	GF ^g
		μl	ppb	ppb	ppm	ppmC	min	Molec cm ⁻³ min	μg m ⁻³	%				
1	D1 ^h	150	15.1	6.9	1	1	360	-	417.6	-	0.3	1.8	0.4	1.02
2	D2	150	14.2	7.1	1	1	360	10.4	361.0	28.8	0.3	1.8	0.4	1.00
3	D3	150	13.9	6.3	1	1	361	5.2	375.3	37.7	0.3	1.8	0.4	1.01
4	D4	150	16.6	7.5	1	1	360	20.8	372.8	26.0	0.3	1.8	0.4	1.01
5	D5	150	14.4	7.5	1	1	360	-	371.3	-	0.3	1.8	0.4	1.02
6	D6	150	14.5	7.1	1	1	426	6.2	324.1	30.5	0.3	1.8	0.4	1.02
7	D7	150	14.5	6.9	1	1	402	10.8	349.0	27.6	0.3	1.8	0.3	1.01
8	D8	150	15.4	7.1	1	1	360	20.8	291.2	20.3	0.3	1.8	0.4	-
9	D9	150	16.2	6.6	1	1	457	-	356.1	-	0.3	1.8	-	-
10	D10	150	13.4	6.5	1	1	434	15.6	360.9	26.3	0.3	1.8	0.3	-
11	FACE9 A	150	17.1	6.4	1	1	362	1.3	288.6	49.3	0.4	1.7	0.4	-
12	n-C ₁₅ ^l	127 ^j	19.8	10.4	1	1	295	17.6	177.6	17.0	0.2	1.9	0.3	-
13	S1 ⁱ	*	14.4	6.9	1	1	360	-	1.6	-	-	-	-	-
14	D1 ^h	150	21.4	13	1	1	453	6.8	460.1	41.9	0.3	1.8	-	1.01
15	D1 ^h	150	7.3	3.9	1	1	394	2.8	313.7	40.4	0.3	1.8	0.3	1.02
16	D1 ^h	50	172	*	1	*	289	4.7	29.6	3.1	0.3	1.8	0.6	-
17	D1	150	20.1	11.8	1	*	289	9.3	504.4	41.6	-	-	-	-

a: Initial volume of compound injected; b: Initial NO, NO₂ and H₂O₂ concentration before turning blacklights on; c: Surrogate ROG mixture; d: Irradiation Time; e: Calculated from toluene or *m*-xylene decay; f: Averaged density over the entire course of the experiment; g: Data represent the average over the final one hour of the experiment; h: Experiments conducted under three different initial NO_x concentrations for studying NO_x effects using D1 #2 diesel fuel (Fig. 8 and Fig. 9); i: S1 and S3: Surrogate-NO_x-H₂O₂ only runs; j: A density of 1.4 g cm⁻³ was chosen for surrogate only experiment based on previous experimental data; k: 127 μl n-Pentadecane was used to generate the same initial concentration (μg m⁻³) as that for diesel experiments (150 ul); l: n-Pentadecane; “-”: data not collected; “*”: Chemicals not injected; O:C: Oxygen-to-carbon ratio; H:C: Hydrogen-to-carbon ratio; VFR: Volume fraction remaining; GF: Growth factor.

Table 5. 2: Mass loss of different #2 diesel brands in 9 months.

Diesel	Initial weight (g)	Final weight (g)	Percentage loss ^a (%)	Evaporation rate ^b (g day ⁻¹)
D1	1.5543	1.2032	22.6	0.0058
D2	1.5444	1.2335	20.1	0.0045
D3	1.5505	1.2600	18.7	0.0039
D4	1.5413	1.2121	21.4	0.0046
D5	1.5523	1.2298	20.8	0.0050
D7	1.5588	1.2102	22.4	0.0052
D8	1.5414	1.2082	21.6	0.0054
D10	1.5447	1.2186	21.1	0.0050

^a Percentage loss = (Initial weight – Final weight)/Initial weight.

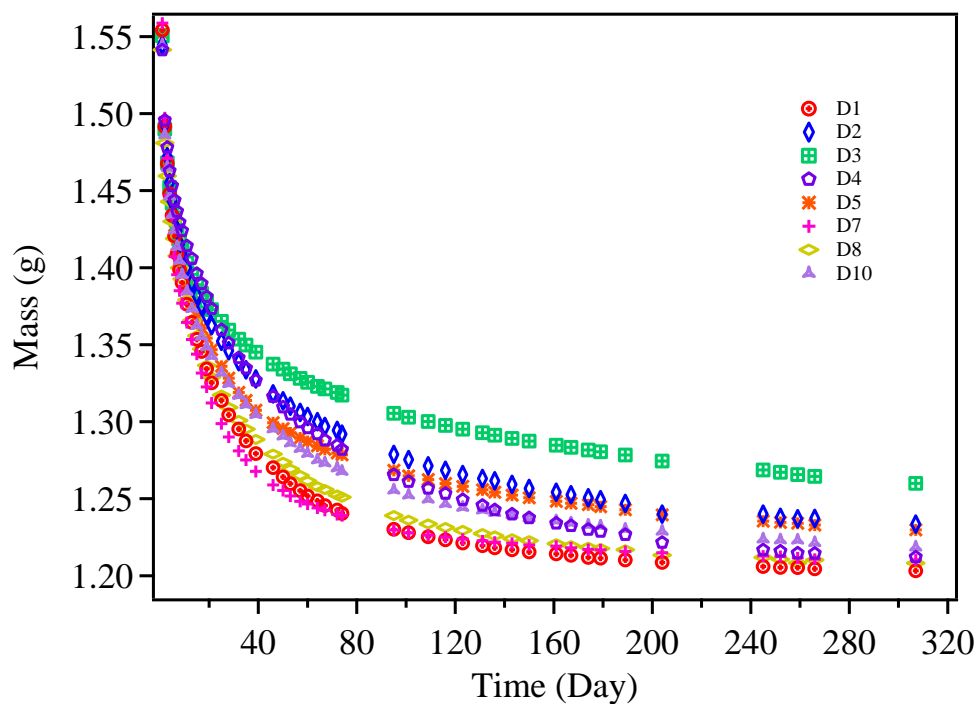
^b Evaporation rate = Initial slope

Table 5. 3: The percentage of diesel reacted (D10).

Carbon #	mass% ug	concentration ug/m3	k_{OH} ($cm^3 molec^{-1}s^{-1}$)	[OH] (molecule cm^{-3})	% reacted
9	1.6	17.79	9.70E-12	3.59E+06	0.59
10	3	33.35	1.10E-11	3.59E+06	0.64
11	4.8	53.36	1.23E-11	3.59E+06	0.68
12	6.2	68.92	1.32E-11	3.59E+06	0.71
13	7.6	84.48	1.51E-11	3.59E+06	0.75
14	9.5	105.60	1.79E-11	3.59E+06	0.81
15	10.5	116.72	2.07E-11	3.59E+06	0.85
16	11.4	126.72	2.32E-11	3.59E+06	0.88
17	10.6	117.83	2.85E-11	3.59E+06	0.93
18	9.8	108.94	3.51E-11	3.59E+06	0.96
19	9	100.04	4.32E-11	3.59E+06	0.98
20	7.3	81.15	4.32E-11	3.59E+06	0.98
21	6	66.70	4.32E-11	3.59E+06	0.98
22	3.2	35.57	4.32E-11	3.59E+06	0.98
23	2.7	30.01	4.32E-11	3.59E+06	0.98

Table 5. 4: List of NO_x effect runs.

Expt.#	Compound	NO_x ppb	OH exposure $\times 10^8$ Molec $cm^{-3}min$	SOA $ug m^{-3}$
15	D1	11	2.8	313.7
1	D1	22	3.2	417.6
14	D1	34	6.8	460.1
16	D1	1723	4.7	29.6



• D1-D10: Commercial #2 diesel fuel samples.

Figure 5. 1: Mass loss of diesel fuel samples in evaporation chambers.

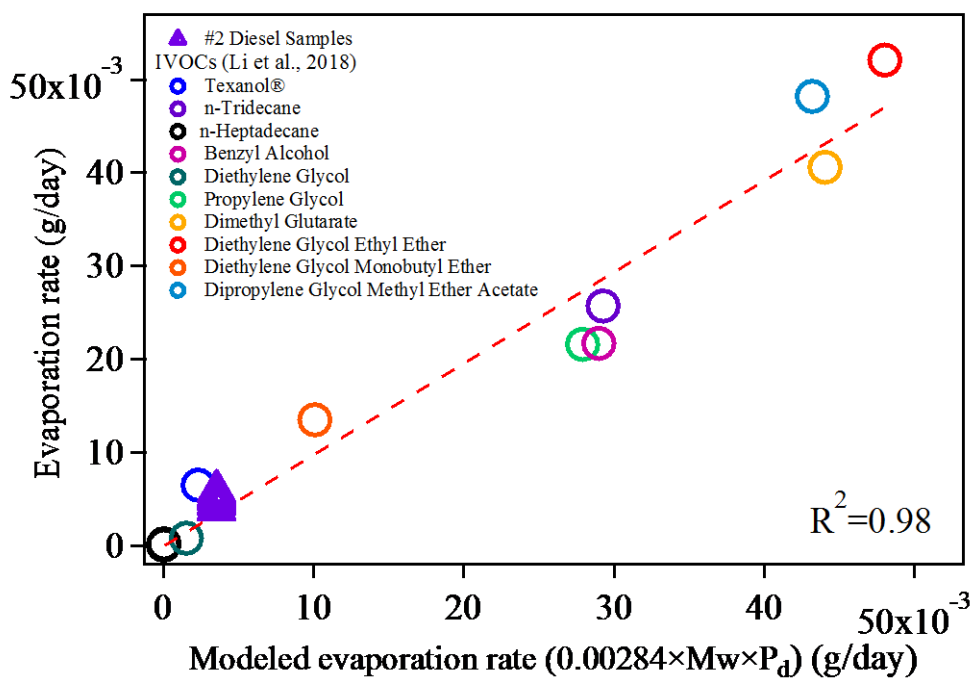


Figure 5. 2: Evaporation Rates of # 2 diesel samples (Table S1). Vapor pressure of n-Heptadecane was used as the vapor pressure for #2 diesel samples.

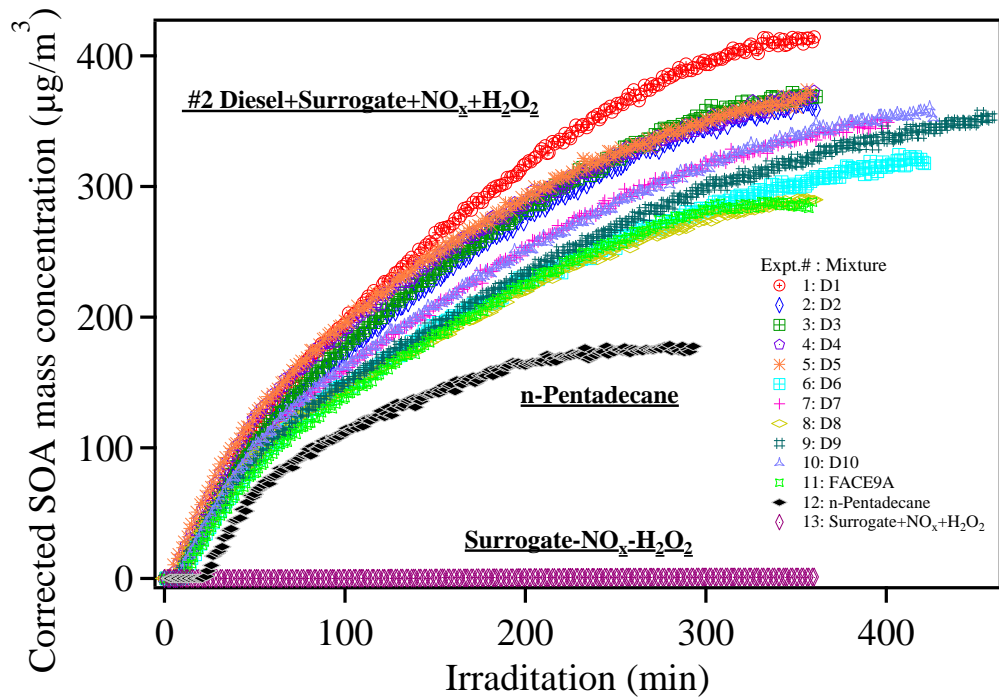


Figure 5. 3: SOA formation from photo-oxidation of ten #2 diesel samples and FACE9A research diesel fuel with surrogate, NO_x, and H₂O₂. SOA formation from n-Pentadecane under the same experimental condition and Surrogate-NO_x-H₂O₂ run were shown as comparison.

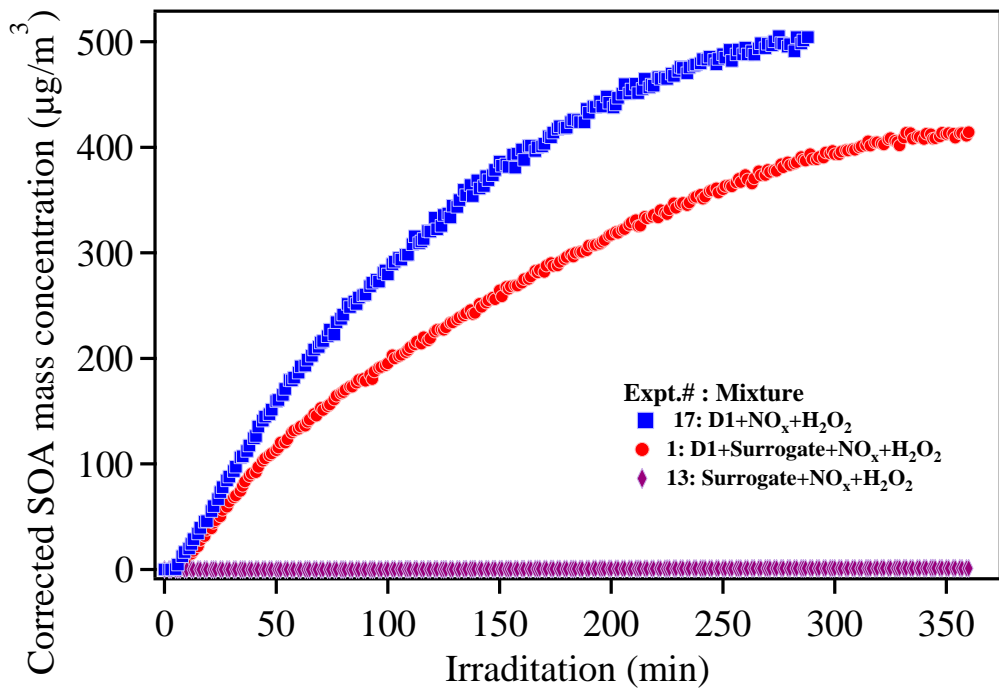


Figure 5. 4: SOA formation comparison from photo-oxidation of D1 with and without the presence of surrogate ROG mixture. Surrogate-NO_x-H₂O₂ run was shown as comparison.

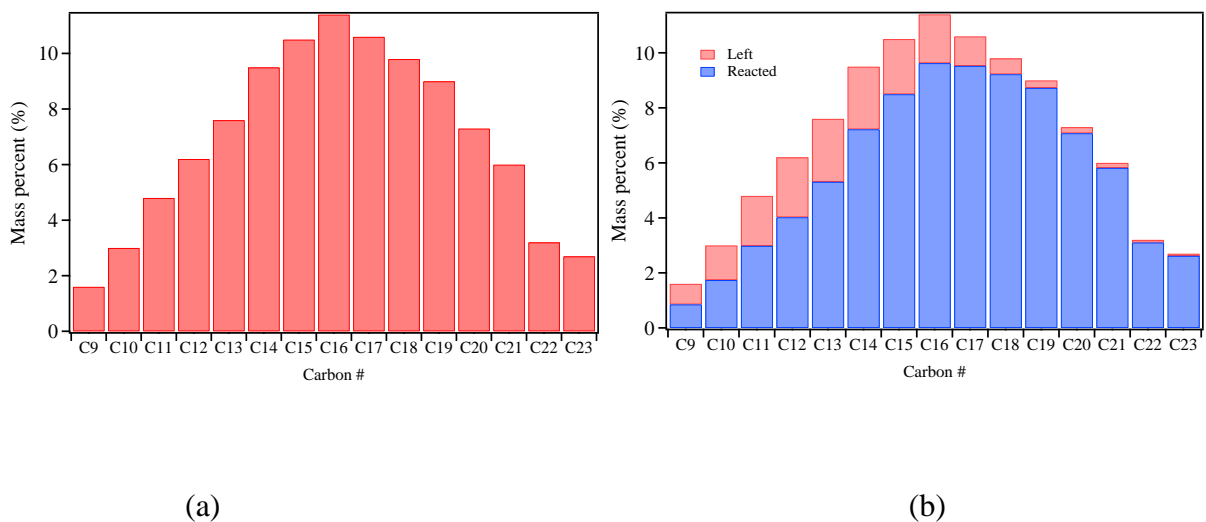


Figure 5.5: # 2 diesel carbon distribution (Chevron Corporation, 2007). (b): Blue represents percentage of diesel reacted.

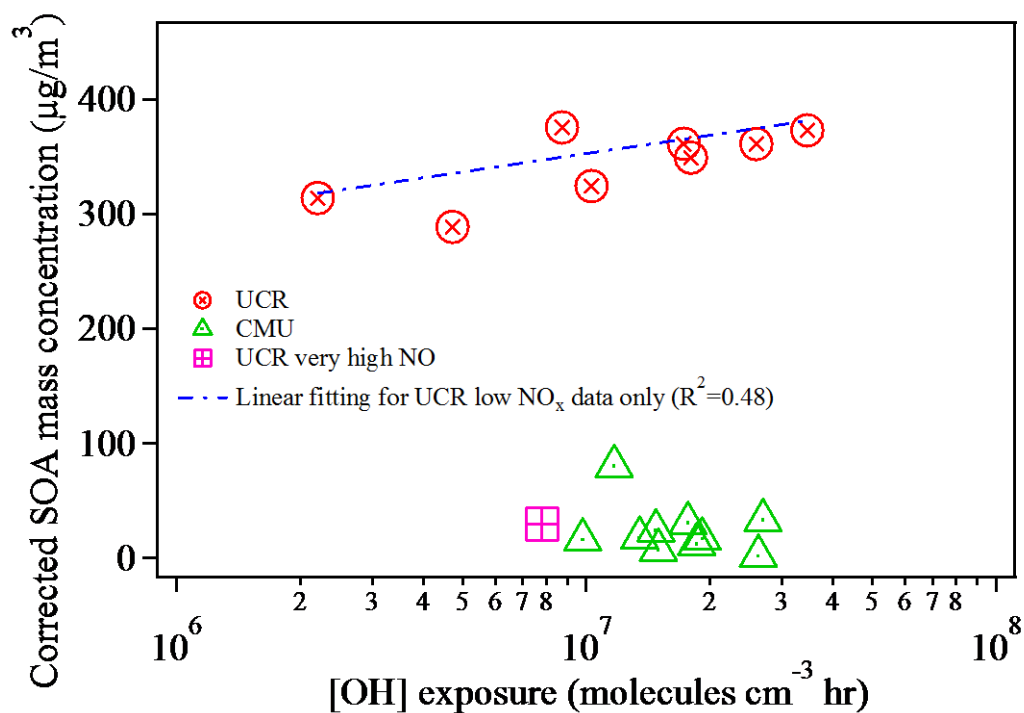


Figure 5.6: SOA formation as a function of OH radical concentration.

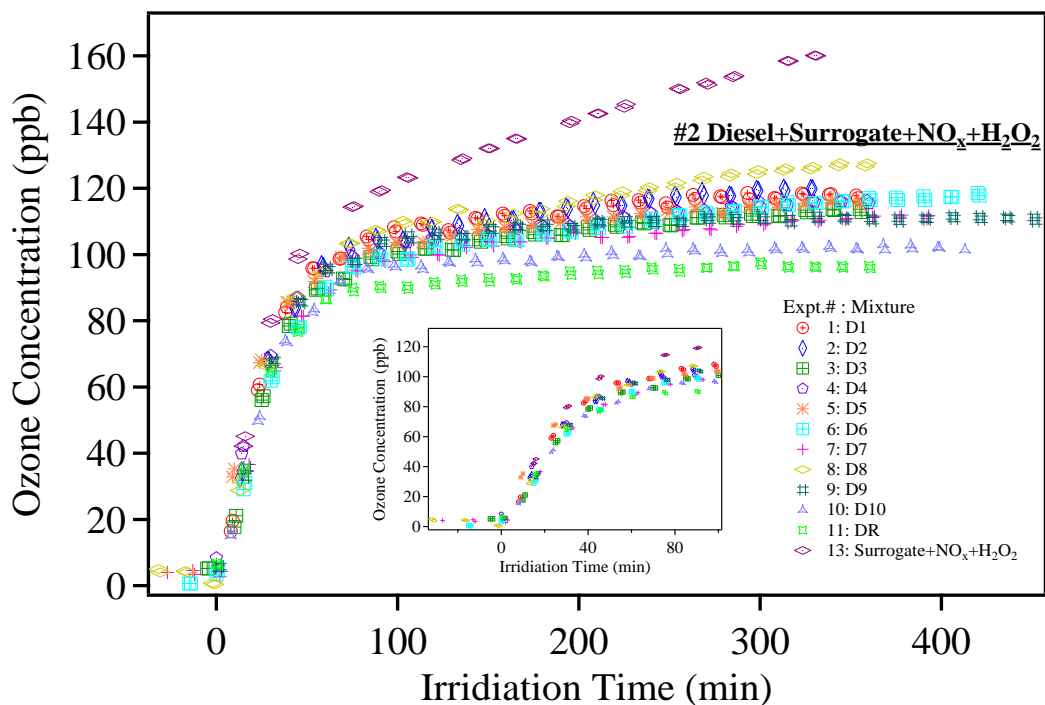


Figure 5. 7: Ozone formation from photo-oxidation of ten #2 diesel sample and one reference diesel with surrogate, NO_x , and H_2O_2 .

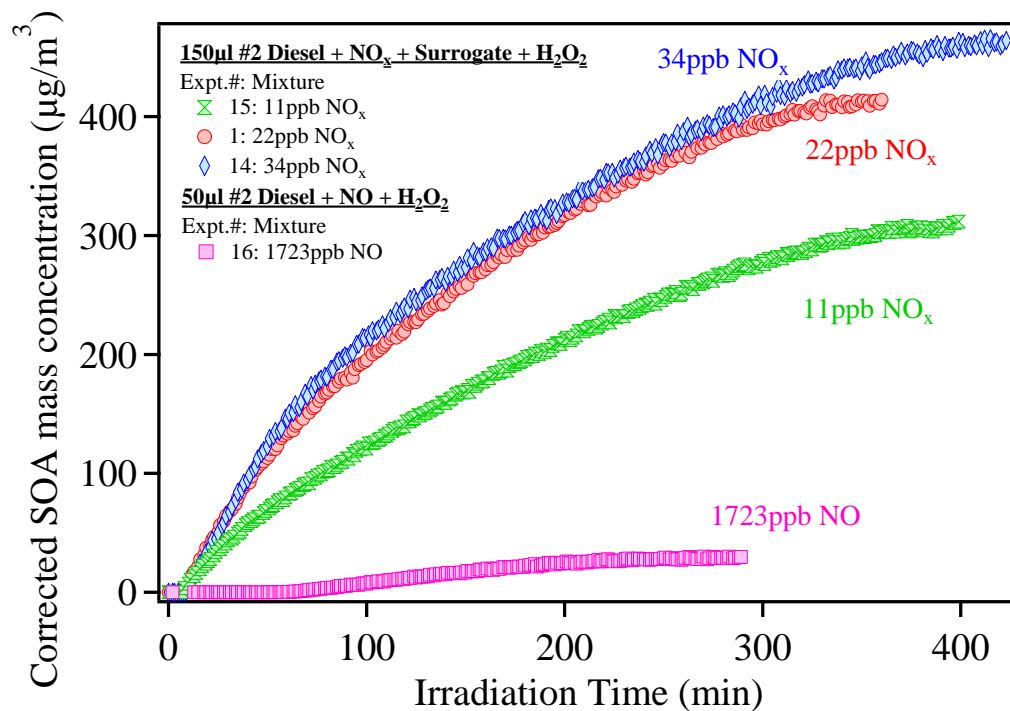


Figure 5. 8: SOA formation from photo-oxidation of D1 with H_2O_2 at various NO_x concentrations. Surrogate ROG mixture was added to low NO_x runs.

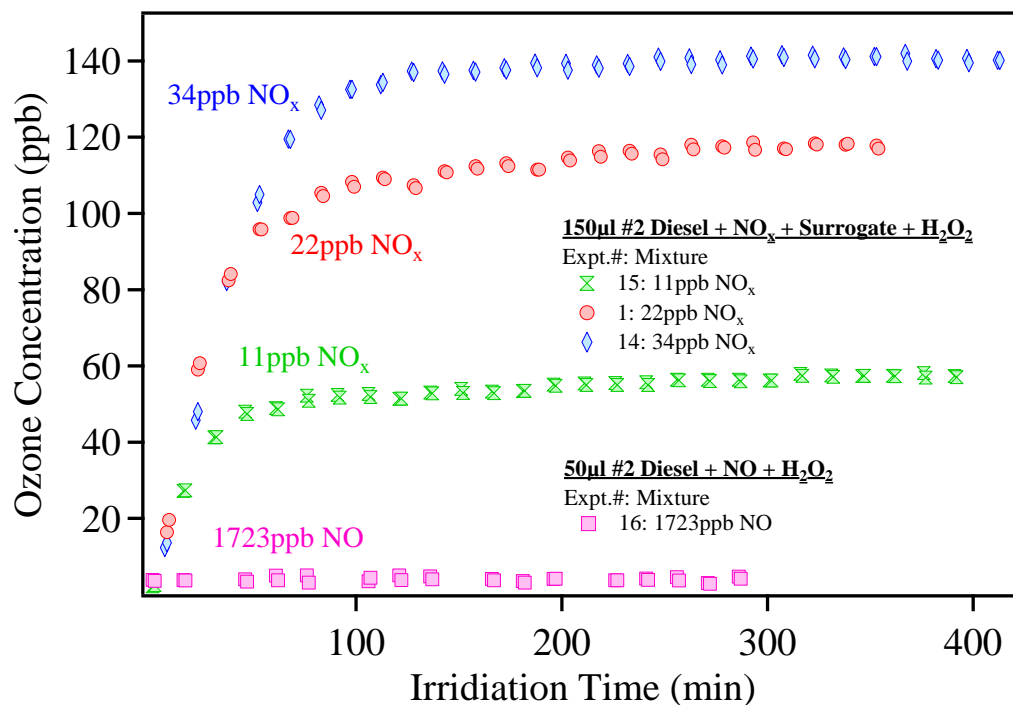


Figure 5.9: Ozone formation from photo-oxidation of D1 with surrogate and H₂O₂ at various NO_x concentrations.

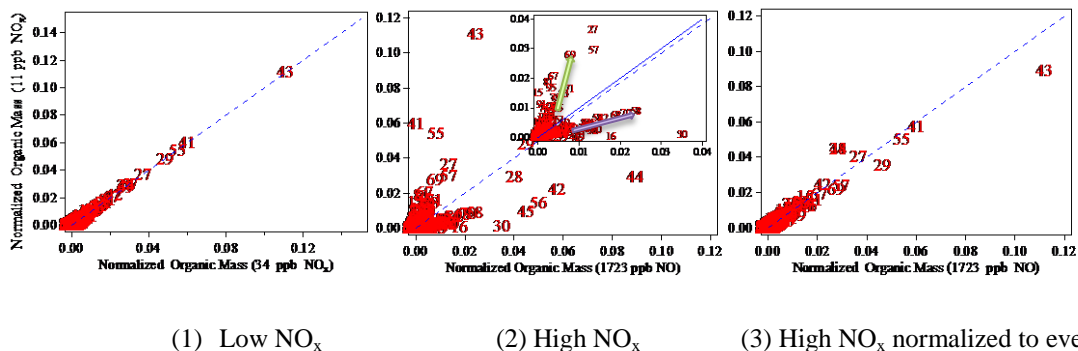
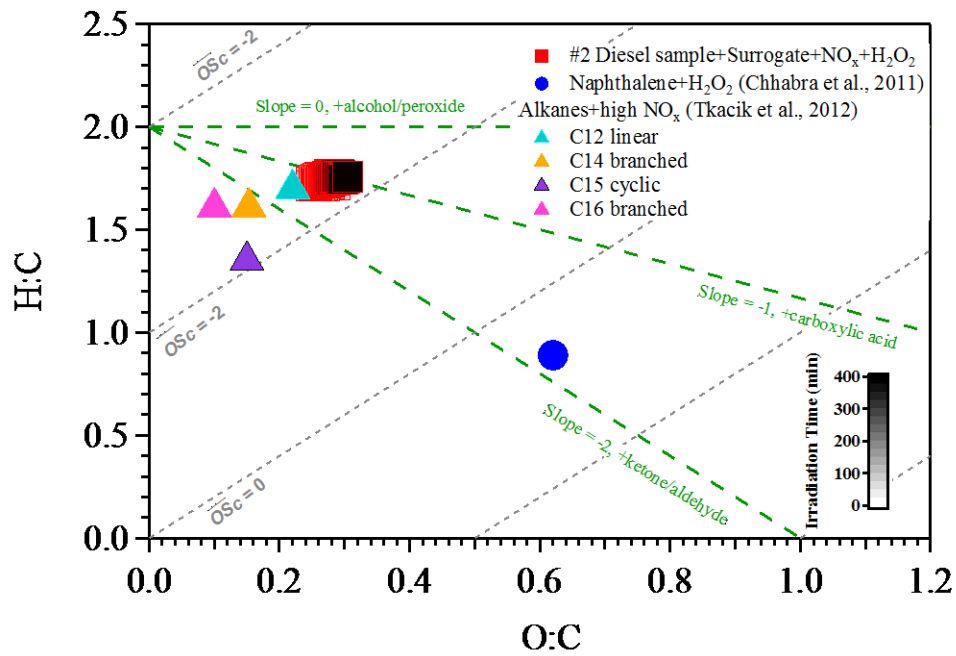
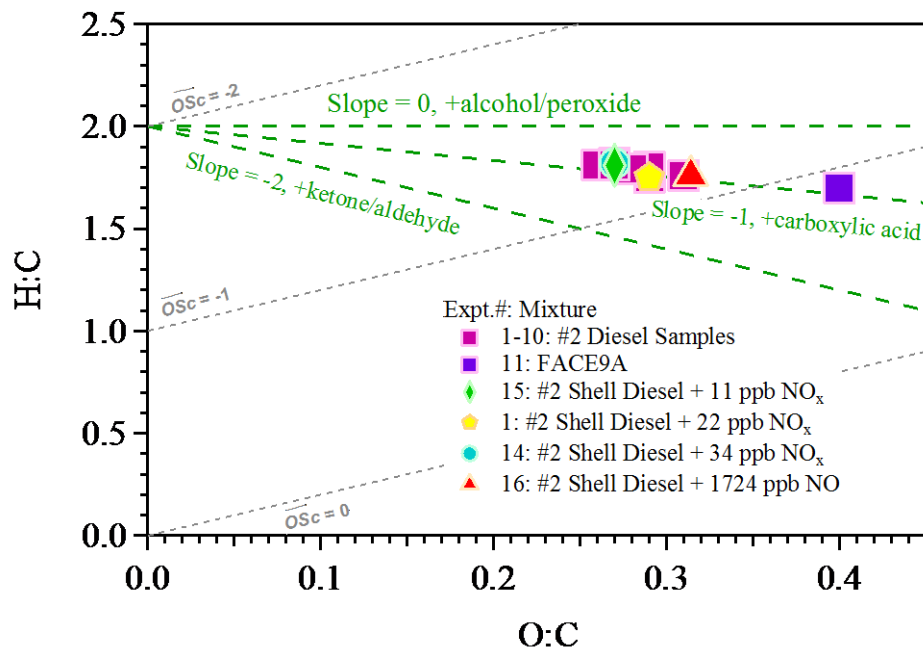


Figure 5.10: (1) Organic mass spectra of 34 ppb NO_x versus 11 ppb NO_x (normalized to total mass). (2) Organic mass spectra of 1723 ppb NO versus 11 ppb NO_x (normalized to total mass) (3) Organic mass spectra of 1723 ppb NO versus 11 ppb NO_x (normalized to (total mass – mass due to even m/z numbers)).



(a)



(b)

Figure 5. 11: Van Krevelen diagram of #2 diesel SOA. Dotted green lines show slopes of 0, -1 and -2. Solid grey lines show \overline{OSc} of 0, -1 and -2. (a) Single run; (b) All runs colored by NO_x conditions. Each maker represents the average over the final one hour of the experiment.

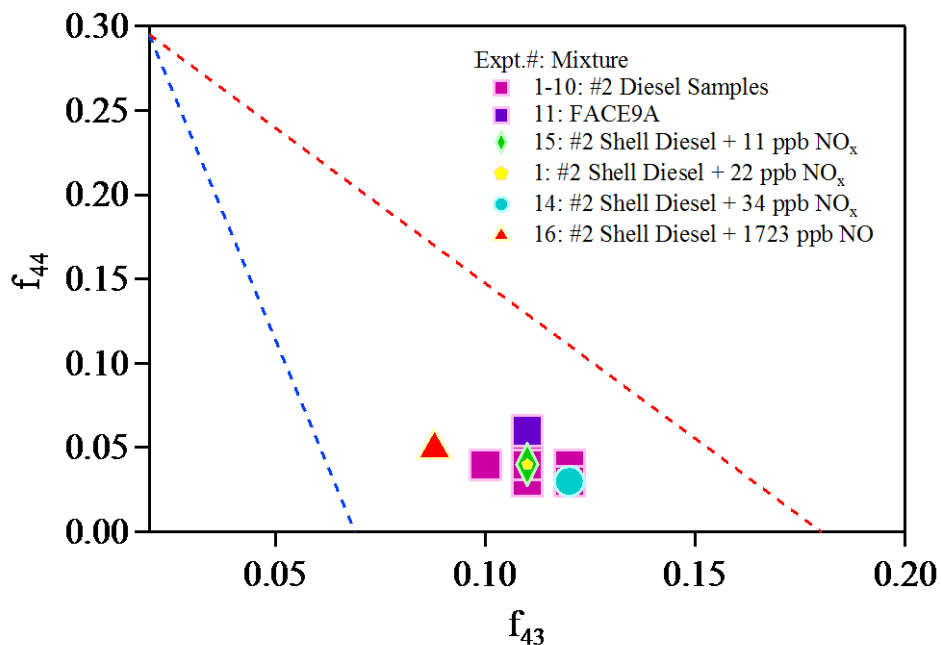


Figure 5. 6: The fractions of total organic signal at m/z 43 (f_{43}) vs. m/z (f_{44}) at the end of each experiment together with the triangle plot of Ng et al. (2011). The dotted lines define the space where ambient OOA components fall. The ranges of f_{44} observed for SV-OOA and LV-OOA components are 0.03–0.11 and 0.13–0.21, respectively. Each maker represents the average over the final one hour of the experiment.

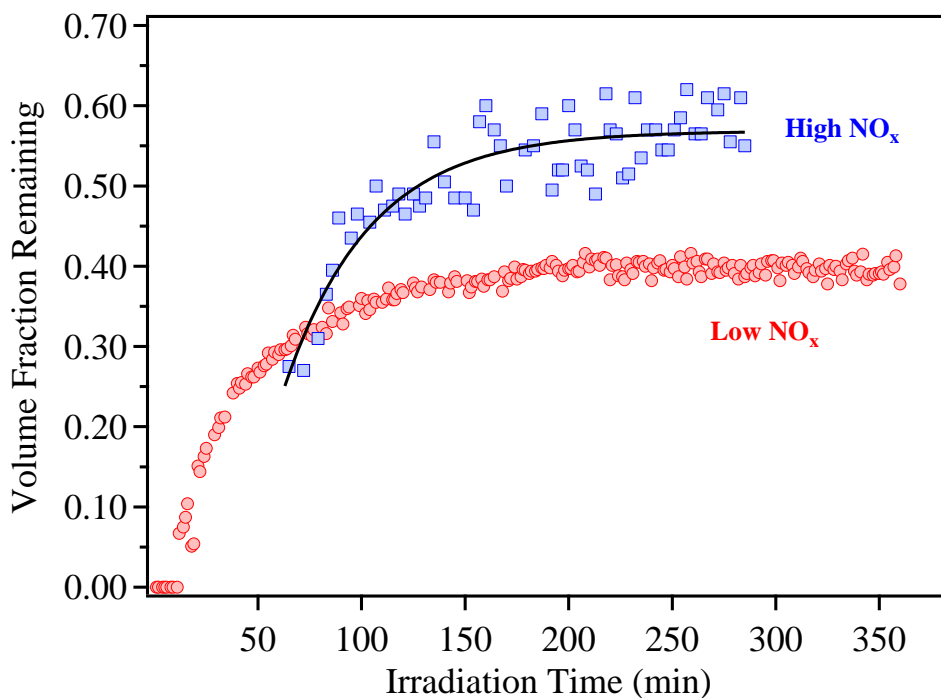


Figure 5. 7: VFR of diesel SOA.

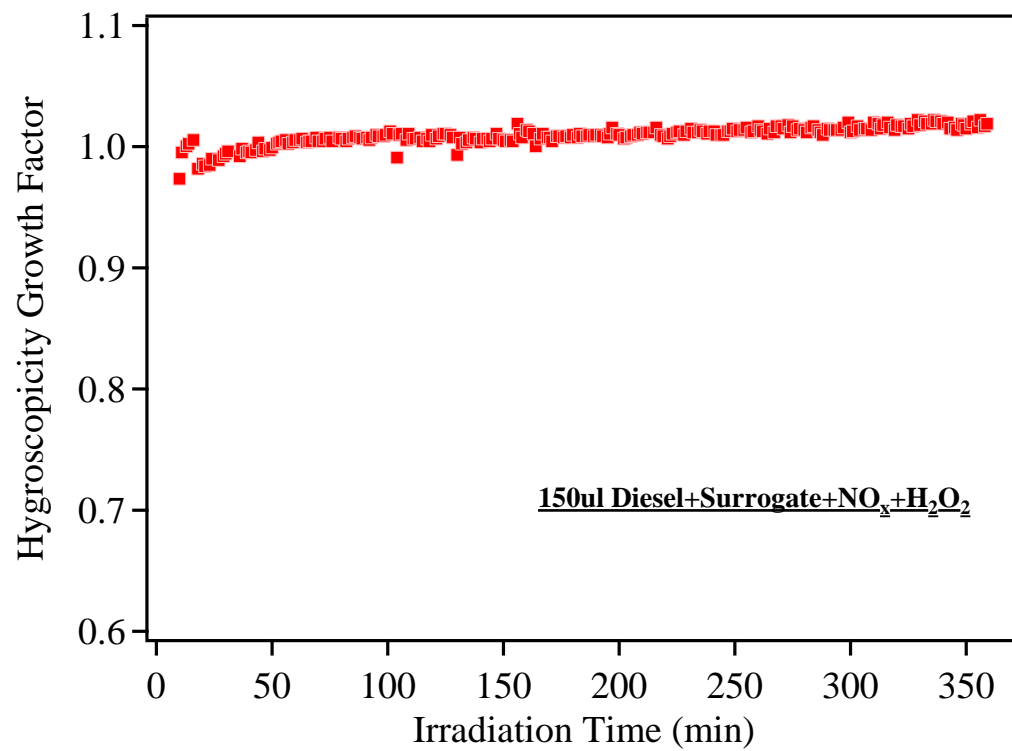


Figure 5. 8: Hygroscopicity growth factor of diesel SOA.

Chapter 6: Secondary Organic Aerosol and Ozone Formation from Photo-oxidation of Unburned Whole Gasoline in a Surrogate Atmospheric Environment

6.1: Introduction

Secondary organic aerosol (SOA) contributes to a significant fraction of the sub-micrometer atmospheric organic aerosol mass and therefore has vital impacts on global climate change, visibility, and human health (Pope et al., 2002, Maria et al., 2004; Naeher et al., 2007; Yee et al., 2013; Fiore et al., 2015; Pöschl and Shiraiwa, 2015; Fuzzi et al., 2015). However, there are still uncertainties about the reasons behind the gap between model prediction and actual observation, e.g., sources, and atmospheric chemistry. (Hallquist et al., 2009). Furthermore, tropospheric ozone at high concentrations affects human health and plant ecosystems deleteriously (Finlayson-Pitts et al., 1993).

Recent inventories show roughly equal contributions to total volatile organic compounds (VOC) emissions from tailpipe and evaporative sources (Environmental Protection Agency (EPA), 2008; California air resource board (CARB), 2012). Direct evaporation from unburned gasoline is an established important source of ozone and SOA forming precursors (EPA, 2008; CARB 2012). Evaporative emissions include the release of gasoline vapors resulting from diurnal temperature variations, hot soak (i.e., residual heat at the end of a trip), running losses, resting losses, and leaks and spills occurring at service stations (Gentner et al., 2009). As new vehicle control technologies continue to decrease primary organic aerosol and gas-phase emissions, whole fuel evaporation becomes a more significant source of organic emissions. Moreover, Gentner et al. (2012)

argue that unburned gasoline is an important component of tailpipe emissions from gasoline engines. Additionally, the composition of gasoline is representative of the complex atmospheric distribution of anthropogenic hydrocarbons in an urban atmosphere (Harley et al., 1992). Thus, determining the SOA and ozone forming potential of whole gasoline vapor is of great interest.

Gasoline composes a variety of hydrocarbons, and its composition differs according to crude oil sources, petroleum refining procedures, additives, and season, and changes according to governmental regulations. Gasoline is blended differently for summer or winter to meet volatility requirements. Petroleum refiners are required to switch between summer and winter blend gasoline twice per year in California. Volatility is directly related to the Reid vapor pressure (RVP) which is the vapor pressure of the gasoline blend at 38 °C (Hajipour et al., 2014). Winter blend gasoline has a higher RVP and is of higher volatility. The reason for that is winter blend gasoline need to be able to evaporate at cold temperatures for the engine to operate properly. Summer blend gasoline has a lower RVP in order to avoid excessive evaporation during hot summer days, which can contribute to reduction of ozone and SOA concentrations.

SOA formation from components of gasoline such as aromatics and alkanes has been individually studied under controlled conditions. The SOA yields increase with increasing carbon number for linear n-alkanes and cyclic alkanes (Lim and Ziemann, 2009a; Presto et al., 2010). For a given carbon number, yields follow the order cyclic >

linear > branched (Lim and Ziemann, 2009b). SOA formation from photo-oxidation of aromatics has been investigated extensively (Derwent et al., 2010; Nakao et al. 2012; Li et al., 2016). However, studies on how these complex mixtures behave in the atmosphere are limited. Odum et al. (1997a, 1997b) study SOA forming potential from photo-oxidation of 12 unburnt gasoline blends using a smog chamber facility. They find that aromatics are the class of compounds that are responsible for producing the majority of the SOA formed during the atmospheric oxidation of whole gasoline vapor. This finding is confirmed by a few research groups (Gentner et al., 2012; Jathar et al., 2013). Modelling studies report a substantially low yield (0.0024 ± 0.0001) for nontailpipe gasoline emissions (Gentner et al., 2012). Jathar et al. (2013) show a yield of 0.01-0.03 for photo-oxidation of unburnt gasoline. However, these previous smog chamber studies are conducted at relatively high NO_x concentrations. The SOA formation from these precursors are sensitive to NO_x concentrations and yields are higher under urban relevant low initial NO_x concentrations (Loza et al. 2014; Li, et al., 2015).

Given changes in fuel formulations, increased knowledge on impact of reactivity on SOA formation (not investigated in earlier work), potential evaporative losses of unburnt fuels to the atmosphere, and improved experimental photochemical chambers and instrumentation, a new study of whole gasoline aerosol and ozone formation is conducted. This pilot study uses the state-of-the-art chamber facility at UCR CE-CERT to evaluate SOA and ozone formation from photo-oxidation of whole gasoline blends under relative urban NO_x concentrations in the presence of a surrogate mixture, which is

applied to control the chamber reactivity and mimic urban atmospheric activity. The SOA mass yields, ozone formation, NO_x effects on SOA and ozone formation, and bulk SOA chemical composition and physical properties are studied.

6.2: Results and discussion

6.2.1: SOA formation from photo-oxidation of unburnt whole gasoline

Figure 6.1 illustrates the SOA formation from individual winter blend gasoline when oxidized in the presence of the surrogate, H₂O₂, NO_x and UV. Surrogate-NO_x-H₂O₂ run is shown as comparison. As mentioned in the experimental section, the surrogate is a simplified chemical mixture mimicking urban atmosphere reactivity. The use of the surrogate mixture in a photo-oxidation system is used to study the effects of individual compounds on overall SOA and ozone formation. Briefly, the chemicals contained in the ROG mixture are selected and measured by both the abundance and atmospheric reactivity potential (via maximum incremental reactivity (MIR) value) of the different VOCs to identify one representative chemical compound to be the bulk percentage of that category. And the surrogate ROG mixture has very low SOA formation in the absence of a test VOC. H₂O₂ is added to reduce the impact of hydroxyl radical loss due to reactions of the hydrocarbon of interest. As shown in Figure 6.1, surrogate-NO_x-H₂O₂ run only formed 2.6 μg m⁻³ SOA. SOA formation is approximately ten times higher after adding gasoline sample to the surrogate-NO_x-H₂O₂ system. Remarkable consistency of SOA formation regardless of fuel manufacturer or octane rating (varied by a factor of 2) is observed, which indicates that the results obtained should be generally true for gasoline

fuels in the Southern California Air Basin. No conclusions of general differences among fuel manufacturers should be drawn from the limited number of samples obtained.

Figure 6.2 compares the SOA formation from winter and summer gasoline blends. As shown in figure 2.2, composition of winter and summer gasoline blends are different. Small constituent changes could lead to a certain degree differences on SOA formation. However, two of the winter blends (WP4 and WP510) form more SOA than their summer counterparts while three of the winter blends form (WP3, WR4, and WR5) form less SOA. General trends in SOA formation between winter and summer blends are not observed.

6.2.2: Yield of Unburned Gasoline SOA

An effective SOA mass yield is calculated for all gasoline samples studied using the same approach as that of Odum et al. (Odum et al. 1996, 1997a, 1997b). The effective SOA mass yield (Y) is equal to the ratio of the particle wall-loss-corrected SOA mass (ΔM_0) to the estimated mass of gasoline reacted (ΔHC) (Eq.2). The percentages of gasoline components reacted are calculated by assuming that gasoline components go through a first order reaction with the OH radical, which is shown in equation 3. Solution to equation 3 leads to equation 4.

$$Y = \frac{\Delta M_0}{\Delta HC} \quad (2)$$

$$\frac{d[C_i]}{dt} = -k_{OH,C_i}[OH][C_i] \quad (3)$$

$$\ln\left(\frac{C_0}{C}\right) = k_{OH,C_i}[OH] * t_r \quad (4)$$

where $[C_i]$ is the individual gasoline component concentration in $\mu\text{g m}^{-3}$, k_{OH} is the reaction rate constant in $\text{cm}^3 (\text{molecules}\cdot\text{s})^{-1}$ of that component, $[OH]$ is the OH radical concentration in molecules cm^{-3} , which is estimated from the measured decay of toluene (Eq. 1) (Hildebrandt et al. 2009, Jathar et al. 2013), t_r is reaction time. The k_{OH} of gasoline components are taken from literature (Table 6.2) (Jathar et al., 2013). The initial individual gasoline component concentration is calculated based on gasoline composition data (Table 2.3). The calculated yields are listed in Table 6.1.

6.2.3: NO_x effects on SOA formation

Aerosol yields are generally higher at lower NO_x concentrations for benzene, toluene, and *m*-xylene (Song et al., 2005). However, SOA formation increased with increasing NO_x concentrations in this study (Figure 6.3), which indicates that greater reactivity is maintained (fraction of NO_x consumed is less) with higher NO_x concentrations (higher OH concentration).

6.2.4: Effects of OH radical concentration on SOA formation

Figure 6.4 (a) compares the SOA formation from photo-oxidation of WGS9 in the presence of surrogate and NO_x with or without H₂O₂ added. Figure 6.4 (b) plots the SOA formation against OH exposure. By adding H₂O₂, 2.3 times more SOA is formed. The OH exposure in the H₂O₂ run is 15% higher than that without H₂O₂ run (Table 6.1). Therefore, the presence of H₂O₂ greatly enhances reactivity and SOA formation.

Figure 6.5 shows the SOA formation as a function of OH radical concentration from photo-oxidation of gasoline sample. Data from Jathar et al. (2013) is also plotted as comparison. Gasoline SOA data correlates well with aromatic mixture SOA data under urban relevant NO_x conditions indicated by the increased R². The hydroxyl radical concentration is estimated from the measured decay of toluene or *m*-xylene, which is shown in Eq. (1) (Hildebrandt et al., 2009; Jathar et al., 2013). From Figure 6.5, we can see that the greater the estimated hydroxyl radical concentrations, the more SOA forms under urban relevant NO_x conditions, which supports the SOA trends discussed above where the greater the reactivity, the greater the SOA formation. SOA formation under high NO_x conditions is low, which is due to formation of RONO₂, which is more volatile and has a lower tendency to partition to the aerosol phase. Similar trend is found for photo-oxidation of unburnt diesel fuel as well (Li et al, 2018).

$$\frac{d[\textit{toluene}]}{dt} = -k \cdot [\textit{OH}][\textit{toluene}] \quad (1)$$

6.2.5: Aromatic content vs SOA formation

SOA formation is plotted as a function of aromatics content in Figure 6.6. A weak trend (R²=0.24) of higher SOA formation coupled with higher aromatic content are observed, which is consistent with literature work (Odum et al., 1997a, 1997b). This trend, however, is not observed for alkanes and olefins. Figure 6.7 compares SOA and ozone formation from photo-oxidation of WR5 and the aromatic mixture, the concentration of which matches the concentration of gasoline aromatic content in the smog chamber. The

aromatic mixture forms more SOA and ozone, which indicates that the presence of other compounds, likely alkanes, in gasoline sample suppress the consumption of aromatic contents resulting in lower ozone and SOA formation. The OH exposure is approximately two times higher in aromatic mixture experiment than that in gasoline experiments. The consumption difference is due to the difference in OH exposure.

The organic mass spectrum obtained from HR-ToF-AMS at 20 ppb NO_x is plotted against the organic mass spectrum at 41 ppb NO_x (Figure 6.8). The average organic mass spectra are normalized to the total organic signal. The two mass spectrums are almost identical, which indicates that NO_x concentration level does not play a significant role on gasoline SOA oxidation pathway when NO_x concentration is not very high.

6.2.6: Trends in SOA elemental composition and SOA physical properties

An established technique for determining trends in aerosol elemental composition is through the triangle plot described in Ng, et al. (2011), which plots the ratio of HR signals of CO₂⁺ to total signal in the component spectrum versus HR signals of C₂H₃O⁺ to total signal in the component spectrum. The edges of the triangle plot define the space where ambient data reside. Figure 6.9 presents the triangle plot for gasoline SOAs. Isooctane SOA in the presence of NO and aromatic mixture SOAs, m-xylene SOA, and m-xylene/toluene SOA in the presence of NO_x and H₂O₂ are shown for comparison. Both winter and summer gasoline SOAs cluster together with aromatic mixture SOA and single aromatic SOA, which indicates the similarity of their elemental compositions.

Furthermore, both winter and summer gasoline SOAs fall in the lower but outside of the triangle plot, which may not be surprising because of the complex sources of ambient SOA. The triangle plot suggests that gasoline SOAs are more similar to the less oxidized ambient semi-volatile oxygenated organic aerosol (SV-OOA) (Chhabra et al. 2011).

The Van Krevelen diagram, generated from Aerodyne HR-ToF AMS, is widely applied to characterize the average oxidation products produced from SOA forming precursors. Organic aerosol evolution is traced in the Van Krevelen diagram along a line of a particular slope (e.g. A slope of -2 is generated by replacing an aliphatic functionality with a carbonyl functionality.) (Ng, et al. 2011).

Figure 6.10 plots molar ratios of H:C and O:C on a Van Krevelen diagram for SOA produced from photo-oxidation of unburnt summer and winter blend gasoline fuels. Aromatic mixture SOAs and single aromatic SOAs under similar experimental conditions are shown as comparison. SOA formed from photo-oxidation of alkanes with various structures under high NO_x conditions are plotted. Each data point in Figure 6.10 represents the average over the final one hour of the corresponding experiment. Compared with alkanes SOA, all gasoline SOA data cluster closely with aromatics SOAs, which implies the similarity between gasoline SOAs and aromatics SOAs.

The volume fraction remaining (VFR) for SOA formed from winter and summer blend gasoline are shown in table 6.1. Winter blend gasoline SOA has a comparable VFR value

to that of summer blend SOA. Winter blend gasoline SOA also has similar final one hour O:C ratio to that of summer blend SOA. Figure 6.11 compares the VFR of gasoline SOA with m-xylene SOA and aromatic mixture SOA. Gasoline SOAs share similar VFR to m-xylene SOA. But aromatic mixture SOA has a much higher VFR than gasoline SOAs. Aromatic mixture SOA is also more oxidized than gasoline SOAs, indicated by the higher O:C ratio (Figure 6.). The VFR of aromatic mixture SOA increases rapidly during the first 2 hours of the experiment and then reaches a plateau, which indicates that lower volatility stuff is rapidly formed during the first one hour of irradiation. Slightly before the experiment ends, approximately 53% of the aromatic mixture SOA evaporates.

Figure 6.12 presents the GF for SOA formed from winter and summer blend gasoline. The GF for gasoline SOA remains a constant (1.01-1.03) during the period of the experiments. GF is very near 1 indicating that the SOA produced is quite hydrophobic.

6.2.7: Ozone formation from photo-oxidation of gasoline

Figure 6.13 presents ozone formation from ten winter gasoline blends in the presence of the surrogate ROG mixture, NO_x , and H_2O_2 together with an inset plot that reveals the first 100 minutes of each experiment using a magnified scale. The black empty diamond represents ozone formation from photo-oxidation of surrogate, NO_x , and H_2O_2 , which is shown for comparison and called as surrogate only run. The ozone concentration attained ranges from 96.5 to 114.9 ppb after approximately six hours' irradiation, all noticeably lower than that generated from the surrogate only run (No gasoline added). Similar ozone

formation rates are achieved for both surrogate only run and surrogate plus gasoline runs before plateauing due to the similar NO_x conditions. This observed ozone reduction at the plateau is due to the presence of aromatics in gasoline sample, which removes NO_x at a faster rate leaving less NO_x available to form ozone (Carter, 2011).

Figure 6.14 compares the ozone formation from photo-oxidation of winter and summer blends gasoline. The slightly higher ozone formation is due to the slightly higher initial NO_x concentration and the less aromatic present in the gasoline sample. No conclusions of general differences among winter and summer gasoline blends should be drawn from the limited number of samples obtained. Figure 6.15 compares the ozone formation from photo-oxidation of WR5 at three different NO_x levels in the presence of surrogate and H_2O_2 . The higher the NO_x concentration, the higher the ozone formed. This indicates that gasoline is probably behaving as a NO_x sink, which reduces the total reactivity of the environmental chamber system. Therefore, addition of greater quantities of NO_x leads to greater consumption of SOA precursors than in systems with lower NO_x concentrations, indicated by the increased OH radical concentration with increased NO_x concentration in Table 6.3. Ozone formation at 41ppb NO_x level is delayed due to a high initial NO concentration, which suppresses ozone formation (Li, et al., 2015). Additionally, when NO_x is consumed completely, which indicated by the starting point of the plateau portion in Figure 6.15, ozone growth rate is slowed dramatically; however, SOA formation continues to increase.

Figure 6.16 compares the ozone formation from photo-oxidation of WP5 with and without the presence of H_2O_2 . By adding H_2O_2 into the experimental system, slightly less ozone is formed; however, the ozone formation rate during the first two hours of experiment is increased. The reduced ozone formation is probably due to formation of HNO_3 , which decreases the total amount of NO_x available to form ozone.

6.3: Conclusion

Environmental chamber photo-oxidation experiments of unburnt blend gasoline samples show consistent SOA formation regardless of fuel manufacturer and octane rating. Parameters that enhance SOA formation include aromatic content fraction of the gasoline sample, hydroxyl radical concentration, and NO_x concentration (within 100 ppb). There is a linear trend between SOA formation and OH exposure. The greater the percentage of aromatic content is, the more SOA forms. The overall SOA formation is OH driven in this work. NO_x is another parameter to tune hydroxyl radical concentration. Gasoline forms less SOA and ozone than its aromatic mixture counterpart, which indicates that other compounds in the gasoline mixture suppress SOA and ozone formation. General trends in SOA and ozone formation between winter and summer gasoline blends are not found. The gasoline SOA generated at urban relevant NO_x levels is similar to the ambient SV-OOA from AMS high resolution data.

Tables & Figures

Table 6. 1: List of experiments.

Run #	Mixture	HC ₀ ^a	NO ^b	NO ₂ ^b	Surr ^c	H ₂ O ₂	OH Exposure ^d ×10 ⁶	SOA	Yield	H:C ^f	O:C ^f	VF R ^f	GF ^f
		ppb	ppb	ppb	ppmC	ppm	Molec cm ⁻³ hr	μg m ⁻³	%				
1	WR1	447	12.1	6.2	1.1	1	9.0	29.0	2.2	1.60	0.56	0.3	1.03
2	WP1	447	12.8	6.0	1.1	1	5.9	19.0	2.2	1.76	0.58	0.3	-
3	WR2	447	13.4	6.2	1.1	1	-	28.2	-	1.75	0.59	-	-
4	WP2	447	14.2	8.1	1.1	1	10.2	33.9	2.3	1.69	0.60	0.3	-
5	WR3	447	14.4	8.1	1.1	1	5.6	19.3	1.8	1.82	0.56	-	-
6	WP3	447	14.6	5.8	1.1	1	8.4	27.0	1.8	1.70	0.68	0.3	1.01
7	WR4	447	-	-	1.1	1	7.8	29.0	2.4	1.66	0.63	0.3	-
8	WP4	447	15.6	7.5	1.1	1	-	34.7	-	1.68	0.61	0.3	1.01
9	WR5	447	14.3	7.6	1.1	*	4.1	6.8	0.7	-	-	0.3	-
10	WR5	447	13.9	8.0	1.1	1	4.8	22.2	2.3	1.69	0.62	0.2	-
11	WR5 ^h	447	26.1	14.6	1.1	1	54.0	40.9	3.9	1.81	0.65	0.3	1.00
12	WR5 ^h	447	14.4	5.1	1.1	1	20.6	27.9	4.7	1.70	0.67	0.3	-
13	WP5	447	14.3	7.8	1.1	1	7.3	23.0	1.2	1.66	0.65	0.2	1.01
14	SP3	447	15.0	7.8	1.1	1	-	27.7	-	1.70	0.68	0.3	1.01
15	SR4	447	16.1	6.2	1.1	1	6.5	33.7	2.1	1.75	0.67	0.3	-
16	SP4	447	16.4	7.0	1.1	1	-	30.2	-	-	-	0.3	-
17	SR5	447	14.0	7.0	1.1	1	9.0	26.1	1.5	1.75	0.65	0.3	1.03
18	SP5	447	13.2	6.6	1.1	1	-	20.9	-	1.60	0.62	-	1.00
19	S ^h	*	14.0	8.3	1.1	1	8.7	2.8	-	-	-	-	-
20	Aromatics	134	13.1	8.3	1.1	1	15.9	45.6	8.7	1.67	0.68	0.5	-
21	Aromatics	134	14.1	8.2	1.1	1	14.4	49.7	9.8	1.64	0.73	0.4	-
22	<i>m</i> -xylene	75.5	16.2	8.2	1.1	1	9.7	44.7	14.1	1.50	0.50	0.3	-

a. Initial volume of gasoline injected; b: Initial NO, NO₂, H₂O₂ concentration before turning black lights on; c. Surrogate ROG mixture; d. Averaged density over the entire course of the experiment; e. Calculated from toluene or *m*-xylene decay; f. Averages over the final one hour of the experiment; g. Experiments conducted under different initial NO_x concentrations for studying NO_x effects using WGS9 (Figure 4); h. Surrogate-NO_x-H₂O₂ only runs; i. Assumed 1.4 g cm⁻³ is chosen for surrogate only experiment based on previous experimental data; “*”: Chemicals not injected; “-”: Data not collected; VFR: Volume fraction remaining; GF: Growth factor; Aromatic: Aromatic mixture.

Table 6. 2: The k_{OH} s of gasoline components (Jathar et al., 2013)

Chemical	Initial Concentration ($\mu\text{g m}^{-3}$)	k_{OH} ($\text{cm}^3 \text{ molecule}^{-1} \text{ s}^{-1}$)	$\Delta\text{HC}(\mu\text{g m}^{-3})$
butane	814.02	2.38E-12	60.17
2-Methylbutane	398.58	2.38E-12	29.46
Pentane	152.74	3.84E-12	17.79
2-Methylpentane	188.99	5.20E-12	29.15
Hexane	74.93	5.25E-12	11.65
2,4-Dimethylpentane	108.38	4.77E-12	15.44
Benzene	74.16	1.22E-12	2.87
Isocatane	20.76	8.16E-12	4.80
Heptane	38.82	6.81E-12	7.65
Toluene	295.02	5.58E-12	48.58
Octane	27.88	8.16E-12	6.45
Chlorobenzene	49.91	1.22E-12	1.93
<i>m</i> -Xylene	157.35	2.31E-11	82.59
<i>p</i> -Xylene	51.54	1.43E-11	19.03
<i>o</i> -Xylene	48.03	1.36E-11	17.04
1-Methyl-4-ethylbenzene	59.56	1.86E-11	26.85
1,3,5-Trimethylbenzene	32.55	5.67E-11	27.31
1-Methyl-2-ethylbenzene	15.74	7.00E-11	14.09
1,2,4-Trimethylbenzene	85.42	3.25E-11	55.44
1,2,3-Trimethylbenzene	14.73	3.25E-11	9.56
<i>p</i> -Diethylbenzene	13.67	3.25E-11	8.87
<i>o</i> -Diethylbenzene	12.25	3.25E-11	7.95
1,2,4,5-Tetramethylbenzene	7.49	3.25E-11	4.86
1,2,3,5-Tetramethylbenzene	9.67	3.25E-11	6.27
Naphthalene	18.44	2.30E-11	9.66
2-Methylnaphthalene	6.63	2.30E-11	3.48

Table 6. 3: List of NO_x effect runs.

Compound	NO_x	OH	SOA	Yield
	ppb	Molec cm^{-3}hr	$\mu\text{g m}^{-3}$	%
WR5	41	3.6E7	40.9	2.2
WR5	20	3.5E7	27.9	1.5

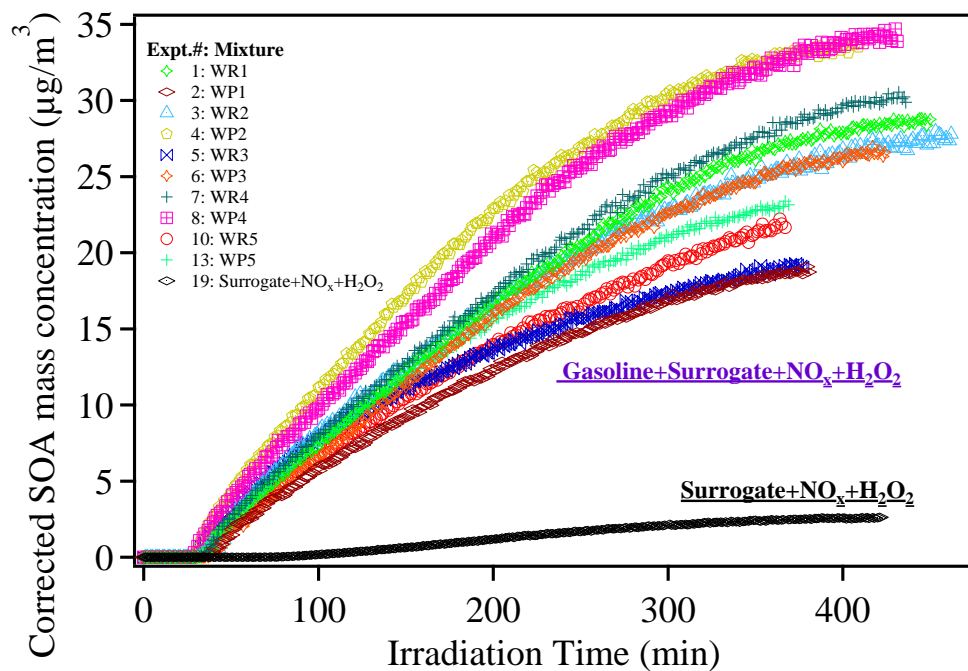


Figure 6. 1: SOA formation from winter blend gasoline with surrogate, NO_x and H₂O₂.

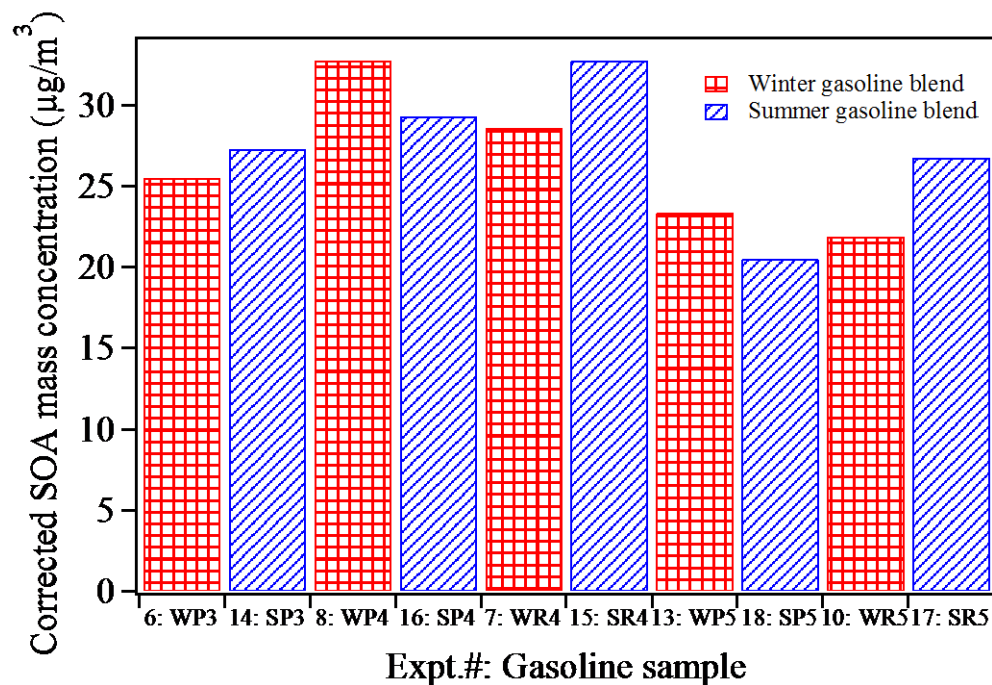


Figure 6. 2: Comparison of SOA formation from winter and summer blend gasoline with surrogate and H₂O₂

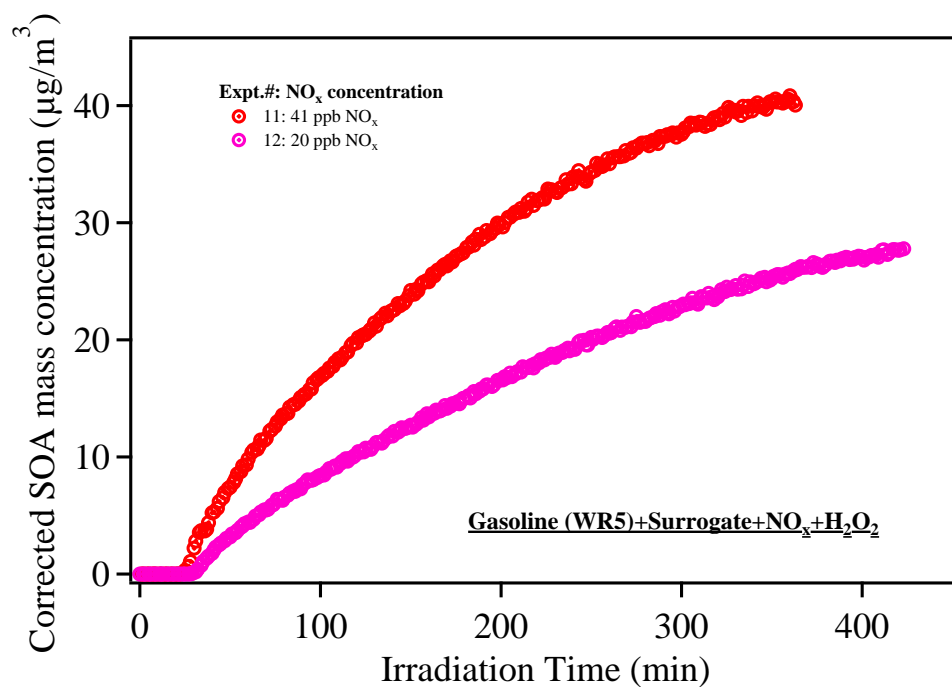


Figure 6. 3: SOA formation from photo-oxidation of WR5 with surrogate and H₂O₂ at various NO_x concentrations.

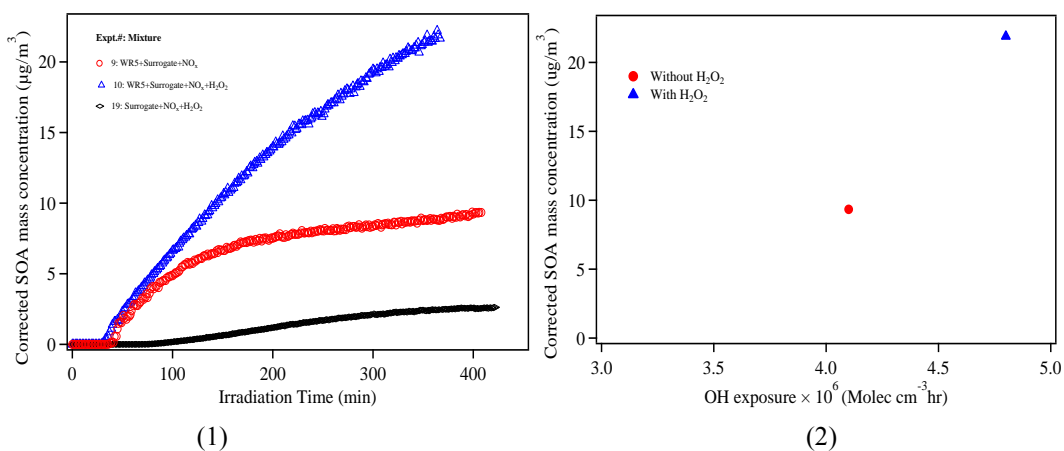


Figure 6. 4: (1) SOA formation from WR5 with surrogate, NO_x. H₂O₂ was added as needed. (2) OH exposure vs SOA formation.

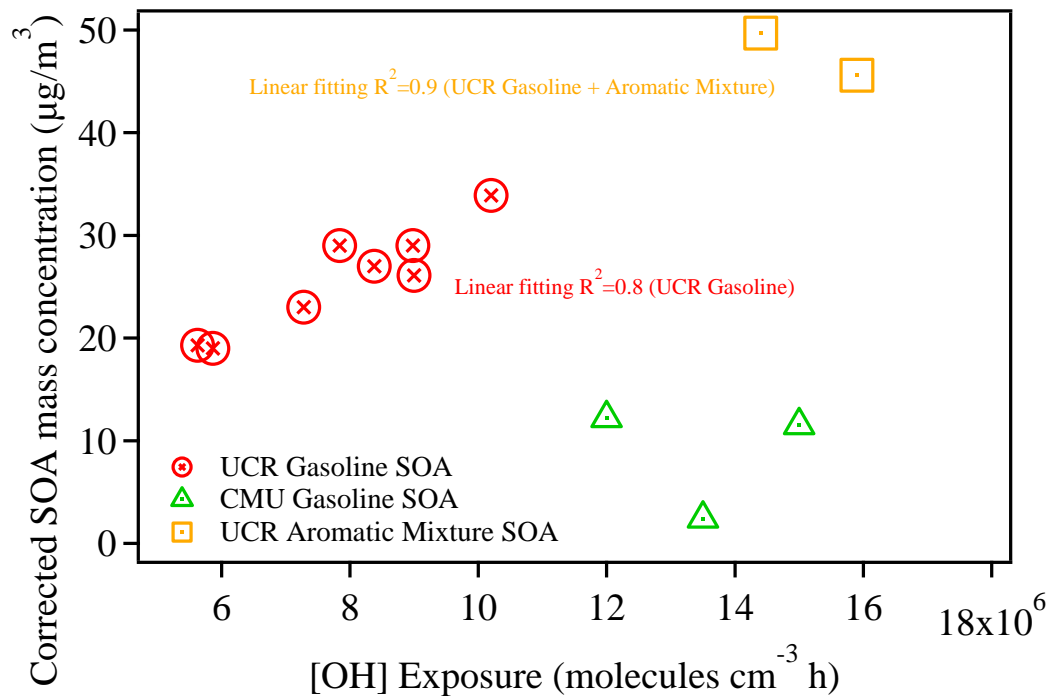


Figure 6. 5: SOA formation as a function of OH radical concentration under various NO_x conditions. (UCR gasoline: NO_x~25ppb; CMU gasoline: NO_x~100-400ppb; UCR aromatic mixture: NO_x~25ppb;)

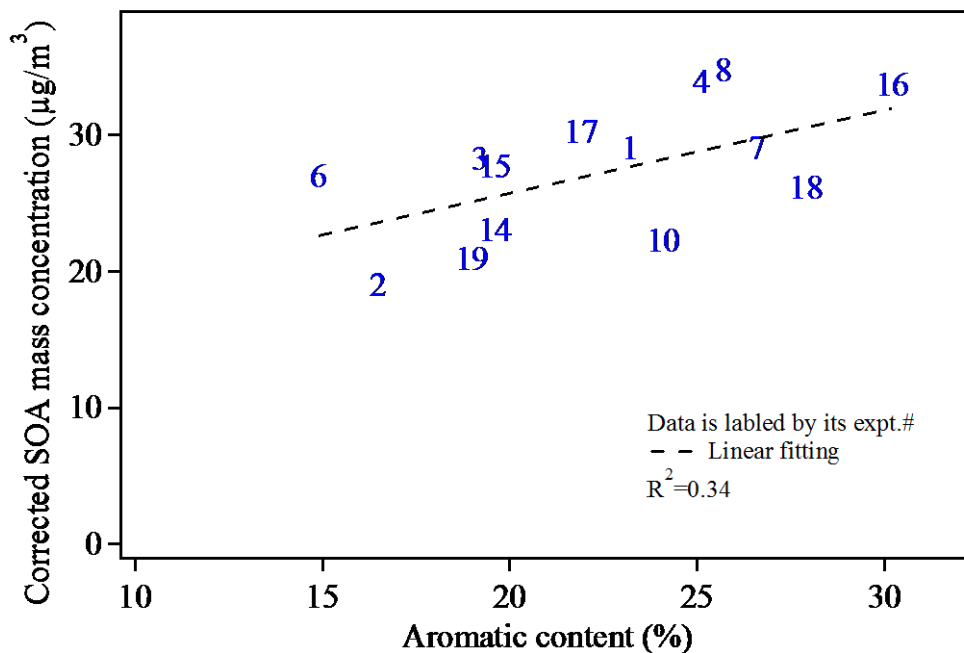


Figure 6. 6: SOA formation VS aromatics content.

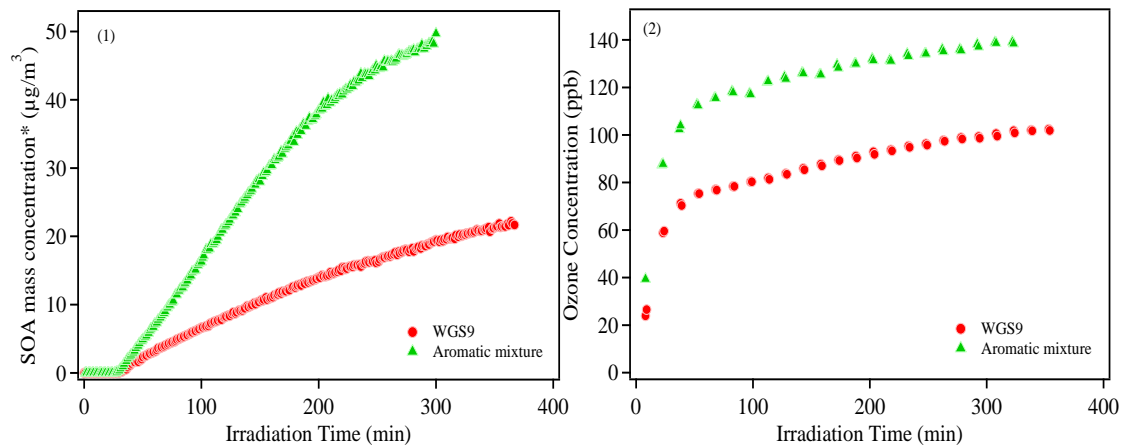


Figure 6. 7:

(1) SOA and (2) ozone formation from photo-oxidation of WR5 and the aromatic mixture in the presence of surrogate, NO_x and H_2O_2 .

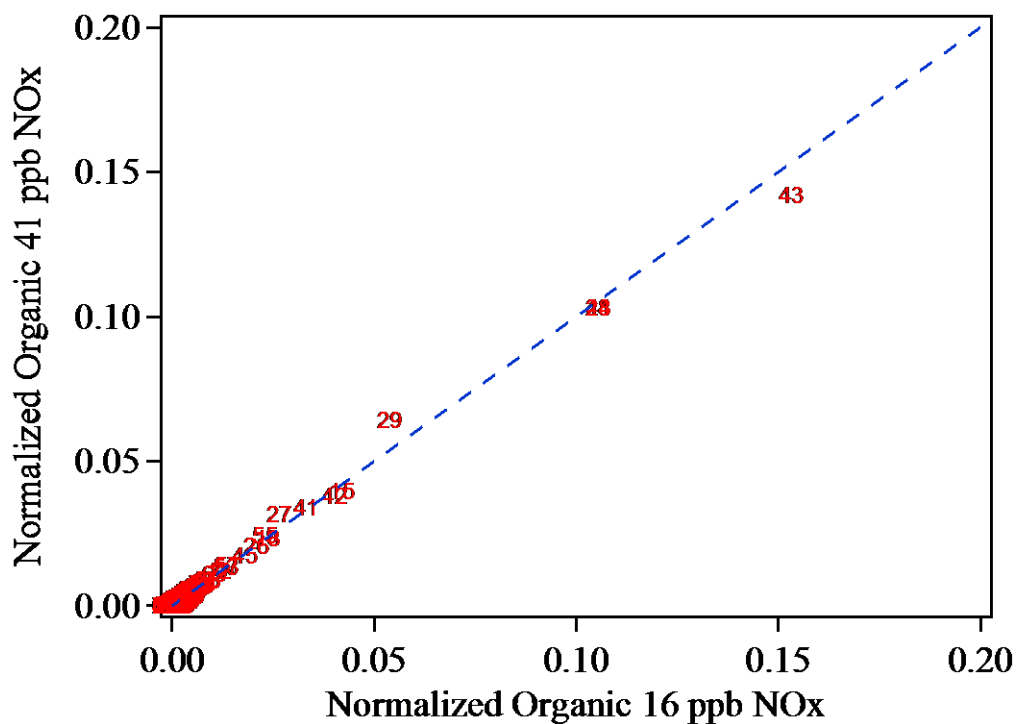


Figure 6. 8: Correlation plots of the organic mass spectra (normalized to total mass)

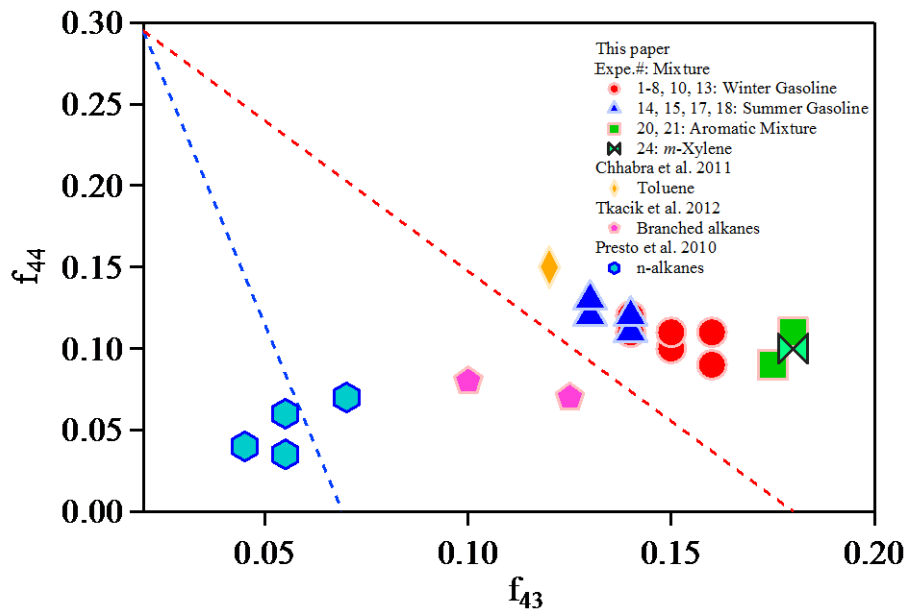


Figure 6. 9: Triangle plot for both winter and summer blends gasoline SOAs. The fractions of total organic signal at m/z 43 (f_{43}) vs. m/z (f_{44}) at the end of each experiment (Ng et al., 2010). The ranges of f_{44} observed for SV-OOA and LV-OOA components are 0.03–0.11 and 0.13–0.21, respectively.

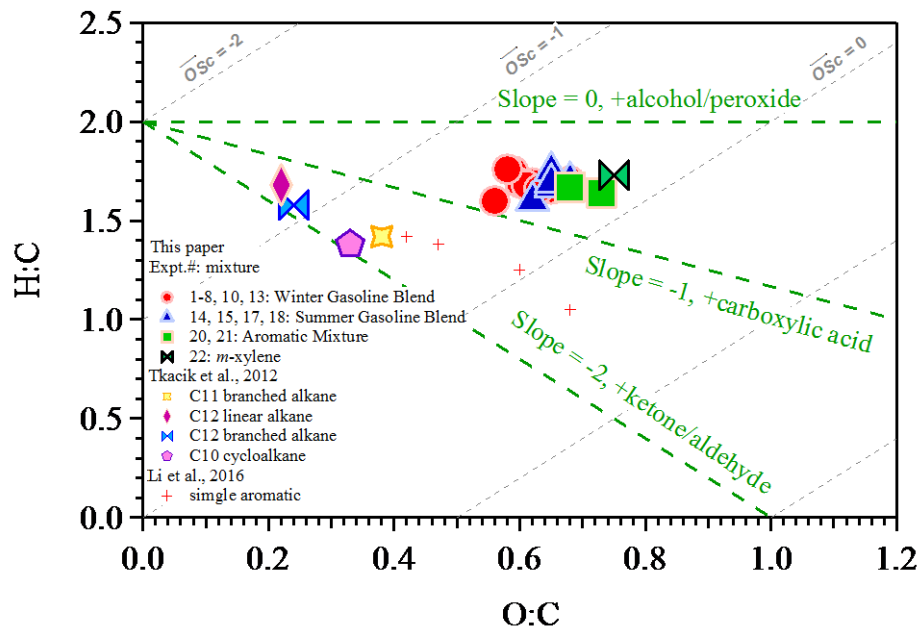


Figure 6. 10: Van Krevelen diagram of gasoline SOAs. Dotted green lines show slopes of 0, -1 and -2. Dotted grey lines show \overline{OS}_C of 0, -1 and -2.

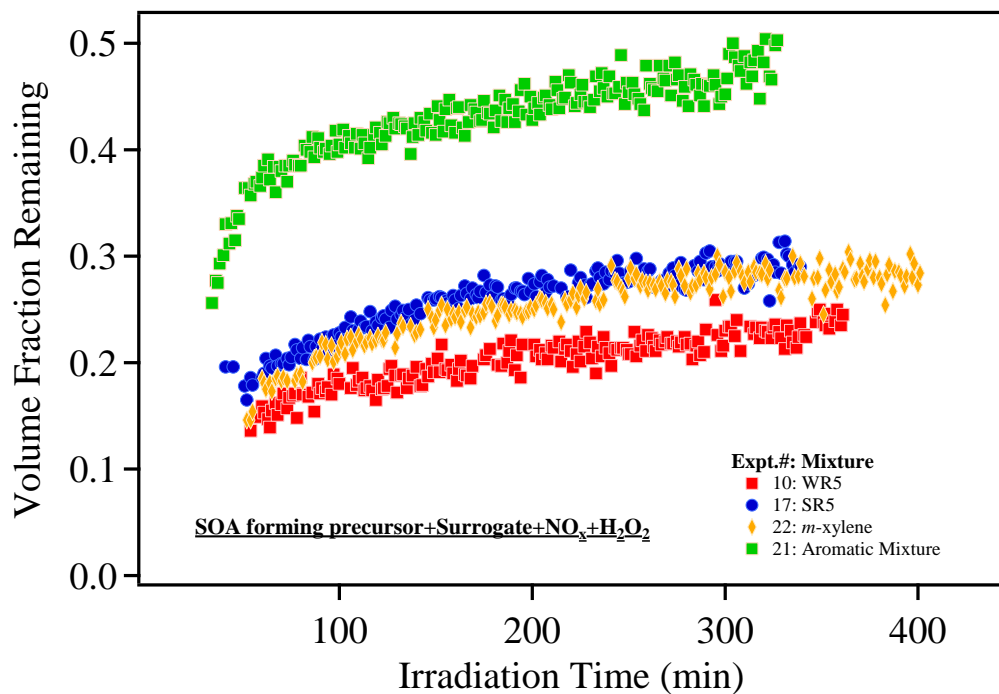


Figure 6. 11: VFR of winter and summer blend gasoline SOA. VFRs of *m*-xylene and aromatic mixture SOAs under the same experimental condition are shown as comparison.

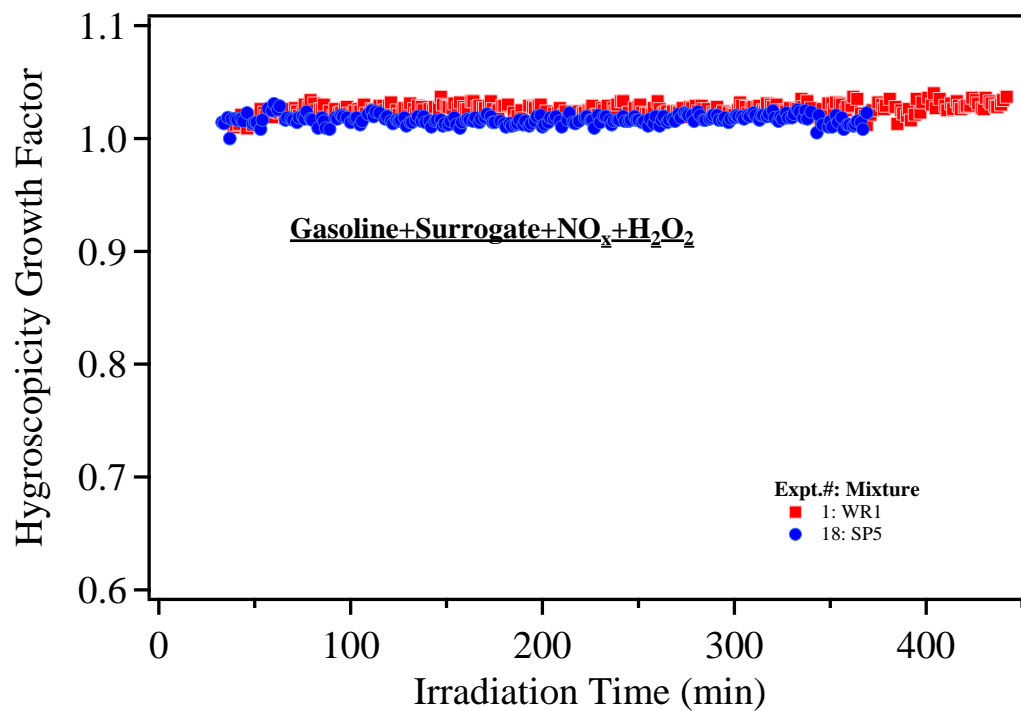


Figure 6. 12: Hygroscopicity growth factor of winter and summer blend gasoline SOAs.

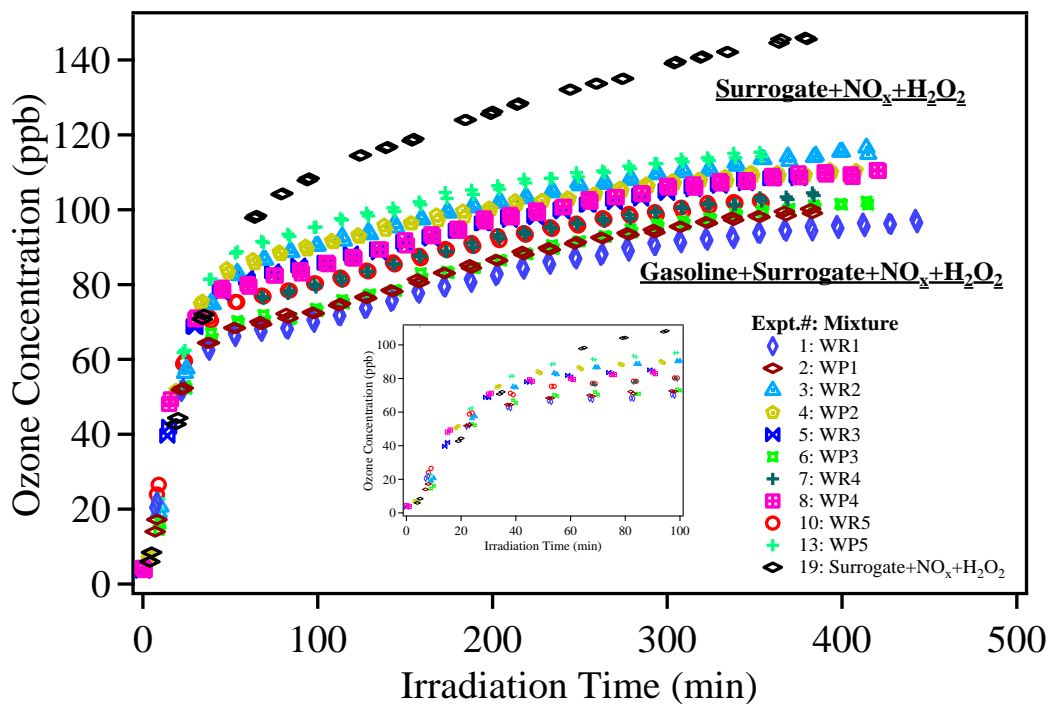


Figure 6. 13: Ozone formation from winter gasoline blends with surrogate, NO_x, and H₂O₂.

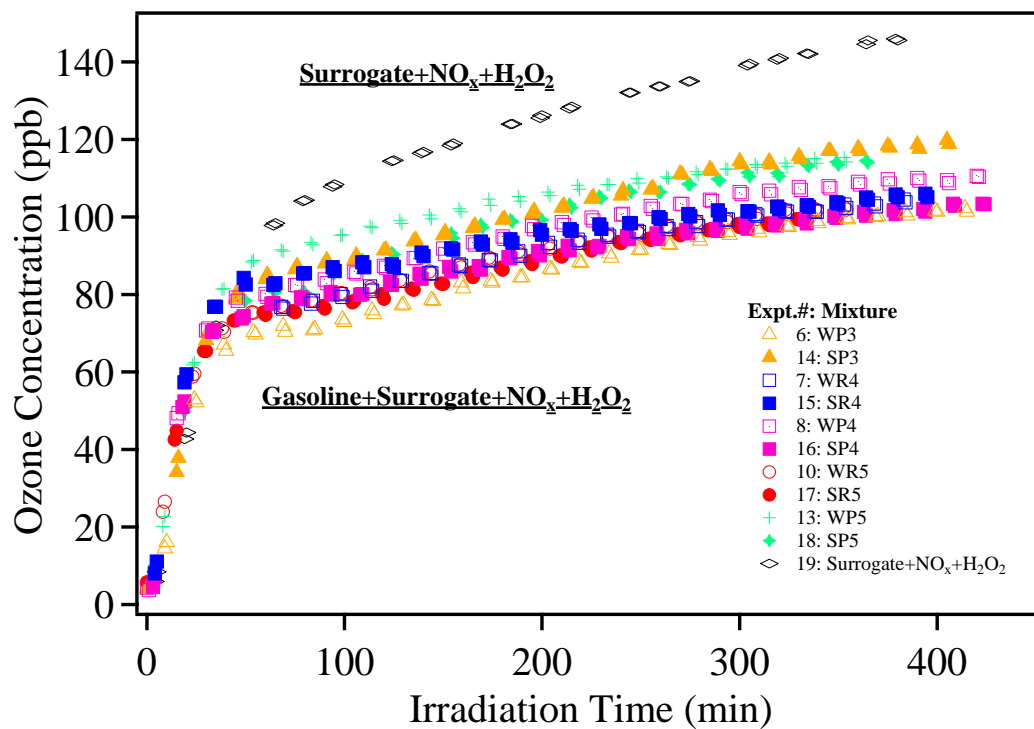


Figure 6. 14: Comparison of ozone formation from winter and summer gasoline blends with surrogate, NO_x, and H₂O₂

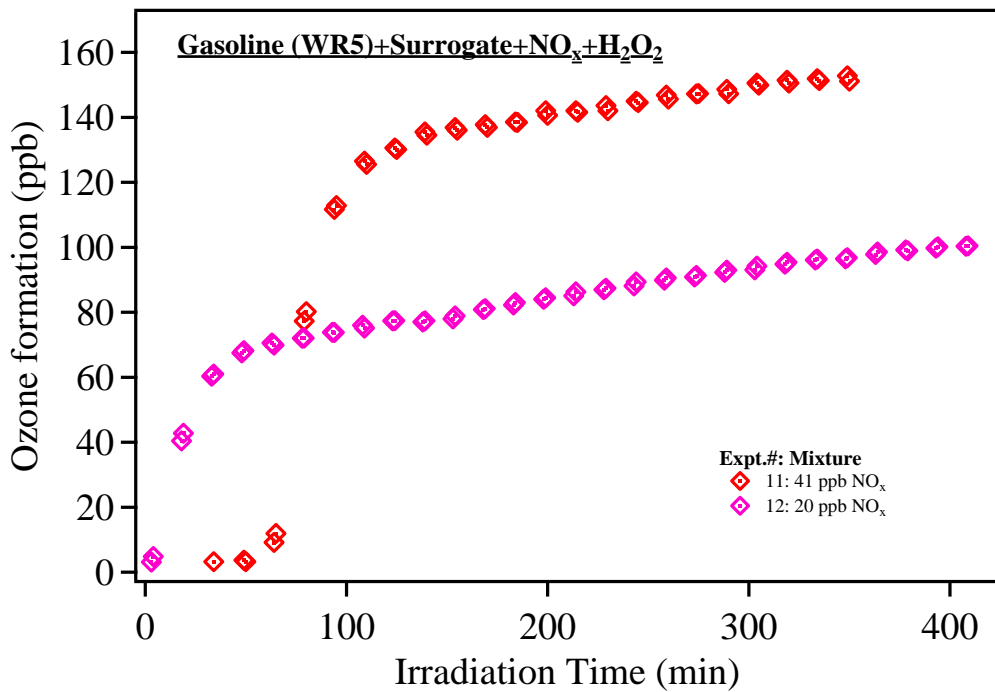


Figure 6. 15: Ozone formation from photo-oxidation of WR5 with surrogate and H₂O₂ at various NO_x concentrations.

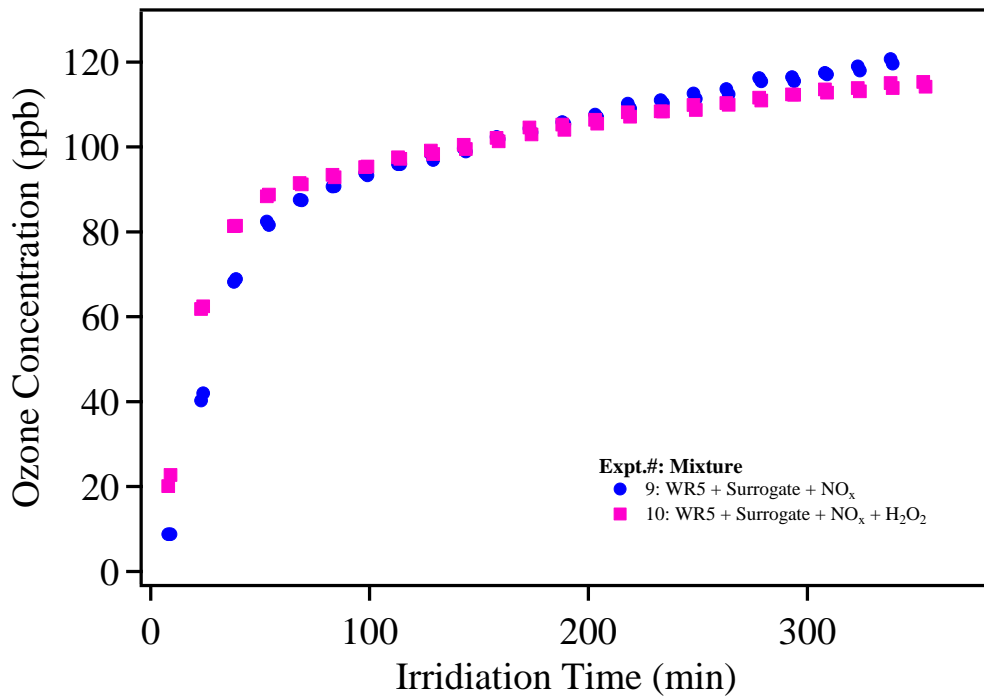


Figure 6. 16: Comparison of ozone formation from Wp5 with or without H₂O₂. The other experimental conditions are the same.

Chapter 7: Conclusions & Future Work

A primary objective of this study was to provide critical experimental data on the atmospheric availability of select IVOCs (components of consumer products) and IVOC mixtures. The select IVOCs studied within this work include: Benzyl Alcohol, diethylene glycol, Dipropylene Glycol Methyl Ether Acetate (DPGMEA), Diethylene Glycol Monobutyl Ether (DEGBE), n-Tridecane, n-Heptadecane, Diethylene Glycol Ethyl Ether (DEGEE), Dimethyl Glutarate (DBE-5), 2,2,4-trimethyl-1,3-pentanediol monoisobutyrate (Texanol), glyceryl triacetate Propylene Glycol, Triethanolamine, Glycerol, and Methyl Palmitate. These IVOCs are also called LVP-VOCs and are considered by CARB as meeting the LVP-VOC nonvolatile standards. However, Benzyl alcohol, DEGBE, n-Tridecane, DBE-5, DPGMEA, DEGEE, and propylene glycol lost more than 95% of their mass within 1 month and Texanol® within 3 months. Glyceryl triacetate, diethylene glycol, and n-Heptadecane lost half of their weights within 6 months. Triethanolamine, Glyceryl Triacetate, and Methyl Palmitate did not show appreciable evaporation rates after six months and no further environmental chamber experiments were carried out done on with them. These observations suggest that these IVOCs could evaporate after extended periods of time and become SOA and ozone-forming precursors. A semi-empirical formula using vapor pressure and molecular weight of the IVOC was identified from the scientific literature and found to be sufficient to accurately estimate evaporation rates for the wide range of IVOCs studied within this dissertation.

This study proceeded to evaluate the evaporation rate, and therefore atmospheric availability, of IVOC-containing mixtures. The select IVOC-containing mixtures included eight unburnt #2 diesel fuel samples. ~20% of the diesel fuel evaporated over a period of 10-months at room temperature. Nevertheless, more is expected to evaporate at slightly elevated temperature. The semi-empirical formula that correlates chemical vapor pressure and molecular weight with evaporation rate was also sufficient to accurately estimate evaporation rates for unburnt #2 diesel fuels.

Another primary objective of the dissertation was to evaluate the ozone and SOA formation from the select individual IVOCs, IVOC-containing mixtures (generic consumer products (Caulk Remover, Laundry Detergent, Paint Stripper, General Purpose Spray Cleaner Mixture and Hand Lotion), industrial hydrocarbon solvent mixtures (Conosol[®] C-200 and Isopar[®] M), and unburnt commercial #2 diesel), and unburnt commercial gasoline. Therefore, environmental chamber experiments were conducted within the advanced environmental chamber facility housed at the CE-CERT at UCR designed to investigate atmospheric reactivity, ozone formation, and PM formation at relevant atmospheric concentrations. SOA formation ranged widely among IVOCs explored. The hypothesis that IVOCs begin with lower vapor pressure than VOCs and therefore will form more SOA was proven to be generally not true for the compounds studied. Nearly half of the select IVOCs did not form SOA. However, several selected IVOCs formed appreciable SOA. Ozone formations from several individual IVOCs are suppressed, which indicates that the IVOCs act as either radical inhibitors or removed

NO_x at a faster rate than the surrogate mixture. Atmospheric Chemical Mechanism SAPRC-2011 was evaluated for the IVOCs studied. Generally, excellent agreement is observed between the IVOC experiments within this work and that predicted by the model providing confidence in the gas-phase reactivity data previously obtained and currently used for these compounds.

The addition of lab created generic consumer products has a weak influence on ozone formation from the surrogate mixture but strongly affects SOA formation. Other components, beyond the individually identified IVOCs also strongly contribute to aerosol formation as the total aerosol formation observed could not be explained solely by the individual aerosol forming IVOCs studied. The overall SOA and ozone formation of the generic consumer product could not be explained solely by analyzing the results of the pure IVOC experiments.

Heavy *n*-alkanes and alkane mixtures are great IVOC systems, which are explored in detail in this dissertation. Conosol[®] C-200, Isopar[®] M, *n*-C₁₇, and *n*-C₁₃ form significant amounts of SOA under urban relevant NO_x levels in the presence of a surrogate ROG mixture and H₂O₂. Compared with H₂O₂ only and surrogate only experiments, SOA formation is the highest for the experiment where the surrogate ROG mixture provides a baseline reactivity in the system with enhanced hydroxyl radical (H₂O₂ added). SOA formation is enhanced for larger *n*-alkanes in the presence of H₂O₂, which is caused by decreased volatility (Volatility: C₁₃>C₁₄>C₁₅>C₁₆). Ozone formation is suppressed in

general because of the formation of organic nitrates from heavy alkanes. It is still unclear how highly oxygenated SOA is formed from the photo-oxidation of *n*-C₁₇ in the presence of the surrogate ROG mixture and H₂O₂ at urban relevant NO_x levels. The conclusions drawn for *n*-alkanes and hydrocarbon solvents could be extrapolated to similar individual IVOCs or IVOC mixtures.

2 diesel fuels also contain a lot of IVOCs. Photo-oxidation of the unburned diesel fuel generated significant SOA rapidly. Approximately twice the SOA was formed from diesel fuel compared with that from *n*-pentadecane leading us to the conclusion that there is a large potential of both aromatics and other alkanes larger than *n*-Pentadecane to contribute to SOA formation. Increasing NO_x concentration at urban NO_x levels enhanced SOA and ozone production due to enhancement of hydroxyl radical concentrations within the environmental chamber. Nevertheless, SOA formation under previously reported extremely high NO_x concentrations led to nearly 14 times lower SOA formation while ozone formation was negligible compared with those under low NO_x condition. Therefore, operating the chamber under more relevant urban concentrations and reactivities greatly enhanced the measured aerosol formation potential of diesel fuel. Furthermore, two distinct SOAs were formed under low and high NO_x conditions in this study with a major fraction of the high NO_x system forming organic nitrates while little organic nitrate formation occurs when NO_x concentrations are in the tens of ppb. The trends observed during the current experiments demonstrate the importance of atmospheric NO_x concentrations; however, it is important to note that NO_x is

continuously injected into the atmosphere in urban areas so further study is needed to determine the full impact of lowering NO_x emissions on atmospheric SOA formation from diesel fuel. The SOA produced in this work at urban NO_x concentrations is observed to be similar to the ambient semi-volatile oxygenated organic aerosol (SV-OOA) from AMS high resolution data. The produced diesel SOA does not undergo appreciable oxidation once formed suggesting that the SOA formed from photo-oxidation of diesel is first generation.

The above sections of this dissertation provide experimental data for the understanding of SOA formation from photo-oxidation of IVOCs and IVOC mixtures in the Earth's atmosphere. Photo-oxidation of IVOCs is a potential source of oxygenated OA at urban relevant NO_x concentration. Further detailed studies are required to determine functional relationships of other IVOC compound types to improve forecasting of ability of other types of IVOCs to form SOA.

Lastly, SOA and ozone formation from unburned gasoline was investigated. Photo-oxidation of unburnt winter blend gasoline samples show consistent SOA formation regardless of fuel manufacturer and octane rating. The parameters enhancing SOA formation include aromatic content of the gasoline sample, hydroxyl radical concentration, and NO_x concentration (within 100 ppb). There is a linear trend between SOA formation and hydroxyl radical concentration. The greater the percentage of aromatic content and NO_x concentration are, the more SOA forms. The overall SOA

formation is OH driven in this work. NO_x is another parameter to tune hydroxyl radical concentration. Gasoline forms less SOA and ozone than its aromatic mixture counterpart, which indicates that other compounds (e.g. isoalkanes etc.) in the gasoline mixture suppress SOA and ozone formation. General trends in SOA and ozone formation between winter and summer gasoline blends are not found. The gasoline SOA generated at urban relevant NO_x levels is similar to the ambient SV-OOA from AMS high resolution data.

Reference

Alnajjar, M., Cannella, B., Dettman, H., Fairbridge, C., Franz, J., Gallant, T., Gieleciak, R., Hager, D., Lay, C., Lewis, S., Ratcliff, M., Sluder, S., Storey, J., Yin, H., Zigler, B., 2010. Chemical and physical properties of the fuels for advanced combustion engines (FACE) research diesel fuels. CRC Report No. FACE-1.

Bahreini, R., Middlebrook, A. M., de Gouw, J. A., Warneke, C., Trainer, M., Brock, C. A., Stark, H., Brown, S. S., Dube, W. P., Gilman, J. B., Hall, K., Holloway, J. S., Kuster, W. C., Perring, A. E., Prevot, A. S. H., Schwarz, J. P., Spackman, J. R., Szidat, S., Wagner, N. L., Weber, R. J., Zotter, P., Parrish, D. D., 2012. Gasoline emissions dominate over diesel in formation of secondary organic aerosol mass. *Geophys. Res. Lett.* 39, L060805.

Bernard, F., Magneron, I., Eyglunent, G., Daële, V., Wallington, T. J., Hurley, M. D., Mellouki, A., 2013. Atmospheric chemistry of benzyl alcohol: kinetics and mechanism of reaction with OH radicals. *Environ. Sci. Technol.* 47, 3182-3189.

Brandenberger, S., Mohr, M., Grob, K., Neukom, H. P., 2005. Contribution of unburned lubricating oil and diesel fuel to particulate emission from passenger cars. *Atmos. Environ.* 39, 6985-6994.

Cappa, C. D., Jathar, S. H., Kleeman, M. J., Docherty, K. S., Jimenez, J. L., Seinfeld, J. H., Wexler, A. S., 2016. Simulating secondary organic aerosol in a regional air quality model using the statistical oxidation model-Part 2: Assessing the influence of vapor wall losses. *Atmos. Chem. Phys.* 16, 3041-3059.

California Air Resources Board (CARB), 2012. Emission Inventory Data. Retrieved from <https://www.arb.ca.gov/ei/emissiondata.htm> (website).

California Air Resources Board (CARB), 2015. Regulation for reducing emissions from consumer products. Title 17, California Code of Regulations, Division 3, Chapter 1, Subchapter 8.5, Article 2, 94507-94517. Available online at: <https://www.arb.ca.gov/consprod/regs/regs.htm>

Caravaggio, G. A., Charland, J. P., MacDonald, P., Graham, L., 2007. n-Alkane profiles of engine lubricating oil and particulate matter by molecular sieve extraction. *Environ. Sci. Technol.* 41, 3697-3701.

Carter, W. P. L., Luo, D., Irina L. Malkina, I. L., Pierce, J. A., 1995. Environmental Chamber Studies of atmospheric compounds. Effects of varying ROG surrogate and NO_x. Final Report to California Air Resources Board, Contract A032-096, Coordinating Research Council, Inc., Project ME-9, National Renewable Energy Laboratory, Contract ZF-2-12252, South Coast Air Quality Management District, Contract C91323.

Carter, W. P. L., Cocker, D. R., III, Fitz, D. R., Malkina, I. L., Bumiller, K., Sauer, C. G., Pisano, J. T., Bufalino, C., Song, C., 2005. A new environmental chamber for evaluation of gas- phase chemical mechanisms and secondary aerosol formation. *Atmos. Environ.* 39, 7768-7788.

Carter, W. P. L., 2009. Updated maximum incremental reactivity scale and hydrocarbon bin reactivities for regulatory applications. Report to the CARB. Contract 07-339.

Carter, W. P. L., 2010. Development of the SAPRC-07 Chemical Mechanism. *Atmos. Environ.* 44, 5324-5335.

Carter, W. P. L., 2011. Environmental Chamber Study of Ozone Impacts of Coatings VOCs. Final report to California Air Resources Board, Contract No. 07-339, May 11. Available at <http://www.cert.ucr.edu/~carter/absts.htm#coatrpt2>

Carter, W. P. L., Heo, G., Cocker III, D. R., Nakao, S., 2012. SOA formation: chamber study and model development. Final Report to the California Air Resources Board Contract No. 08-326.

Chan, A. W. H., Kautzman, K. E., Chhabra, P. S., Surratt, J. D., Chan, M. N., Crouse, J. D., Kürten, A., Wennberg, P. O., Flagan, R. C., and Seinfeld, J.H., 2009. Secondary organic aerosol formation from photooxidation of naphthalene and alkylnaphthalenes: implications for oxidation of intermediate volatility organic compounds (IVOCs). *Atmospheric Chemistry and Physics*. 9, 3049-3060.

Chan, A. W. H., Isaacman, G., Wilson, K. R., Worton, D. R., Ruehl, C. R., Nah, T., Gentner, D. R., Dallmann, T. R., Kirchstetter, T.W., Harley, R. A., Gilman, J. B., Kuster, W. C., deGouw, J. A., Offenberg, J. H., Kleindienst, T. E., Lin, Y. H., Rubitschun, C. L., Surratt, J. D., Hayes, P. L., Jimenez, J. L., Goldstein, A. H., 2013. Detailed chemical characterization of unresolved complex mixtures in atmospheric organics: Insights into emission sources, atmospheric processing, and secondary organic aerosol formation. *J. Geophys. Res.* 118, 6783-6796.

Chen, C., Kacarab, M., Tang, P., David R. Cocker III, D. R., 2016. SOA formation from naphthalene, 1-methylnaphthalene, and 2-methylnaphthalene photooxidation. *Atmos. Environ.* 131, 424-433.

Chevron Corporation, 2007. Diesel Fuels Technical Review.

Chhabra, P. S., Ng, N. L., Canagaratna, M. R., Corrigan, A. L., Russell, L. M., Worsnop, D. R., Flagan, R.C., Seinfeld, J. H., 2011. Elemental composition and oxidation of chamber organic aerosol. *Atmos. Chem. Phys.* 11, 8827-8845.

Cocker, D. R., Clegg, S. L., Flagan, R. C., and Seinfeld, J. H., 2001a. The effect of water on gas-particle partitioning of secondary organic aerosol. Part I: α -pinene/ozone system. *Atmospheric Environment*. 35, 6049-6072.

Cocker, D. R., Mader, B. T., Kalberer, M., Flagan, R. C., and Seinfeld, J. H., 2001b. The effect of water on gas-particle partitioning of secondary organic aerosol: II. m-xylene and 1, 3, 5-trimethylbenzene photooxidation systems. *Atmospheric Environment*. 35, 6073-6085.

Cocker, D.R., Flagan, R.C., Seinfeld, J.H., 2001c. State-of-the-art chamber facility for studying atmospheric aerosol chemistry. *Environ. Sci. Technol.* 35, 2594-2601.

Cocker, D. R., Li, L., Price, D., Kacarab, M., Chen, C., 2014. Review of VOC Emissions Inventory for Consumer Products and Architectural Coatings for Potential Alternative Fate and Availability Corrections. Consumer Specialty Products Association.

DeCarlo, P. F., Kimmel, J. R., Trimborn, A., Northway, M. J., Jayne, J. T., Aiken, A. C., Gonin, M., Fuhrer, K., Horvath, T., Docherty, K. S., Worsnop, D. R., Jimenez, J. L., 2006. Field-deployable, high-resolution, time-of-flight aerosol mass spectrometer. *Analytical chemistry*. 78, 8281-8289.

Derwent, R. G., Jenkin, M. E., Utembe, S. R., Shallcross, D. E., Murrells, T. P., Passant, N. R., 2010. Secondary organic aerosol formation from a large number of reactive man-made organic compounds. *Sci. Total Environ.* 408, 3374-3381.

Donahue, N. M., Kroll, J. H., Pandis, S. N., Robinson, A. L., 2012. A two-dimensional volatility basis set – Part 2: diagnostics of organic-aerosol evolution. *Atmos. Chem. Phys.* 12, 615-634.

Emanuelsson, E. U., Hallquist, M., Kristensen, K., Glasius, M., Bohn, B., Fuchs, H., Kammer, B., Kiendler-Scharr, A., Nehr, S., Rubach, F., Tillmann, R., Wahner, A., Wu, H.-C., 2013. Th. F. Mentel Formation of anthropogenic secondary organic aerosol (SOA) and its influence on biogenic SOA properties. *Atmos. Chem. Phys.* 13, 2837-2855.

EPA., 2008. In 2005 National Emissions Inventory Data & Documentation; EPA: Washington, DC. Retrieved from: <https://www.epa.gov/air-emissions-inventories/2008-national-emissions-inventory-nei-data>.

Fahnestock, K. A. S., Yee, L. D., Loza, C. L., Coggon, M. M., Schwantes, R., Zhang, X., Dalleska, N. F., and Seinfeld, J. H., 2015. Secondary Organic Aerosol Composition from C12 Alkanes. *J. Phys. Chem. A*. 119, 4281-4297.

Finlayson-Pitts, B. J., Pitts Jr., J. N., 1993. Atmospheric Chemistry of Tropospheric Ozone Formation: Scientific and Regulatory Implications. *AIR & WASTE*. 43, 1091-1100.

Flagan, R.C., Seinfeld, J.H., 1988. Fundamentals of air pollution engineering. Prentice-Hall, Inc., Englewood Cliffs, New Jersey.

Flores, J. M., Bar-Or, R. Z., Bluvshstein, N., Abo-Riziq, A., Kostinski, A., Borrmann, S., Koren, I., Koren, I., Rudich, Y., 2012. Absorbing aerosols at high relative humidity: linking hygroscopic growth to optical properties. *Atmos. Chem. Phys.* 12, 5511-5521.

Fiore, A. M., Naik, V., Leibensperger, E. M., 2015. Air Quality and Climate Connections. *Journal of the Air & Waste Management Association.* 65, 645-685.

Fuzzi, S., Baltensperger, U., Carslaw, K., Decesari, S., Denier van der Gon, H., Facchini, M. C., Fowler, D., Koren, I., Langford, B., Lohmann, U., Nemitz, E., Pandis, S., Riipinen, I., Rudich, Y., Schaap, M., Slowik, J. G., Spracklen, D. V., Vignati, E., Wild, M., Williams, M. Gilardoni, S., 2015. Particulate matter, air quality and climate: lessons learned and future needs. *Atmos. Chem. Phys.* 15, 8217-8299.

Gentner, D. R., R A., Miller A. M., Goldstein, A. H., 2009. Diurnal and seasonal variability of gasoline-related volatile organic compound emissions in Riverside, California. *Environ Sci Technol.* 43, 4247-4252.

Gentner, D. R., Isaacman, G., Worton, D. R., Chan, A. W. H., Dallmann, T. R., Davis, L., Liu, S., Day, D. A., Russell, L. M., Wilson, K. R., Weber, R., Guha, A., Harley, R. A., Goldstein, A. H., 2012. Elucidating secondary organic aerosol from diesel and gasoline vehicles through detailed characterization of organic carbon emissions. *Proc Natl Acad Sci.* 109, 18318-18323.

Gentner, D. R., Jathar, S. H., Gordon, T. D., Bahreini, R., Day, D. A., Haddad, I. E., Hayes, P. L., Pieber, S. M., Platt, S. M., de Gouw, J., Goldstein, A. H., Harley, R.A., Jimenez, J. L., André S. H. Prévôt, A. S. H., Robinson, A. L., 2017. Review of Urban Secondary Organic Aerosol Formation from Gasoline and Diesel Motor Vehicle Emissions. *Environ. Sci. Technol.* 51, 1074-1093.

Griffin, R. J., Cocker, D. R., Flagan, R. C., Seinfeld, J. H., 1999. Organic aerosol formation from the oxidation of biogenic hydrocarbons. *Journal of geophysical research.* 104, 3555-3567.

Guth, J. A., Reischmann, F. J., Allen, R., Arnold, D., Hassink, J., Leake, C. R., Skidmore, M. W., Reeves, G. L., 2004. Volatilisation of crop protection chemicals from crop and soil surfaces under controlled conditions-prediction of volatile losses from physicochemical properties. *Chemosphere.* 57, 871-887.

Hallquist, M., Wenger, J. C., Baltensperger, U., Rudich, Y., Simpson, D., Claeys, M., Dommen, J., Donahue, N. M., George, C., Goldstein, A. H., Hamilton, J. F., Herrmann, H., Hoffmann, T., Iinuma, Y., Jang, M., Jenkin, M. E., Jimenez, J. L., Kiendler-Scharr,

A., Maenhaut, W., McFiggans, G., Mentel, T. F., Monod, A., Prevot, A. S. H., Seinfeld, J. H., Surratt, J. D., Szmigielski, R., and Wildt, J., 2009. The formation, properties and impact of secondary organic aerosol: current and emerging issues, *Atmos. Chem. Phys.* 9, 5155-5236.

Hajipour, S., Satyro, M. a. and Foley, M. W., 2014. Uncertainty analysis applied to thermodynamic models and fuel properties - Natural gas dew points and gasoline Reid vapor pressures. *Energy and Fuels.* 28, 1569-1578.

Harley, R. A., Hannigan, M. P., Cass, G. R., 1992. Respeciation of Organic Gas Emissions and the Detection of Excess Unburned Gasoline in the Atmosphere. *Atmos. Environ.* 26, 2395.

Heald, C. L., Kroll, J. H., Jimenez, J. L., Docherty, K. S., DeCarlo, P. F., Aiken, A. C., Chen, Q., Martin, S. T., Farmer, D. K., Artaxo, P., 2010. A simplified description of the evolution of organic aerosol composition in the atmosphere. *GEOPHYSICAL RESEARCH LETTERS.* 37, L08803.

Hoffmann, T., Odum, J. R., Bowman, F., Collins, D., Klockow, D., Flagan, R. C., Seinfeld, J. H., 1997. Formation of organic aerosols from the oxidation of biogenic hydrocarbons. *J., Atmos. Chem.* 26, 189-222.

Hildebrandt, L., Donahue, N., Pandis, S., 2009. High formation of secondary organic aerosol from the photo-oxidation of toluene. *Atmos. Chem. Phys.* 9, 2973.

Houssni Lamkaddam, Aline Gratien, Edouard Pangui, Mathieu Cazaunau, Bénédicte Picquet-Varrault, and Jean-François Doussin., 2017. High-NO_x Photooxidation of n - Dodecane: Temperature Dependence of SOA Formation, *Environ. Sci. Technol.* 51, 192-201.

Jathar, S. H., Miracolo, M. A., Tkacik, D. S., Donahue, N. M., Adams, P. J., Robinson, A. L., 2013. Secondary Organic Aerosol Formation from Photo-Oxidation of Unburned Fuel: Experimental Results and Implications for Aerosol Formation from Combustion Emissions. *Environ. Sci. Technol.* 47, 12886-12893.

Jathar, S. H., Cappa, C. D., Wexler, A. S., Seinfeld, J. H., Kleeman, M. J., 2016. Simulating secondary organic aerosol in a regional air quality model using the statistical oxidation model—Part 1: Assessing the influence of constrained multi-generational ageing. *Atmos. Chem. Phys.* 16, 2309-2322.

Jathar, S. H., Woody, M., Pye, H. O. T., Kirk R. Baker, Robinson, A. L., 2017. Chemical transport model simulations of organic aerosol in southern California: model evaluation and gasoline and diesel source contributions. *Atmos. Chem. Phys.* 17, 4305-4318.

Jimenez, J. L. et al., 2009. Evolution of organic aerosols in the atmosphere. *Science* 326, 1525–1529 .

Kacarab, M.E., 2016. Impacts of Controlling Reactivity and Temperature on Advanced Study of Secondary Organic Aerosol Formation. Retrieved from UC Riverside Electronic Theses and Dissertations. (<http://escholarship.org/uc/item/4sq547tq>).

Kanakidou, M., Seinfeld, J. H., Pandis, S. N., Barnes, I., Dentener, F. J., Facchini, M. C., Van Dingenen, R., Ervens, B., Nenes, A., and Nielsen, C.J., 2005. Organic aerosol and global climate modelling: a review. *Atmospheric Chemistry and Physics* 5, 1053-1123.

Kiendler-Scharr, A., Nehr, S., Rubach, F., Tillmann, R., Wahner, A., Wu, H.-C., Mentel, Th. F., 2013. Formation of anthropogenic secondary organic aerosol (SOA) and its influence on biogenic SOA properties. *Atmos. Chem. Phys.*, 13, 2837–2855.

Koo, B. Y., Ansari, A. S., Pandis, S. N., 2003. Integrated approaches to modeling the organic and inorganic atmospheric aerosol components, *Atmos. Environ.* 37(34), 4757–4768.

Krechmer, E. J., Demetrios, P., Paul J. Ziemann, P. J., Jimenez, J. L., 2016. Quantification of Gas-Wall Partitioning in Teflon Environmental Chambers Using Rapid Bursts of Low-Volatility Oxidized Species Generated in Situ. *Environ. Sci. Technol.* 50, 5757-5765.

Kroll J. H., Seinfeld J.H., 2008. Chemistry of secondary organic aerosol: formation and evolution of low-volatility organics in the atmosphere. *Atmos. Environ.* 42, 3593-3624.

Kroll, J. H., Donahue, N. M., Jimenez, J. L., Kessler, S. H., Canagaratna, M. R., Wilson, K. R., Altieri, K. E., Mazzoleni, L. R., Wozniak, A. S., Bluhm, H., Mysak, E. R., Smith, J. D., Kolb, C. E., and Worsnop, D. R., 2011. Carbon oxidation state as a metric for describing the chemistry of atmospheric organic aerosol. *Nat. Chem.* 3, 133-139.

Kundu, S., Fisseha, R., Putman, A. L., Rahn, T. A., Mazzoleni, L. R., 2012. High molecular weight SOA formation during limonene ozonolysis: insights from ultrahigh-resolution FT-ICR mass spectrometry characterization. *Atmos. Chem. Phys.* 12, 5523-5536.

Lambe, A. T., Onasch, T. B., Croasdale, D. R., Wright, J. P., Martin, A. T., Franklin, J. P., Massoli, P., Kroll, J. H., Canagaratna, M. R., Brune, W. H., Worsnop, D. R., and Davidovits, P., 2012. Transitions from functionalization to fragmentation reactions of laboratory secondary organic aerosol (SOA) generated from the OH oxidation of alkanes precursors, *Environ. Sci. Technol.* 46, 5430-5437.

Lelieveld, J., Dentener, F.J., 2000. What controls tropospheric ozone? *Journal of Geophysical Research: Atmospheres.* 105, 3531-3551.

Li, L., Tang, P., Cocker, D. R., 2015. Instantaneous nitric oxide effect on secondary organic aerosol formation from m-xylene photooxidation. *Atmospheric Environment*. 119, 144-155.

Li, L., Tang, P., Nakao, S., Kacarab, M. E., Cocker, D. R., 2016. Novel Approach for Evaluating Secondary Organic Aerosol from Aromatic Hydrocarbons: Unified Method for Predicting Aerosol Composition and Formation. *Environ. Sci. Technol.* 50, 6249-6256.

Li, L., Cocker, D. R., 2018. Molecular Structure Impacts on Secondary Organic Aerosol Formation from Glycol Ethers. *Atmos. Environ.*

Li, W., Li, L., Chen, C., Kacarab, M. E., Peng, W., Price, D., Xu, J., Cocker, D. R., 2018. Potential of select intermediate-volatility organic compounds and consumer products for secondary organic aerosol and ozone formation under relevant urban conditions. *Atmos. Environ.*

Li, Y., Lau, A. K. H., Fung, G. C. H., Zheng, J., Liu, S., 2013. Importance of NO_x control for peak ozone reduction in the Pearl River Delta region, J., *Geophysical Research: Atmospheres*, 118, 9428-9443.

Liang, F., Lu, M., Keener, T. C., Liu, Z., Khang, S. J., 2005. The organic composition of diesel particulate matter, diesel fuel and engine oil of a non-road diesel generator. *J. Environ. Monit.* 7, 983-988.

Lim, Y. B., Ziemann, P. J. Products and mechanism of secondary organic aerosol formation from reactions of n-alkanes with OH radicals in the presence of NO_x. *Environ. Sci. Technol.* 2005, 39, 9229-9236.

Lim, Y. B., Ziemann, P. J., 2009a. Chemistry of secondary organic aerosol formation from OH radical-initiated reactions of linear, branched, and cyclic alkanes in the presence of NO_x. *Aero. Sci. Technol.* 43, 604-619.

Lim, Y. B., Ziemann, P. J., 2009b. Effects of molecular structure on aerosol yields from OH radical-induced reactions of linear, branched, and cyclic alkanes in the presence of NO. *Environ. Sci. Technol.*, 43, 2328-2334.

Loza, C. L., Craven, J. S., Yee, L. D., Coggon, M. M., Schwantes, R. H., Shiraiwa, M., Zhang, X., Schilling, K. A., Ng, N. L., Canagaratna, M. R., Ziemann, P. J., Flagan, R. C., and Seinfeld, J. H., 2014. Secondary organic aerosol yields of 12-carbon alkanes, *Atmos. Chem. Phys. Discuss.*, 13, 20677-20727.

Ma, P. K., Zhao, Y., Robinson, A.L., Worton, D. R., Goldstein, A. H., Ortega, A. M., Jimenez, J. L., Zotter, P., Prévôt, A. S. H., Szidat, S., Hayes, P. L., 2017. Evaluating the

impact of new observational constraints on P-S/IVOC emissions, multi-generation oxidation, and chamber wall losses on SOA modeling for Los Angeles, CA. *Atmos. Chem. Phys.* 17, 9237-9259.

McDonald et al., 2018. Volatile Chemical Products Emerging as Largest Petrochemical Source of 1 Urban Organic Emissions. *Science*. 359(6377), 760-764.

Mackay, D., Wesenbeeck, I.V., 2014. Correlation of Chemical Evaporation Rate with Vapor Pressure. *Environ. Sci. Technol.* 48, 10259-10263.

Malloy, Q., Nakao, S., Switzer, D., Cocker, D., Hagino, H., 2009. On-line Density Measurements of Secondary Organic Aerosol Formation. *Aerosol Science and Technology*. 43, 673-678.

Matsunaga, A., Docherty, K. S., Lim, Y. B., Ziemann, P. J., 2009. Composition and yields of secondary organic aerosol formed from OH radical-initiated reactions of linear alkenes in the presence of NO_x: Modeling and measurements. 43, 1349-1357.

Matsunaga, A., Ziemann, P. J., 2010. Gas-wall partitioning of organic compounds in a Teflon film chamber and potential effects on reaction product and aerosol yield measurements. *Aero. Sci. Technol.* 44, 881-892.

Maria, S. F., Russell, L. M., Gilles, M. K., Myneni, S. C. B., 2004. Organic Aerosol Growth Mechanisms and Their Climate-Forcing Implications. *Science*. 306, 1921-1924.

Meier, J., Wehner, B., Massling, A., Birmili, W., Nowak, A., Gnauk, T., Brüggemann, E., Herrmann, H., Min, H., Wiedensohler, A., 2009. Hygroscopic growth of urban aerosol particles in Beijing (China) during wintertime: a comparison of three experimental methods. *Atmos. Chem. Phys.*, 9, 6865-6880.

Miracolo, M. A., Presto, A. A., Lambe, A. T., Hennigan, C. J., Donahue, N. M., Kroll, J. H., Worsnop, D. R., Robinson, A. L., 2010. Photo-Oxidation of Low-Volatility Organics Found in Motor Vehicle Emissions: Production and Chemical Evolution of Organic Aerosol Mass. *Environ. Sci. Technol.* 44, 1638-1643.

Naeher, L. P., Brauer, M., Lipsett, M., Zelikoff, J. T., Simpson, C. D., Koenig, J. Q., Smith, K. R., 2007. Woodsmoke health effects: A review. *Inhal. Toxicol.* 19, 67-106.

Nakao, S., Shrivastava, M., Nguyen, A., Jung, H., Cocker III, D. R., 2011. Interpretation of Secondary Organic Aerosol Formation from Diesel Exhaust Photooxidation in an Environmental Chamber. *Aerosol Science and Technology*. 45, 964-972.

- Nakao, S., Liu, Y., Tang, P., Chen, C.-L., Zhang, J., Cocker, D. R., 2012. Chamber studies of SOA formation from aromatic hydrocarbons: observation of limited glyoxal uptake. *Atmos. Chem. Phys.* 12, 3927-3937.
- Ng, N. L., Kroll, J. H., Chan, A. W. H., Chhabra, P. S., Flagan, R. C., Seinfeld, J. H., 2007. Secondary organic aerosol formation from m-xylene, toluene, and Benzene. *Atmos. Chem. Phys.*, 7, 3909-3922.
- Ng, N. L., Canagaratna, M. R., Zhang, Q., Jimenez, J. L., Tian, J., Ulbrich, I. M., Kroll, J. H., Docherty, K. S., Chhabra, P. S., Bahreini, R., Murphy, S. M., Seinfeld, J. H., Hildebrandt, L., Donahue, N. M., DeCarlo, P. F., Lanz, V. A., Prévôt, A. S. H., Dinar, E., Rudich, Y., Worsnop, D. R., 2010. Organic aerosol components observed in Northern Hemispheric datasets from Aerosol Mass Spectrometry. *Atmos. Chem. Phys.* 10, 4625-4641.
- Ng, N. L., Canagaratna, M. R., Jimenez, J. L., Chhabra, P. S., Seinfeld, J. H., Worsnop, D. R., 2011. Changes in organic aerosol composition with aging inferred from aerosol mass spectra. *Atmos. Chem. Phys.*, 11, 6465-6474.
- Odum, J. R., Hoffmann, T., Bowman, F., Collins, D., Flagan, R. C., Seinfeld, J. H., 1996. Gas/Particle Partitioning and Secondary Organic Aerosol Yields. *Environ. Sci. Technol.* 30, 2580-2585.
- Odum, J. R., Jungkamp, T. P. W., Griffin, R. J., Flagan, R. C., Seinfeld, J. H., 1997a. The atmospheric aerosol-forming potential of whole gasoline vapor. *Science.* 276, 96-99.
- Odum, J. R., Jungkamp, T. P. W., Griffin, R. J., Forstner, H. J. L., Flagan, R. C., Seinfeld, J. H., 1997b. Aromatics, reformulated gasoline, and atmospheric organic aerosol formation. *Environ. Sci. Technol.* 31, 1890-1897.
- Pankow, J. F., 1994. An absorption model of gas/particle partitioning of organic compounds in the atmosphere. *Atmos. Environ.* 28, 185-188.
- Pandis, S. N., Paulson, S. E., Seinfeld, J. H., Flagan, R. C., 1991. Aerosol formation the photooxidation of isoprene and β -pinene, *Atmos. Environ.* 25, 997-1008.
- Pope, C. A., Richard T. Burnett, Thun, M. J., Calle, E. E., Krewski, D., Kazuhiko Ito, K., Thurston, G. D., 2002. Lung Cancer, Cardiopulmonary Mortality, and Long-term Exposure to Fine Particulate Air Pollution. *JAMA.* 287, 1132-1141.
- Pope, C.A., Dockery, D.W., 2006. Health Effects of Fine Particulate Air Pollution: Lines that Connect. *Journal of the Air & Waste Management Association.* 56, 709-742.

- Pöschl, U., Shiraiwa, M., 2015. Multiphase Chemistry at the Atmosphere-Biosphere Interface Influencing Climate and Public Health in the Anthropocene. 115, 4440-4475.
- Presto, A. A., Miracolo, M. A., Kroll, J. H., Worsnop, D. R., Robinson, A. L., Donahue, N. M., 2009. Intermediate-volatility organic compounds: a potential source of ambient oxidized organic aerosol. *Environ. Sci. Technol.* 43, 4744-4749.
- Presto, A. A., Miracolo, M. A., Donahue, N. M., and Robinson, A. L., 2010. Secondary organic aerosol formation from high-NO_x photooxidation of low volatility precursors: n-alkanes, *Environ. Sci. Technol.* 44, 2029-2034.
- Qin, T.F. D., Plattner, G.-K., Tignor, M., Allen, S.K., Boschung, J., Nauels, A., Xia, Y., Bex, V., Midgley, P.M., 2013. Climate change 2013: The physical science basis. Contribution of working group I to the fifth assessment report of the Intergovernmental Panel on Climate Change. Cambridge University Press, 1535.
- Rader, D. J., McMurry, P. H., 1986. Application of the tandem differential mobility analyzer to studies of droplet growth or evaporation. *Journal of Aerosol Science.* 17, 771-787.
- Rappoport, S. and Gaumann, T., 1973. Retention indexes of isomeric alkanes in gas-chromatography, *Helvetica Chimica Acta*, 56, 1145-1158.
- Robinson, A. L., Donahue, N. M., Shrivastava, M. K., Weitkamp, E. A., Sage, A. M., Grieshop, A. P., Lane, T. E., Pierce, J. R., Pandis, S. N., 2007. Rethinking organic aerosols: Semivolatile emissions and photochemical aging. *Science.* 315, 1259-1262.
- Sage, A. M., Weitkamp, E. A., Robinson, A. L., Donahue, N.M., 2008. Evolving mass spectra of the oxidized component of organic aerosol: results from aerosol mass spectrometer analyses of aged diesel emissions. *Atmos. Chem. Phys.* 8, 1139-1152.
- Schauer, J. J., Kleeman, M. J., Cass, G. R., Simoneit, B. R. T., 1999. Measurement of emissions from air pollution sources. 2. C1 through C30 organic compounds from medium duty diesel trucks. *Environ. Sci. Technol.* 33, 1578-1587.
- Shin, H-M, McKone, T.E., Bennett, D.H., 2016. Volatilization of low vapor pressure – volatile organic compounds (LVP-VOCs) during three cleaning products-associated activities: potential contributions to ozone formation. *Chemosphere.* 153, 130-137.
- Singh, A., Dey, S., 2012. Influence of aerosol composition on visibility in megacity Delhi. *Atmospheric Environment*, 62, 367-373.
- Song, C., Na, K., Cocker, D. R., 2005. Impact of the Hydrocarbon to NO_x Ratio on Secondary Organic Aerosol Formation. *Environ. Sci. Technol.* 39, 3143-3149.

Song, C., Na, K., Warren, B., Malloy, Q., Cocker, D., 2007. Secondary organic aerosol formation from m-xylene in the absence of NO_x. *Environmental science & technology*. 41, 7409-16.

Tkacik, D. S., Presto, A. A., Donahue, N. M., Robinson, A. M., 2012. Secondary organic aerosol formation from intermediate-volatility organic compounds: cyclic, linear, and branched alkanes, *Environ., Sci., Technol.* 46, 8773-8781.

Tritscher, T., Dommen, J., DeCarlo, P. F., Gysel, M., Barmet, P. B., Praplan, A. P., Weingartner, E., Prévôt, A. S. H., Riipinen, I., Donahue, N. M., Baltensperger, U., 2011. Volatility and hygroscopicity of aging secondary organic aerosol in a smog chamber. *Atmos. Chem. Phys.* 11, 11477-11496.

Vo, U.-U.T., Morris, M.P., 2014. Nonvolatile, semivolatile, or volatile: redefining volatile for volatile organic compounds. *J. Air Waste Manag. Assoc.* 64, 661-669.

Volkamer, R., Jimenez, J. L., Martini, F. S., Dzepina, K., Zhang, Q., Salcedo, D., Molina, L. T., Worsnop, D. R., Molina, M. J., 2006. Secondary organic aerosol formation from anthropogenic air pollution: Rapid and higher than expected. *Geophysical research letters*. 33, L17811, doi:10.1029/2006GL026899.

Weitkamp, E. A., Sage, A. M., Pierce, J. R., Donahue, N. M., Robinson, A. L., 2007. Organic aerosol formation from photochemical oxidation of diesel exhaust in a smog chamber. *Environ. Sci. Technol.* 41, 6969.

Woodrow, J. E., Seiber, J. N., Baker, L. W., 1997. Correlation techniques for estimating pesticide volatilization flux and downwind concentrations. *Environ. Sci. Technol.* 31, 523-529.

Woodrow, J. E., Seiber, J. N., Dary, C., 2001. Predicting pesticide emissions and downwind concentrations using correlations with estimated vapor pressures. *J. Agric. Food Chem.* 49, 3841-3846.

Ye, P., Ding, X., Hakala, J., Hofbauer, V., Robinson, E. S., Donahue, N. M., 2016. Vapor wall loss of semi-volatile organic compounds in a Teflon chamber. *Aero. Sci. Technol.* 50, 822-834.

Yee, L. D., Craven, J. S., Loza, C. L., Schilling, K. A., Ng, N. L., Canagaratna, M. R., Ziemann, P. J., Flagan, R. C., Seinfeld, J. H., 2012. Secondary organic aerosol formation from Low-NO_x photooxidation of dodecane: evolution of multi-generation gasphase chemistry and aerosol composition, *J. Phys. Chem. A*, 116, 6211-6230.

Yee, L. D., Kautzman, K. E., Loza, C. L., Schilling, K. A., Coggon, M. M., Chhabra, P. S., Chan, M. N., Chan, A. W. H., Hersey, S. P., Crounse, J. D., Wennberg, P. O., Flagan,

R. C., Seinfeld, J. H., 2013. Secondary organic aerosol formation from biomass burning intermediates: phenol and methoxyphenols. *Atmos. Chem. Phys. Discuss.* 13, 3485-3532.

Yeh, G. K., Ziemann, P. J., 2014. Alkyl Nitrate Formation from the Reactions of C₈–C₁₄ n-Alkanes with OH Radicals in the Presence of NO_x: Measured Yields with Essential Corrections for Gas–Wall Partitioning. *J. Phys. Chem. A*, 118:8147-8157.

Zhang, S. H., Shaw, M., Seinfeld, J. H., Flagan, R. C., 1992. Photochemical aerosol formation from α -pinene and β -pinene, *J Geophys Res.* 97, 20717-20729.

Zhang, H., Ruehl, C. R., Chan, A. W. H., Nah, T., Worton, D. R., Isaacman, G., Goldstein, A. H.,

Wilson, K. R., 2013. OH-Initiated Heterogeneous Oxidation of Cholestane: A Model System for Understanding the Photochemical Aging of Cyclic Alkane Aerosols. *J. Phys. Chem. A* 117, 12449-12458.

Zhang, X., Cappa, C. D., Jathar, S. H., McVay, R. C., Ensberg, J. J., Kleeman, M. J., Seinfeld, J. H., 2014. Influence of vapor wall loss in laboratory chambers on yields of secondary organic aerosol. *PNAS*. 111, 5802-5807.

Zhao, Y. L., Hennigan, C. J., May, A. A., Tkacik, D. S., de Gouw, J. A., Gilman, J. B., Kuster, W. C., Borbon, A., Robinson, A. L., 2014. Intermediate-volatility organic compounds: A large source of secondary organic aerosol. *Environ. Sci. Technol.* 48, 13743-13750.